

NASA TECHNICAL NOTE



NASA TN D-8099

C4

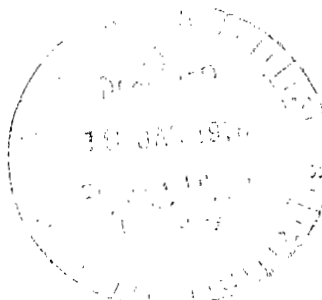
NASA TN D-8099



LOAN COPY: RETURN TO
AFWL TECHNICAL LIBRARY
KIRTLAND AFB, N. M.

INCIDENT SHOCK-WAVE CHARACTERISTICS
IN AIR, ARGON, CARBON DIOXIDE,
AND HELIUM IN A SHOCK TUBE
WITH UNHEATED HELIUM DRIVER

Charles G. Miller III and Jim J. Jones
Langley Research Center
Hampton, Va. 23665



NATIONAL AERONAUTICS AND SPACE ADMINISTRATION • WASHINGTON, D. C. • DECEMBER 1975



0133802

1. Report No. NASA TN D-8099		2. Government Accession No.		3. Recipient's Catalog No.	
4. Title and Subtitle INCIDENT SHOCK-WAVE CHARACTERISTICS IN AIR, ARGON, CARBON DIOXIDE, AND HELIUM IN A SHOCK TUBE WITH UNHEATED HELIUM DRIVER				5. Report Date December 1975	
				6. Performing Organization Code	
				8. Performing Organization Report No. L-10520	
				10. Work Unit No. 506-26-20-01	
7. Author(s) Charles G. Miller III and Jim J. Jones				11. Contract or Grant No.	
9. Performing Organization Name and Address NASA Langley Research Center Hampton, Va. 23665				13. Type of Report and Period Covered Technical Note	
12. Sponsoring Agency Name and Address National Aeronautics and Space Administration Washington, D.C. 20546				14. Sponsoring Agency Code	
15. Supplementary Notes					
16. Abstract Incident shock-wave velocities were measured in the Langley 6-inch expansion tube, operated as a shock tube, with air, argon, carbon dioxide, and helium as test gases. Unheated helium was used as the driver gas and most data were obtained at pressures of approximately 34 and 54 MN/m ² . A range of pressure ratio across the diaphragm was obtained by varying the quiescent test-gas pressure, for a given driver pressure, from 0.0276 to 34.5 kN/m ² . Single- and double-diaphragm modes of operation were employed and diaphragms of various materials tested. Shock velocity was determined from micro-wave interferometer measurements, response of pressure transducers positioned along the driven section (time-of-arrival gages), and to a lesser extent, measured tube-wall pressure. Velocities obtained from these methods are compared and limitations of the methods discussed. The present results are compared with theory and the effects of diaphragm mode (single or double diaphragm), diaphragm material, heating of the driver gas upon pressurization of the driver section, diaphragm opening time, interface mixing, and two-dimensional (nonplanar) flow are discussed.					
17. Key Words (Suggested by Author(s)) Shock tube Shock wave Velocity measurements				18. Distribution Statement Unclassified — Unlimited Subject Category 34	
19. Security Classif. (of this report) Unclassified	20. Security Classif. (of this page) Unclassified	21. No. of Pages 84	22. Price* \$4.75		

CONTENTS

	Page
SUMMARY	1
INTRODUCTION	2
SYMBOLS	3
FACILITY AND APPARATUS	5
INSTRUMENTATION	7
Incident Shock Velocity	7
Microwave Interferometer System	7
Time-of-Arrival (TOA) Measurement	7
Wall-Pressure Measurement	9
Driver-Section Pressure and Temperature	9
TESTS	9
DATA REDUCTION AND UNCERTAINTY	10
Microwave Interferometer Measurements	10
Time of Arrival	11
Wall Pressure	11
RESULTS AND DISCUSSION	12
Effect of Uncertainty in Incident Shock Velocity on Predicted Expansion-Tube Performance	12
Comparison of Methods for Measuring Incident Shock Velocity	13
Comparison of Measured Shock Velocity With Theory	17
Comparison With Conventional Theory	18
Causes of Discrepancy	19
Driver temperature	19
Single- or double-diaphragm mode of operation	21
Diaphragm material	22
Diaphragm opening time	23
Formation-from-compression predictions	23
Unsteady flow analyses	25
Interface mixing	27
Nonequilibrium flow	27
Departures from one-dimensional flow	27

	Page
CONCLUDING REMARKS	29
REFERENCES	31
TABLES	33
FIGURES	36

INCIDENT SHOCK-WAVE CHARACTERISTICS IN AIR, ARGON,
CARBON DIOXIDE, AND HELIUM IN A SHOCK TUBE

WITH UNHEATED HELIUM DRIVER

Charles G. Miller III and Jim J. Jones
Langley Research Center

SUMMARY

Incident shock-wave velocities were measured in the Langley 6-inch expansion tube, operated as a shock tube, with air, argon, carbon dioxide, and helium as test gases. Unheated helium was used as the driver gas, and most data were obtained at pressures of approximately 34 and 54 MN/m². A range of pressure ratio across the diaphragm was obtained by varying the quiescent test-gas pressure from 0.0276 to 34.5 kN/m². Single- and double-diaphragm modes of operation were employed and diaphragms of various materials (aluminum, brass, copper, stainless steel, and plastic) tested. Shock velocities were determined from microwave interferometer measurements, response of pressure transducers positioned along the driven section (time-of-arrival gages), and measured tube-wall pressure.

Comparison of the three methods for determining shock velocity showed that the microwave technique gives better definition of shock-wave characteristics (acceleration-deceleration trends) along the tube and is a viable method provided that microwave reflection occurs at the shock front. However for the present range of flow conditions, the microwave technique proved to be rather limited in application. Shock velocities inferred from time-of-arrival transducers agreed within experimental accuracies with those inferred from measured wall pressures. The time-of-arrival method avoids many of the shortcomings of the other two methods and is believed to be the most acceptable method of those examined. Measured shock velocities were observed to increase initially and then to attenuate with distance from the diaphragm for all test gases. This trend was most pronounced for helium; argon, air, and carbon dioxide experienced successively less attenuation. The distance required for the shock velocity to reach a maximum value increased with increasing pressure ratio across the diaphragm for all test gases. At the higher pressure ratios, the shock velocity remained more nearly constant with distance after the initial acceleration for the present tube length of 29.0 m. Only minor differences in shock velocity were observed between single- and double-diaphragm modes of operation for a given test gas and pressure ratio across the diaphragm. The

ratio of measured maximum shock velocity to predicted velocity was essentially the same for all diaphragm materials tested; however, the distance for the shock to reach a maximum value varied with diaphragm material.

Measured maximum velocities exceeded predictions from conventional shock-tube theory for all test gases. Primary contributing factors to this discrepancy are believed to be (1) the effect of the helium driver temperature increasing upon pressurization of the driver section, (2) effects resulting from the finite opening time of the primary diaphragm, and (3) two-dimensional or nonplanar flow effects. Tests with helium, which also yielded higher than theoretical shock speeds, suggest that interface mixing and flow chemistry are not primary contributors to this discrepancy.

INTRODUCTION

The Langley 6-inch expansion tube was designed for several modes of operation to provide a wide range of velocity-density performance. The first mode of driver operation used in the facility after its initial operation made use of a resistance heater element mounted inside the driver chamber to heat the driver gas (refs. 1 and 2) to temperatures up to 600 K. Tests in this mode showed that incident shock speeds attained were in satisfactory agreement with theoretical one-dimensional prediction. At the conclusion of those tests, a series of tests was made without the driver-gas heater, and surprisingly the shock speeds achieved were only modestly lower than those with the heater. Also, it was noted that the tests without the heater showed significantly higher shock Mach numbers than predicted by theory for a driver temperature of 300 K.

As demonstrated in this report, the theoretical performance of the expansion tube, as predicted by conventional expansion-tube theory, is very sensitive to incident shock velocity in the intermediate section. Thus, in comparing predicted expansion-tube performance with measured performance, it is imperative that the input incident shock velocity be determined accurately. (It is well recognized that accurate measurement of the incident shock velocity in shock tubes is required for determination of the thermochemical conditions in the post-shock test gas.)

The present investigation was undertaken to review and compare the accuracy of various means of determining incident shock velocity and to study more fully the phenomenon of shock strengths which significantly exceeded theoretical prediction. For these tests the secondary diaphragm of the expansion tube was removed and the facility operated as a conventional shock tube with an unheated driver gas. Air, argon, carbon dioxide, and helium were used as test gases because of their probable use in future expansion-tube studies.

Tests were conducted in two phases. After the initial testing phase, improvements were made to increase the precision of shock arrival time measurement, additional stations were added, and a second testing phase was undertaken. The second phase covered a wider range of pressure ratio, included direct measurements of driver temperature, and since the facility configuration had changed in the interim, used a driven-section length of 29.0 m compared with 21.6 m for the first phase.

Data from both series of tests are included in this report. Effects on shock-wave characteristics of (1) pressure ratio across the diaphragm, (2) test gas, (3) pressurization rate of the driver section (i.e., driver-gas temperature), (4) single- or double-diaphragm mode of operation, and (5) diaphragm material are examined. The various methods used to determine shock velocity are compared and relative advantages discussed. Various nonideal effects are examined for their contribution to shock strength.

SYMBOLS

\tilde{A}	ratio of cross-sectional area of driver section to cross-sectional area of driven section
a	speed of sound, m/sec
c_p	specific heat at constant pressure, J/kg-K
d	distance between successive minima or successive maxima on microwave film, m
l	distance from primary diaphragm station to position of maximum incident shock velocity, m
M_s	incident shock Mach number into quiescent test gas, U_s/a_1
$M_{s,c}$	incident shock Mach number calculated by compression model
N_e	electron number density, electrons/cm ³
p	pressure, N/m ²
T	temperature, K

t	diaphragm thickness, m
t_g	diaphragm thickness at groove, m (see fig. 3)
U	velocity, m/sec
U_s	incident shock velocity into quiescent test gas, m/sec
V	volume, m ³
x	axial distance downstream from the primary diaphragm, m
Π	percent increase in shock Mach number (see eq. (4))
ρ	density, kg/m ³
τ	time, sec

Subscripts:

bf	bottle field
calc	calculated
d	driver section
i	interface
m	measured
max	maximum
op	open
1	state of quiescent test gas
2	state of test gas behind incident shock in driven or intermediate section
3	driver-gas conditions following unsteady expansion
4	

- 4 driver-gas conditions at time of primary diaphragm rupture
- 5 state of test-gas flow in acceleration section (free stream)
- 5,t pitot pressure at expansion-tube test section

Abbreviation:

TOA time of arrival

A bar over a symbol denotes average value.

FACILITY AND APPARATUS

The Langley 6-inch expansion tube is a cylindrical tube divided by two diaphragms (primary and secondary) into three sections. (See fig. 1.) The most upstream section is the driver or high-pressure section. This section is pressurized with a gas having a high speed of sound, such as helium. The intermediate section is evacuated and filled with the desired test gas at ambient temperature. The driver and intermediate sections are usually separated by a double-diaphragm apparatus, but a single diaphragm may also be used. The most downstream section is referred to as the expansion or acceleration section and has the same inside diameter (15.24 cm) as the intermediate section. A weak low-pressure diaphragm (secondary diaphragm) separates the driven and acceleration sections. The operating sequence of the expansion tube is shown schematically in figure 1 and is discussed in reference 3.

Results presented herein were obtained with the secondary diaphragm removed; that is, the expansion tube was operated as a shock tube. The length of the driver section was 2.44 m and the inside diameter was 16.51 cm. For the first series of tests, the length of the driven section was 21.6 m, whereas for the second series of tests, it was 29.0 m. The inside diameter of the driven section was 15.24 cm, yielding a ratio of driver-section cross-sectional area to driven-section cross-sectional area of 1.174.

Double-diaphragm mode of operation is generally employed to reduce the randomness in pressure ratio across the primary diaphragm at the time of rupture. For this mode the driver section and double-diaphragm section (the volume between the two primary diaphragms; see fig. 2) are pressurized with the driver gas to a pressure somewhat less than the rupture pressure for a single diaphragm. The double-diaphragm section is then isolated from the driver section and the high-pressure supply field. The driver section is pressurized to the desired pressure, whereupon the double-diaphragm section is opened to atmospheric pressure. This decrease in pressure in the double-

diaphragm section results in rupture of the upstream diaphragm. Upon rupture of this diaphragm, the downstream diaphragm is subjected to a pressure on the driver-section side that is essentially that of the driver section. (The volume of the double-diaphragm section is small compared with the driver section, with the ratio of double-diaphragm-section volume to driver-section volume being approximately 0.07.) This pressure results in the rupture of the downstream diaphragm, and an incident shock wave is propagated into the quiescent test gas.

Figure 3 shows the geometry for metal diaphragms. For most tests, diaphragms were fabricated from commercial plates of AISI type 304 stainless steel. A circular saw blade was used to cut cross-pattern grooves. In the present study, diaphragms used in the double-diaphragm mode were stainless steel and had a thickness t of 3.38 mm or 4.775 mm, and the diaphragm thickness from the bottom of the groove to the side facing the driver section t_g was 2.54 mm or 3.81 mm, respectively. For most tests made with a single diaphragm, t was 4.775 mm and t_g was 3.81 mm. (For all single-diaphragm tests the diaphragm was placed in the downstream position in the double-diaphragm section (fig. 2), to maintain the same plane of initiation of shock formation (x equal to zero) as for the double-diaphragm tests.) Diaphragms with variations in t or t_g exceeding 75 μm were rejected.

Other metal diaphragm materials tested in the single-diaphragm mode of operation were aluminum, brass, and copper. The values of t , t_g , and experimentally determined rupture pressure for the metal diaphragms are presented in the following table. Also presented in this table are the thickness and rupture pressure for a laminated plastic (polyethylene terephthalate) diaphragm. This diaphragm, which was unscribed, consisted of four layers of 0.36-mm-thick plastic and was positioned at the same station as the metal diaphragms.

Diaphragm material	t , mm	t_g , mm	Rupture pressure, MN/m^2
Stainless steel, AISI type 304	4.78	3.81	34.9
Stainless steel, AISI type 304	3.38	2.54	20.7
Stainless steel, AISI type 304	2.08	1.35	9.7
Brass, annealed	3.53	2.39	6.7
Brass, extra spring	2.13	1.27	2.9
Copper, cold roll, light	4.45	3.05	5.4
Aluminum, alloy 6061	3.84	2.57	3.5
Aluminum, alloy 2024	4.93	3.48	5.4
Polyethylene terephthalate, laminated	1.44		2.5

The square double-diaphragm section and the square-to-circular cross-section piece immediately downstream of the double-diaphragm section were modified to accept brass damper pads. (See fig. 2.) These pads have a thickness of 3.18 mm. The pads prevented the tips of the four diaphragm petals formed upon rupture from tearing off and thereby resulted in a significant reduction in debris carried downstream in the post-test flow.

INSTRUMENTATION

Incident Shock Velocity

Microwave Interferometer System

A microwave interferometer system (discussed in detail in ref. 4) was used to introduce microwave energy into the expansion tube, to excite a standing wave in the tube, and to record the movement of this standing wave due to the movement of the termination (region of ionized gas exceeding critical electron density) as a function of time. The varying periodic signal is recorded on a high-speed (60 rps) drum-camera-oscilloscope combination. Representative microwave films for argon, air, and carbon dioxide (CO_2) are shown in figure 4. With helium as the test gas, the temperature immediately behind the incident shock was insufficient for ionization of helium. Hence, no microwave results were obtained, since the electron concentration was not high enough for reflection of the microwave signal.

The antenna for this system for tests with a 21.6-m-long driven section consisted of an uninsulated tin-copper wire having a diameter of 0.61 mm. This wire was stretched horizontally across the tube diameter and positioned approximately 5 cm downstream of the tube exit. A carbon steel drill rod having a diameter of 4.77 mm and protruding 5.08 cm into the tube was used as an antenna for tests with the 29.0-m-long driven section. This antenna was positioned 0.63 m upstream of the tube exit. The signal generator was adjusted to put out a 1.326-GHz signal. Film speed was checked for each test by utilizing a time mark generator to place marks on the film representing 100- μ sec increments.

Time-of-Arrival (TOA) Measurement

A more conventional means of determining incident shock velocity U_s is to position high-frequency-response transducers along the length of the tube at known intervals. This procedure allows a distance-time history to be generated; hence, the average U_s is determined between successive instrumented stations. The time interval for incident shock arrival between stations was determined from the response of piezoelectric (quartz) pressure transducers mounted along the tube flush with the tube wall. At four stations,

thin-film resistance heat-transfer gages and photomultipliers with field stops to collimate the light source served as backup instrumentation. Station locations of pressure transducers in terms of axial distance downstream from the most downstream diaphragm are presented in table I for both driven-section lengths. Outputs from these three types of instrumentation were recorded from an oscilloscope with the aid of a camera, and times for the shock to travel between stations were obtained from manual reading of the oscilloscope film. Each type of instrumentation yields information about the flow behind the shock wave. With the exception of the pressure transducers, this instrumentation was used only to determine time of arrival of the shock wave and is referred to collectively as time-of-arrival transducers. For tests with the 29.0-m-long driven section, 20 counter-timers were also used to obtain a time history of the incident shock. (See table I for locations of stations having counter-timers.)

Reliable triggering of facility recording instrumentation is of primary concern. In the initial tests of the Langley 6-inch expansion tube, it was found that a reliable triggering signal for the oscilloscopes was produced by an accelerometer mounted to the exterior of the double-diaphragm section. This accelerometer detected an acceleration in the axial direction of the tube resulting from the diaphragm rupturing process. (For tests with the plastic diaphragms the accelerometer did not provide an adequate trigger signal; thus the transducer output at station 8 (see table I) was used as a trigger signal.) For tests performed with the 21.6-m-long driven section, the signal from this accelerometer triggered oscilloscopes used to monitor the microwave signal and the output of pressure, heat-transfer, and photomultiplier transducers. Time delays to oscilloscopes monitoring transducers further downstream of the primary diaphragm were supplied by a digital time delay generator and are known to within 1 μ sec. This triggering method is not subject to spurious signals, nor does it require gain adjustments for varying pressure levels.

To enable faster time sweeps of the oscilloscopes monitoring the transducer outputs along the entire tube for the second series of tests (29.0-m-long driven section), output signals from certain transducers were used as trigger signals. These signals triggered downstream oscilloscopes directly or through a digital time delay generator. This more complex triggering system, which required gain adjustments on charge amplifiers processing trigger signals from the pressure transducers for change in test conditions (varying pressure level), performed with relatively good reliability for the present tests. The counter-timers used with the 29.0-m-long driven section were all started by the signal from the accelerometer mounted to the exterior of the double-diaphragm section, and each counter-timer was stopped upon shock arrival by the signal output from the pressure transducer at a given axial station.

Wall-Pressure Measurement

The incident shock velocity at a given station may be computed from the measured wall pressure at that station. (The wall pressure is assumed to be an accurate representation of the static pressure immediately behind the incident shock wave.) Thus, pressure transducers were also employed to measure the driven-section wall pressure with time. Each pressure transducer was used in conjunction with a charge amplifier and was calibrated statically before the test series. The output signal was recorded from an oscilloscope with a camera. Representative oscilloscope films illustrating wall-pressure variation with time at an axial station x of 19.75 m are presented in figure 5 for the three test gases employed in the first series of tests. Because of the larger number of pressure transducers used in the second series of tests and the fact that obtaining accurate pressure measurements is difficult and laborious, pressure instrumentation in the second series of tests was not treated with the same care. Hence, no attempt is made to infer incident shock velocity from wall-pressure measurements in tests with the 29.0-m-long driven section.

Driver-Section Pressure and Temperature

Driver-section and double-diaphragm-section pressures were measured with strain-gage transducers statically calibrated to 68.95 MN/m². Output from these transducers was read visually from a digital voltmeter and recorded on a strip chart. Quiescent test-gas pressure was measured with a variable capacitance diaphragm-type transducer. Driver-section temperature was measured with a bare-wire chromel-alumel thermocouple inserted through the upstream end plate of the driver section approximately 6 cm into the section. The thermocouple junction was exposed directly to the driver gas to provide the fast response required to obtain temperature histories during pressurization of the driver section. This thermocouple output was read from a compensated digital readout and recorded on a strip chart. Quiescent test-gas temperature was measured with a chromel-alumel thermocouple encased in a stainless-steel shroud.

TESTS

For the present tests the helium driver was drawn from a high-pressure supply field at ambient temperature, and no external heat was applied. The actual driver-gas temperatures obtained are discussed in a subsequent section. Approximate driver pressure at the time of diaphragm rupture p_4 was 34 MN/m² or 54 MN/m² for the double-diaphragm tests and 35 MN/m² for the single-diaphragm tests with stainless-steel diaphragms. Dry (bottled) air, and high purity argon, CO₂, and helium were employed

as test gases. The range of pressure ratio across the primary diaphragm, for a given p_4 , was obtained by varying the quiescent test-gas pressure p_1 from 0.0276 to 34.5 kN/m². Tests performed with aluminum, brass, copper, and plastic diaphragms used helium as the test gas, and the pressure ratio across the diaphragm was approximately 10^3 . The driven section was evacuated to approximately 0.01 N/m² before filling with the test gas.

DATA REDUCTION AND UNCERTAINTY

Microwave Interferometer Measurements

For the first series of tests with the 21.6-m-long driven section, the distance between successive minima or successive maxima d of the microwave traces was digitized with a film reader having a calibration factor of 30.11 micrometers per count. The repeatability in reading was within approximately ± 4 counts, or ± 120.44 micrometers. The range of velocity experienced yields d from roughly 3.05 mm to 5.08 mm; the corresponding maximum uncertainty due to this error in reading between successive cycles is 4.0 and 2.4 percent, respectively. Although microwave traces obtained in the second series of tests were digitized with a film reader having a different calibration factor, the uncertainties due to film reading are expected to be the same as for the first series. However, because the microwave traces were read every other cycle in the second series of tests, the uncertainty in velocity due to reading of the film was reduced. By running a brass plug down an accurately determined length of the expansion tube and counting cycles, d was found to correspond to a movement of 22.71 cm. Since 5.08 cm of film corresponds to 1 msec, the time between successive minima or successive maxima is given by

$$\Delta\tau = \frac{d}{5.08 \text{ cm/msec}} \quad (1)$$

where d is expressed in centimeters. The corresponding velocity, in m/sec, is given by

$$U = \frac{227.1 \text{ mm}}{\Delta\tau} \quad (2)$$

where $\Delta\tau$ is expressed in milliseconds. Uncertainties in the microwave system due to film speed variation, film resolution, and film length stability are discussed in reference 4 and contribute a maximum error of less than 0.75 percent. Consideration of all sources of errors in measuring incremental velocities is believed to result in a maximum uncertainty in velocity of 3 percent at the lower velocities of this study and 4.5 percent at the higher velocities. It should be emphasized that these uncertainties refer to

measurement of the velocity of an ionization front which has reached a critical electron density. (This critical density is 2.18×10^{10} electrons/cm³ for the present microwave system.) An additional, possibly large, uncertainty may result if this critical density does not coincide with the incident shock front.

Time of Arrival

An average velocity between stations was determined by knowing the distance between stations and the time for the shock wave to travel this distance. These times were obtained from the response of pressure transducers along the driven section, the output of which was recorded on oscilloscope films and displayed on counter-timers. Uncertainties in pressure transducer response, oscilloscope time scale, and reading of oscilloscope film are believed to result in a corresponding uncertainty in time interval between arrival of the shock wave at successive stations of less than $\pm 10 \mu\text{sec}$ for the first series of tests and $\pm 5 \mu\text{sec}$ for the second series. Uncertainty in oscilloscope time scale was reduced by using a timing mark generator to supply a known time increment to the oscilloscope. If necessary, a correction was applied to film readings. With one exception, oscilloscope time scales were accurate to within 3.75 percent. The principal sources of error for times obtained from the counter-timers are response of the pressure transducers and associated equipment and counter-timer sensitivity to this response. For example, at the lower values of incident shock velocity, disturbances resulting from rupture of the thick steel diaphragms propagated through the tube wall and preceded the arrival of the incident shock. In this case, many of the pressure transducers responded to these acceleration effects, thereby producing a premature stop of the counter-timers. At the higher values of incident shock velocity, the static pressure level behind the incident shock was often too low to provide sufficient output from the charge amplifier of the pressure transducer to stop the counter-timer. In this case the stop would correspond to flow in the higher pressure region of the expansion fan and hence yield a delayed stop signal. Counter times which were obviously erroneous were eliminated from the data, and the velocity was averaged between the adjacent stations. For both the oscilloscope films and the counter-timer readings, uncertainties in shock velocity inferred from TOA transducers depend on the distance between successive stations, being larger for stations closer together. The zero time for these distance-time plots was also obtained from the accelerometer signal. Randomness involved in the accelerometer signal results in a shift in the time scale between individual tests.

Wall Pressure

A third method employed to infer U_s was to use the measured driven-section wall pressure p_2 as input to the shock-tube phase of the computer program of reference 5 (in conjunction with measured p_1 and T_1). Experimental uncertainties in p_2

are dependent on many factors, such as transducer sensitivity, calibration technique (static or dynamic), transducer linearity, transducer mounting, adequate thermal protection, oscilloscope accuracy, quality of oscilloscope traces with respect to the signal-noise ratio, and oscilloscope film reading procedure. The maximum uncertainty in p_2 for the tests in the first series is believed to be less than 10 percent. For the conditions of this study the uncertainty in U_s is roughly half that of the corresponding p_2 .

RESULTS AND DISCUSSION

Effect of Uncertainty in Incident Shock Velocity on Predicted Expansion-Tube Performance

For any shock tube or shock-tube-related device such as the expansion tube, it is well-known that an accurate determination of the incident shock velocity U_s is required for determination of the thermochemical state of the post-shock gas. In expansion-tube operation, measurement accuracy of U_s acquires additional importance because of the multiplying effect of the subsequent expansion. The expansion fan which passes through the shocked gas raises the gas to a higher velocity while expanding it to a lower pressure and temperature. This final state after expansion is dependent on the enthalpy of the gas entering the fan. Rather small differences in this initial enthalpy can result in large differences in the final state of the gas exiting the fan.

Examples of the effect of uncertainty in U_s on predicted expansion-tube flow quantities for air, argon, CO_2 , and helium as test gases are shown in figure 6. The free-stream static pressure p_5 and pitot pressure $p_{5,t}$ are shown as functions of free-stream velocity U_5 . These results were calculated with the conventional expansion-tube program of reference 5 for thermochemical-equilibrium flow and no shock reflection at the secondary diaphragm. The calculations are for values of incident shock velocity U_s which correspond to those attained in the Langley 6-inch expansion tube for an unheated helium driver pressure of 34 MN/m^2 . An uncertainty in U_s of 5 percent is assigned for each gas.

The effect of this uncertainty in U_s on predicted free-stream static pressure and pitot pressure is illustrated by the shaded region in figure 6. The region of uncertainty is magnified as the gas expands to higher velocity. At a velocity of 5.5 km/sec, typical of expansion-tube operation, the uncertainty in static pressure ranges from about 30 to 70 percent for the various gases, and the uncertainty in pitot pressure varies from about 20 to 45 percent. Thus, relatively small uncertainties in input U_s result in much larger uncertainties in predicted p_5 and $p_{5,t}$ for a given flow velocity. Hence, to minimize uncertainties in predicted expansion-tube test-section flow conditions, the incident shock velocity U_s should be measured as accurately as possible.

Comparison of Methods for Measuring Incident Shock Velocity

TOA data from counter-timer readings and from oscilloscope film readings are presented in figures 7, 8, 9, and 10 for air, argon, CO_2 , and helium as test gases, respectively. In these figures the incident shock velocity U_s is plotted as a function of axial distance x downstream from the primary diaphragm for various values of quiescent test-gas pressure p_1 . Horizontal filled bars denote the average velocity between successive stations from oscilloscope film; horizontal open bars denote the average velocity determined from counter-timer readings. Also shown in these figures are values of U_s determined from microwave measurements. These microwave data were read every other cycle and are connected by line segments. The results of figures 7 to 10 were obtained with the double-diaphragm mode of operation and a helium driver pressure of approximately 34 MN/m^2 .

Microwave results were not obtained at the higher values of quiescent test-gas pressure p_1 for air (fig. 7) and CO_2 (fig. 9), nor for helium (fig. 10) at any test value of p_1 . This absence of microwave data at these conditions is due to insufficient electron density at the shock front or in the post-shock flow region to terminate the microwave signal. Ideally, TOA data from counter-timer readings should agree with data from oscilloscope films for a given test. The differences observed in figures 7 to 10 between these two TOA methods are indicative of the present experimental uncertainties, which in turn are dependent on limitations of the methods. For example, at the higher values of p_1 for all test gases (corresponding to the lower values of U_s), disturbance created by the rupture of the thick steel diaphragms propagated downstream through the tube wall and preceded the arrival of the incident shock. Several pressure transducers experienced rather severe acceleration effects because of this propagation, and the resulting output from the transducers caused a premature stop of the counter-timers. These same acceleration effects on pressure transducer outputs used to trigger downstream oscilloscopes resulted in erroneous triggering. The high noise-signal ratio also led to difficulty in reading the time of arrival of the incident shock from oscilloscope film. At the lower values of p_1 , the incident shock preceded disturbances in the tube wall, but the pressure immediately behind the shock was sometimes insufficient to provide adequate output from the charge amplifier of the pressure transducer to stop the counter-timers on arrival of the shock or to trigger oscilloscopes.

Relatively good quality microwave film traces were obtained for air at values of p_1 less than 3.45 kN/m^2 . As observed in figure 7, the microwave method provides more detailed information on the shock travel, since an amplitude peak occurs for every 22.71-cm movement of the front being tracked. This small increment, which is equal to 45.42 cm in figures 7 to 9 since every other cycle of the microwave trace was read, means that a given uncertainty in the time increment Δt results in relatively large

uncertainties in the corresponding velocities. The percent uncertainty in $\Delta\tau$ increases with increasing shock velocity (see the section entitled 'Data Reduction and Uncertainty'); hence the scatter in microwave data is expected to increase with decreasing p_1 . At values of p_1 for which good microwave traces were obtained in air, the shock velocities from the microwave measurements generally were somewhat lower than shock velocities obtained from the TOA method.

Microwave film traces for the argon tests displayed good signal amplitude for all values of quiescent test-gas pressure. As shown in figure 8, shock velocities from the microwave method and TOA method are in good agreement for values of p_1 between 34.5 and 3.45 kN/m². However, at the higher shock velocities corresponding to values of p_1 of 0.69 and 0.345 kN/m², large discrepancies exist between the two methods for determining U_s . The microwave results for these two values of p_1 are suspect, from the viewpoint of the trend of U_s with x and the fact that the peak values of U_s exceed the theoretical limiting value (the value of U_s as p_4/p_1 approaches infinity). As the quiescent pressure is decreased further to 0.069 and 0.0345 kN/m², the agreement between the two methods improves markedly, but the scatter in U_s inferred from microwave measurements is significantly larger than the scatter observed at the higher values of p_1 , as expected.

Microwave film traces for CO₂ tests were characterized by low amplitude and were frequently irregular. As for air, shock velocities from the microwave method for CO₂ (fig. 9) were generally less than those determined from TOA data. The absence of microwave data for helium (fig. 10) is expected, since (1) the range of shock velocity was insufficient to ionize the helium and (2) the photomultipliers failed to show any light emitted from the helium, and thus the test gas was assumed to be essentially free of contaminants which are more readily ionized.

TOA data and microwave data can also be conveniently compared on a plot of time of incident shock arrival as a function of axial distance downstream of the primary diaphragm. Such plots, referred to herein as distance-time diagrams, are shown in figure 11 for air, argon, and CO₂ and for selected values of quiescent test-gas pressure. The microwave data were forced to agree with the TOA data at the 5.377-m station or 11.640-m station. (Because the accelerometer was used as a trigger for the microwave interferometer system, the microwave data lack an absolute reference point. On the two drum-camera-oscilloscope systems used to record the microwave signal, the signal from the pressure transducer at x equal to 5.377 m was placed on one film and the signal from the pressure transducer at x equal to 11.640 m on the other.) Although the scales of figure 11 are relatively coarse (for example, the symbol width for TOA data corresponds to approximately 2 cycles on the microwave trace), these distance-time diagrams show that TOA and microwave measurements do not generally agree as to the

position of the shock front at a given time over the entire distance traversed by the shock. Examples of particularly poor agreement are shown for argon at p_1 equal to 0.345 kN/m^2 (fig. 11(b)) and for CO_2 at this same value of p_1 (fig. 11(c)). The observed discrepancy between microwave and TOA data at other values of p_1 for these two test gases and for air exceeds the uncertainties in measurement. Although the point of forced agreement on the distance-time diagrams is arbitrary, selection of a different adjustment point will not bring the data into agreement for the entire traverse of the shock wave. It seems obvious that the microwave signal sometimes reflects from a region other than the pressure front.

As noted previously, microwave measurements with the present system were not possible for helium tests and tests with air and CO_2 at the higher values of quiescent test-gas pressure. In table II, the maximum and final (near driven-section exit) incident shock velocities for a range of p_1 for each test gas are tabulated. These results were obtained from the TOA data of figures 7 to 10. Also tabulated are predicted electron number densities corresponding to the maximum and final shock velocities for a given p_1 . These electron densities were calculated by the thermochemical-equilibrium program of reference 5. For the microwave signal to be terminated, an electron density of $2.18 \times 10^{10} \text{ electrons/cm}^3$ is required. Hence, the results of this table illustrate that insufficient electron densities were present to provide microwave termination for the cases previously mentioned. According to the data of table II, sufficient electron density existed for the argon tests. However, at values of p_1 of 0.69 and 0.345 kN/m^2 , the microwave data exhibited a departure from the TOA data not observed for the other test gases, nor for other values of p_1 for argon. At these two values of p_1 , the microwave signal is terminated at something other than the shock front.

Immediately behind the shock front, translational degrees of freedom are excited within several collision times, whereas excitation of internal degrees of freedom, dissociation, and ionization take many more collisions. Thus, a relaxation zone is produced immediately behind the shock front. For argon, electron production proceeds initially by atom-atom collisions and collisions of electrons from impurities with atoms until sufficient electrons exist for electron-atom collisions. Hence, relatively few electrons exist at the shock front, and the equilibrium degree of ionization can occur at a significant distance behind the shock front. (See, for example, refs. 6, 7, and 8.) Measurements associated with the chemistry of shocks into argon are beyond the scope of this study. A possible explanation for the difference observed between the microwave and TOA data for argon at p_1 of 0.69 and 0.345 kN/m^2 is that these conditions correspond to an appreciable departure from equilibrium resulting in an electron density deficiency in the relaxation zone. At the lower values of p_1 , the role of impurities in generating electrons may become more significant. (See refs. 7, 8, and 9.) The supply of argon used

in the present study was 99.998 percent pure, but outgasing of the tube and dump tank walls and leaks in the vacuum system may have introduced a significant impurity level. This level could have an appreciable effect on the microwave measurements in argon, where high temperatures were generated in the post-shock flow region. (See table II.) Whereas flow impurities may have a significant effect on the electron density, the corresponding effect on shock velocity and thermodynamic properties in region (2) (see fig. 1) may be negligible. For example, a test relating to another investigation was performed in which a mixture of 98 percent argon and 2 percent methane was used at a p_1 of 6.9 kN/m^2 and p_4 of 34 MN/m^2 . With the exception of the photomultiplier traces, no appreciable difference was detected between this test and a similar test with pure argon.

Prior to a series of expansion-tube tests, pressure transducers mounted along the tube wall are usually dynamically calibrated by employing the facility as a low-performance shock tube. For such checks on the static calibration of the transducers and on thermal insulation of the transducer sensing surface, a plastic diaphragm is used to avoid generation of tube-wall disturbances and to minimize cost of operation. This procedure was reversed in the present study in that shock velocities were determined from measured wall pressures. For a given axial station, the pressure measured immediately behind the incident shock was used as input to the program of reference 5 to calculate the corresponding shock velocity. In figure 12, values of U_s calculated from tube-wall pressure measurements for air, argon, and CO_2 are compared with shock velocities determined from microwave measurements and TOA data. These sample data were obtained with the 21.6-m-long driven section, double-diaphragm mode of operation, and a helium driver pressure of approximately 34 MN/m^2 . For the most part, values of shock velocity inferred from TOA data and pressure data agree within the experimental accuracy, as do the microwave data for air and CO_2 .

Thus, comparison of the three methods for determining shock velocity shows that the dependence of the microwave technique on electron density at the shock front limits its range of applicability for a study such as this one employing a number of test gases over a range of shock velocity. Use of the microwave technique should always be accompanied by TOA transducer information to verify its validity, since good quality microwave film traces (indicating termination of the microwave signal) did not always yield a position of reflection that was in agreement with the pressure front. In its range of validity, the microwave technique is a useful tool because it yields better definition of shock-wave acceleration-deceleration characteristics than practical with TOA transducers. Of the two other methods, the TOA method is believed to be more desirable than the pressure method, since less effort is required to obtain shock velocity with this method and the pressure method has less potential for improvement. Factors contributing to the greater effort for the pressure method are: (1) frequent and careful calibrations of the pressure

transducers and associated charge amplifiers and oscilloscopes are required; (2) care must be exercised in mounting the transducers to insure that the sensing surface is flush with the tube wall, that adequate thermal insulation for the transducers is provided, and that the mounting procedure reduces acceleration effects resulting from disturbances transmitted along the tube wall; and (3) signal noise levels and trace characteristics require judgments to be made in reading the outputs. The inferred pressures must then be used as inputs to a program such as reference 5 to determine corresponding values of shock velocity. The accuracy of this technique is believed to be limited to about 5 percent in shock velocity.

Although pressure transducers were used herein for the TOA method, thin-film resistance transducers are preferable, since they have a faster response to shock arrival and a wide range of flow conditions for which they give good definition of the shock position, they are not influenced by disturbances propagating through the tube wall, and they provide a better signal-noise ratio. However, wall-pressure measurements are basic in expansion-tube testing, and it was not feasible to replace existing pressure transducers with heat-transfer transducers in the Langley 6-inch expansion tube for the present shock-tube tests.

Comparison of Measured Shock Velocity With Theory

As observed for all four test gases (figs. 7 to 10) and in most shock-tube studies (for example, refs. 10 to 14), the incident shock initially accelerates for some distance down the tube, reaches a maximum value $U_{s,max}$, and then decelerates for the remainder of its travel. The principal cause of the acceleration phase is the finite opening time of the diaphragm, which causes the shock wave to be formed and strengthened by a family of compression waves which emanate from the diaphragm location as the open area increases with time. The dominant cause of the deceleration phase is the growth of the wall boundary layer, although the diaphragm opening process may also make a small contribution to this deceleration.

As the higher values of pressure ratio across the diaphragm p_4/p_1 are approached, the incident shock velocity tends to remain more constant with distance x after the initial acceleration for the driven-section length of 29.0 m. The deceleration phase is not examined in detail in the present study. Linear fits to the downstream portion of the velocity-distance data of figures 7 to 10 revealed that helium suffers the most severe attenuation. Argon, air, and CO_2 experience successively less attenuation.

The distance l required for the shock wave to reach $U_{s,max}$ is a function of the time required for the diaphragm to open. The characteristic wave which originates from the diaphragm location at the instant of complete opening may be viewed as the completion of the shock-strengthening wave family. The distance downstream of the diaphragm

where this characteristic wave overtakes the incident shock wave represents the distance l , provided attenuation effects are ignored. An approximate method of estimating the distance l (for example, refs. 11 and 12) has been employed in which l is assumed to be proportional to the product of the diaphragm opening time and the maximum shock velocity. The constant of proportionality is determined empirically and the resulting simple relations from references 11 and 12 are shown graphically in figure 13. The shaded region of figure 13 denotes the present data for all four test gases. The relatively large size of the shaded region is due to data scatter and uncertainty in defining l and $U_{s,max}$ from figures 7 to 10. Diaphragm opening time τ_{op} was not measured in the present study, and predicted values for the stainless-steel diaphragms varied considerably according to the method of calculation. For the present diaphragm thickness and opening area, the method of reference 15 is believed to provide a reasonably accurate value of τ_{op} . The diaphragm opening time predicted from the method of reference 15 is approximately 500 μ sec, and this value is assumed in presenting the data of figure 13. The dashed lines of figure 13 denote the regions for which the empirical relations of references 11 and 12 were obtained. As observed from this figure, the present results represent a large extension in the range of l of these previous studies. At the lower values of pressure ratio p_4/p_1 (that is, lower values of U_s) of this investigation, the present data and the relation of reference 11 are in reasonably good agreement. However, as the pressure ratio increases, the present values of l increase and for a given $\tau_{op}U_{s,max}$, exceed values calculated from the relation of reference 11. Because of the uncertainty in predicted opening time τ_{op} , as well as uncertainties in determining $U_{s,max}$ and l , no definite conclusions may be drawn. However, this comparison suggests that the relations of references 11 and 12 are not valid over the wide range of test conditions obtained in the present facility and should be used with discretion.

Comparison With Conventional Theory

The dashed lines in figures 7 to 10 represent the predicted shock velocity from conventional shock-tube theory for each given diaphragm pressure ratio. This conventional theory assumes one-dimensional, constant-area, inviscid flow and thus includes no mechanism for shock attenuation. Instantaneous diaphragm rupture and shock formation are assumed, and both driver-gas and driven-gas initial temperatures (T_4 and T_1 , respectively) were taken to be 298 K. The computations assumed equilibrium real-gas properties for the shocked test gases and considered imperfect-gas effects for the helium driver. In all cases, the measured maximum shock velocity exceeds prediction. Because of attenuation, which is attributed primarily to viscous effects, agreement between predicted and measured velocities improves near the tube exit, but in many cases the final velocity at the end of the tube still exceeded the prediction from conventional theory.

Experimental shock velocities which exceed conventional shock-tube theory have been previously noted in the literature. For example, in reference 16 for diaphragm pressure ratios larger than 10^6 , the measured shock velocities obtained with a combustion driver approached twice the theoretical value. In reference 17 with an unheated helium driver, measured velocities exceeded conventional shock-tube theory by as much as 25 percent. In reference 10 unheated helium and hydrogen driver gases are shown to produce higher shock velocities than predicted for nitrogen, oxygen, air, or argon as driven gases.

A far greater number of sources could be cited for which the shock velocity does not exceed prediction, so apparently the conditions which cause this effect are not usually dominant. In the following section, several possible causes for the shock velocity being greater than predicted are examined.

Causes of Discrepancy

Driver temperature. - It is well-known that the driver temperature T_4 strongly influences the shock strength. (See ref. 18.) Since both the high-pressure helium storage bottle field and the driver section were at ambient temperature, the ambient temperature of the driver section was used in the predictions illustrated in figures 7 to 10. However, the Joule-Thomson coefficient is negative for helium in this temperature range, and the expansion of helium from the storage field into the driver section results in a temperature rise. In addition to the Joule-Thomson heating, a compression heating occurs since the helium in the driver section is continuously being compressed during the charging process. If this additional temperature is not lost by heat transfer to the driver-section walls prior to diaphragm rupture, a more effective driver condition results. The temperature-time history of the helium during pressurization of the driver section was monitored for each test with the 29.0-m-long driven section. In figure 14 the maximum driver temperature recorded during pressurization is plotted as a function of supply pressure in the helium bottle field for a number of tests. This figure demonstrates that values of $T_{d,max}$ during pressurization were frequently over 340 K. A least-squares fit to the data of figure 14 illustrates the trend of increasing $T_{d,max}$ with increasing bottle-field pressure.

An example of driver-section pressure and temperature variation with pressurization time is shown in figure 15. For this example, the driver section was charged to about 30 MN/m^2 and then isolated from the bottle field for an additional 2 min. During the charging time the driver-gas temperature, as measured by the thermocouple, remained between 330 K and 340 K. When the supply valve to the bottle field is closed, the temperature decays to the ambient driver-section wall temperature because of heat

loss. Since the density is constant after the valve is closed, a corresponding decrease in pressure occurs.

In normal double-diaphragm operation the diaphragm rupture generally occurs approximately 5 to 10 sec after closing the supply valve. On each run, driver pressure and temperature were noted at the time of diaphragm rupture. These values of pressure p_4 and temperature T_4 were used as inputs in the theoretical computations of shock velocity by the method of reference 5 and are indicated in figures 7 to 10 by the long-short dashed lines ($T_4 = T_{4,m}$).

The calculated effect of driver temperature for all four test gases is shown in figure 16, in which the ratio of driver-section pressure to quiescent test-gas pressure is plotted as a function of incident shock Mach number $M_s = U_s/a_1$. The measured values of T_4 and p_4 were used as input to the conventional shock-tube method of reference 5 to predict the shock Mach number for each test. The solid lines of figure 16 represent a fairing of these predicted values of M_s . For comparison, similar predictions using a value of T_4 of 298 K are shown, along with the measured maximum shock Mach number. The effect of driver temperature is observed to be insufficient to explain the differences between measured and predicted shock velocities. Also shown in figure 16 are the measured maximum shock Mach numbers for double-diaphragm tests in which the driver pressure was increased to approximately 54 MN/m². These higher values of p_4 were obtained to extend the range of p_4/p_1 and to determine whether any effect on maximum shock Mach number resulted from operation at a higher driver pressure. No significant effect of pressure level on shock velocity is observed.

It is interesting to note that measured values of maximum shock Mach number for air (fig. 16(a)) and CO₂ (fig. 16(c)) are amenable to a straight-line fit on a semilogarithmic plot. The resulting expressions are:

For air,

$$M_{s,max} \approx 0.92 \log_e \frac{p_4}{p_1} - 0.3 \quad (3a)$$

For CO₂,

$$M_{s,max} \approx 1.2 \log_e \frac{p_4}{p_1} - 1.56 \quad (3b)$$

These relations for air and CO₂ describe the experimental results presented in figure 16 to within 3.5 and 3 percent, respectively. Such simple expressions may be readily incorporated into the program of reference 5, and thereby permit a more accurate prediction of expansion-tube performance for these two test gases than previously possible

by using inputs p_4 and T_4 to determine the incident shock velocity in the intermediate section. It should be emphasized that these relations are not general and discretion must be exercised in usage for other shock tubes.

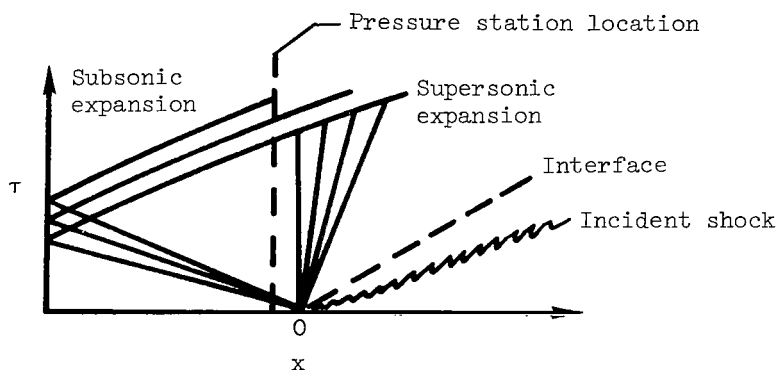
The effect of driver temperature on shock velocity was verified experimentally by varying the pressurization time of the driver section. A number of tests were performed in which the driver gas was allowed to return to near ambient temperature before initiating diaphragm rupture. For these "slow-charge" tests, additional helium was added as needed to make up the pressure loss due to cooling. The resultant shock velocities from these slow-charge tests are compared in figure 17 with "fast-charge" tests with air and helium and for several values of quiescent test-gas pressure. These data illustrate that the higher driver temperature due to fast charge increases the shock velocity, as expected. The velocity difference between the two charge rates is essentially constant down the length of the driven section, and shock attenuation does not appear to be significantly affected by this difference in driver temperature. As observed from figure 7 for air and figure 10 for helium, conventional shock-tube theory predicts a difference in shock velocity (Mach number) roughly the same as observed experimentally for this temperature change. Although elevated driver temperature is a contributing factor, it does not fully account for the discrepancy between experiment and theory.

Single- or double-diaphragm mode of operation. - With the double-diaphragm mode of operation, the test is initiated by venting the chamber between diaphragms, which causes first the upstream and then the downstream diaphragm to rupture, since each one successively feels the entire driver pressure. This arrangement is not unlike a three-chamber shock tube which is generally called a buffered shock tube. Buffered shock tubes have been shown (ref. 19) to produce stronger incident shocks in the driven section than single-diaphragm shock tubes for equivalent driver- and driven-section initial conditions. This effect seems unlikely in the present tests since the chamber between the diaphragms is only 15 cm long. In order to check this effect, a number of tests were made for all four test gases with a single diaphragm. These results are compared in figure 18 with double-diaphragm results. For several tests shown in figure 18, particularly at the highest diaphragm pressure ratios, the shock velocities for double-diaphragm tests reach a higher peak somewhat sooner (that is, at slightly smaller distance traveled). However, as a group, the shock velocities are in good agreement for the two operation modes. It is concluded that the diaphragm mode used has only minor effects on shock velocity.

To learn whether the driver expansion process was significantly affected by the double-diaphragm arrangement, a pressure transducer was mounted in the driver-section wall a short distance (12.7 cm) upstream of the most upstream diaphragm station. Figure 19 compares the pressure histories for single-diaphragm and double-diaphragm

operation. The data were obtained from a digital data storage unit operated in the "pretrigger" mode, wherein the stored data include those measured just prior to the trigger signal. This allowed the preservation of the base line and early pressure decay even though the trigger signal was derived from the pressure decay.

The dotted curve in figure 19 is the experimental driver pressure for a single-diaphragm test. Time equal to zero is an arbitrary time prior to diaphragm rupture. The pressure decay down to about 15 MN/m^2 is observed to be in good agreement with that calculated for a centered unsteady expansion (dashed curve). At about 15 MN/m^2 the pressure levels out, since, because of the larger cross-sectional area of the driver compared with the driven section, the unsteady expansion is not continuous to a Mach number of 1. (See the following sketch.) The pressure begins to decay again when the expansion, reflected from the upstream end of the driver section, crosses the pressure port.



The solid curve of figure 19, taken from a double-diaphragm test, is in good agreement with the single-diaphragm results if the time scales are aligned as shown. The first pressure drop with the double diaphragm undoubtedly occurs as a result of the rupture of the upstream diaphragm. A recompression occurs because the second diaphragm has not yet ruptured; but when it ruptures, the expansion process is very similar to that for the single diaphragm. The weak shock which moves upstream as a result of the recompression has apparently been attenuated before passing the pressure port again.

These results illustrate the similarity of the driver expansion process for single- and double-diaphragm operation and support the previous conclusion that the diaphragm mode of operation has little effect on shock strength.

Diaphragm material. - Several tests were performed with single diaphragms of different material and thickness. Results of these tests are shown in figure 20, in which the average incident shock velocity between successive stations is plotted as a function of distance downstream of the diaphragm. Values of t , t_g , and experimentally determined rupture pressure for the various diaphragms are presented in a previous section entitled

"Facility and Apparatus." Whereas the scribed aluminum, brass, copper, and stainless-steel diaphragms opened into and conformed with the square-to-round transition section shown in figure 2, the unscribed plastic diaphragms opened into an essentially round orifice and thus did not conform to the wall of the transition section. Helium was employed as the test gas because of its ideal-gas behavior and because of the fact that of the four test gases examined, only helium exhibited significant differences between measured and predicted values of maximum incident shock Mach number at pressure ratios as low as 10^3 . (See fig. 16.) Because of the lower rupture pressure of the diaphragms considered in figure 20, it was necessary to test at a low pressure ratio (hence relatively high value of p_1) to avoid instrumentation difficulties with the TOA method as discussed previously. For all tests presented in figure 20, the driver temperature T_4 was within 2 percent of 333 K and the pressure ratio p_4/p_1 was within 9 percent of 1030. The initial acceleration to a maximum shock velocity and subsequent deceleration are observed for all diaphragm materials. The stainless-steel diaphragm and the plastic diaphragm yield the maximum shock velocity at a smaller distance l downstream of the diaphragm than the other three diaphragm materials. The expression of reference 11 was used to predict estimates of relative diaphragm opening times for the various materials. The fact that diaphragms having the fastest predicted opening times (plastic and stainless steel) yield the smallest values of l indicates an effect of diaphragm opening characteristics. Comparison of experiment with prediction (dashed lines of fig. 20 represent conventional shock-tube theory with measured p_4 , T_4 , p_1 , and T_1 inputs) reveals that the measured maximum shock velocity is 1.08 to 1.11 times the predicted shock velocity for all diaphragms. The lowest values of $U_{s,max}/U_{s,calc}$ occur with brass and copper diaphragms. For all diaphragms, the measured shock velocity exceeds prediction in the first 16 to 22 m of travel.

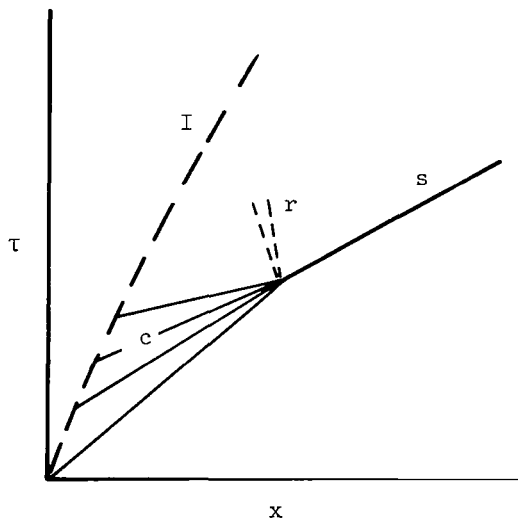
Diaphragm opening time. - As noted previously, White (ref. 10) reported shock velocities which were greater than predicted by conventional theory. White attributed this difference to the influence of the finite time required to open the diaphragm. Conventional theory assumed that the diaphragm opens instantly, with immediate shock formation. However, if a diaphragm is relatively thick and massive, it may require several hundred microseconds to open fully. During this opening, compression waves are generated which coalesce into a shock some distance downstream. The resulting shock wave is stronger than the instantly formed shock.

Formation-from-compression predictions: White solved the special problem in which all the compression waves formed a centered compression fan. The interface was assumed to accelerate in such a way that the compressions all coalesced at the same axial station to form a shock wave. This assumption simplifies the calculation since the driven gas is processed either by isentropic waves only or by shock only.

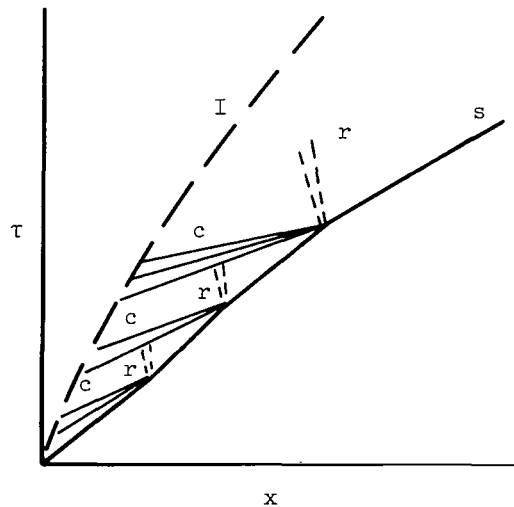
Ikui, Matsuo, and Nagai (ref. 20) solved a more general problem, in which an arbitrary number of convergence points were allowed. The accompanying sketch illustrates, in the distance-time plane, these two solution methods.

I Interface
s Shock wave
c Compression wave
r Reflected wave

Centered compression (ref. 10)



Multiple-step compression (ref. 20)



The following assumptions inhibit the accuracy or completeness of these solution methods:

(1) The reflection waves, denoted r in the sketch, which result from the interaction of the compression wave and the shock, are computed, but the interaction of this reflection with the interface is ignored. This interaction results in a change in the interface speed, a transmitted upstream-facing wave into the driver gas, and a downstream-facing wave which catches the shock and modifies its strength.

(2) The interface is assumed to be the generating surface of the compression waves, whereas in fact the waves originate at the diaphragm station as a result of variation in area as the diaphragm opens. This assumption causes negligible error in the calculation of shock strength, but it does prevent a description of the wave process in the expanded driver gas and divorces the interface acceleration from its cause, the diaphragm opening.

(3) White (ref. 10) uses real-gas properties for the driven gas, but Ikui, Matsuo, and Nagai (ref. 20) confined their calculations to ideal gases. None of these authors performed their calculations for CO_2 or helium as driven gases.

The function Π was defined in reference 20 as the percent increase in shock Mach number due to formation from compression. Figure 21 shows the values of Π for driver-driven gas combinations of helium-air, helium-argon, helium-CO₂, and helium-helium. Both the method of reference 10 (single compression step) and that of reference 20 (multiple compression step) are shown in figure 21. The curves for helium-air and helium-argon are taken from reference 20 and those for helium-CO₂ and helium-helium were computed. Since Π is defined by

$$\Pi \equiv \frac{100(M_{S,c} - M_S)}{M_S} \quad (4)$$

the corrected shock Mach number at a given diaphragm pressure ratio p_4/p_1 is given by

$$M_{S,c} = M_S \left(1 + \frac{\Pi}{100} \right)$$

Although derived for $\tilde{A} = 1$, $T_4 = 300$ K, and perfect gases, the Π correction factors have been applied in the present case for $\tilde{A} = 1.17$, $T_4 = 330$ K, and real gases. (The effects of an area change near the diaphragm are discussed in ref. 21.) These various predictions of shock Mach number as a function of diaphragm pressure ratio are shown in figure 22, together with the measured values of maximum shock Mach number from both phases of the present study, double- and single-diaphragm modes of operation, fast and slow charge of driver section, and two values of driver pressure. Although measured values of $M_{S,max}$ are in better agreement with predictions from the formation-from-compression theories, the experimental values of $M_{S,max}$, with the exception of the argon data, still exceed these predictions at the higher values of p_4/p_1 .

Unsteady flow analyses: The method of characteristics was used to obtain a solution for the flow development with a finite diaphragm opening time. The purpose was to compare the predicted location of the maximum shock velocity with experiment and to compare the measured pressure rise in the driver expansion fan with theoretical predictions for instantaneous and finite opening of diaphragms.

Helium was selected as the test gas for the calculations so that perfect-gas relations could be used without loss of accuracy. The initial conditions correspond to the data illustrated in figure 10(b), for which p_4 is 32.7 MN/m², T_4 is 345 K, and p_1 is 6.9 kN/m² (run 585 in table II). To initiate the characteristic solution, the diaphragm was assumed to open in a stepwise manner; that is, the ratio of the cross-sectional area of the opened portion of the diaphragm to the tube cross-sectional area increased by 0.1 in ten equally spaced time steps. (In other words, the diaphragm opening was modeled in a manner in which the open area increased linearly with time.) It was also assumed that

the partially opened diaphragm represented a Laval nozzle for which quasi-steady flow existed immediately upstream and downstream of the nozzle throat. The boundary conditions at the diaphragm location were determined from the upstream and downstream quasi-steady flow Mach numbers calculated by using the assumed time history of the area ratio.

A diagram in the distance-time plane is shown in figure 23 for a diaphragm opening time of $200 \mu\text{sec}$. Each downstream-facing compression wave interacts with the interface and, upon reaching the shock wave, increases its strength. Thus, the shock-processed test gas displays a varying entropy because of varying shock strength with time. At the interaction of each compression wave with the shock wave, a reflected upstream-facing wave is produced. Although these relatively weak reflected waves were computed, their subsequent effect on the interface was ignored. In figure 23, the calculated shock wave reaches a maximum velocity at a distance x of approximately 9 m. (The subsequent decay of the shock wave is not computed because of neglect of the reflection waves.)

A finite-difference scheme to solve the one-dimensional Navier-Stokes equations for the finite diaphragm opening time problem was also used. This solution, generated by Weilmuenster (ref. 22), is a shock smearing method which uses a Lax-Wendroff differencing technique. The trajectory of the shock wave computed from this finite-difference scheme with an assumed opening time of $200 \mu\text{sec}$ is also shown in figure 23. As for the method-of-characteristics solution, the ratio of diaphragm opening cross-sectional area to tube cross-sectional area was assumed to increase linearly with time. The two theoretical predictions of shock position as a function of time τ are observed to be in good agreement. However, both predictions yield shock trajectories which trail experiment after the first 3 m or so. This is illustrated more clearly in figure 24.

In figure 24, shock velocities predicted by the method of characteristics and the finite-difference scheme for helium as the test gas are compared with experiment. The characteristics solution and finite-difference solution yield values of l (location of the maximum shock velocity) somewhat larger than measurement. Neither of these solutions yield values of maximum shock velocity that exceed the predictions of references 10 and 20, which are nearly identical for helium. Thus, all prediction methods considered significantly underpredict the experimental maximum shock velocities for helium. Assumption of diaphragm opening times greater than $200 \mu\text{sec}$ in the characteristics solution and finite-difference solution will not alter the predicted maximum velocity. However, the location of maximum velocity will increase linearly with assumed opening time.

Pressure-time histories of the expanding helium driver are shown at two axial locations in figure 25. The measured pressure is higher at any given time than the pressure

predicted by conventional theory (instantaneous opening diaphragm) or by solutions which assume a 200- μ sec diaphragm opening time. In fact, increasing the assumed opening time decreases the predicted pressure at any instance of time and thereby results in even poorer agreement with experiment. These pressure histories also support the conclusion that the finite opening time solutions do not adequately predict the present experimental results.

Interface mixing. - White points out in reference 10 that a volume change occurs at the interface as a result of mixing of the driver and driven gases, if their specific heats are different. If the specific heat of the driven gas is greater than that of the driver gas, this volume change is positive and therefore accelerates the shock. Specifically, for a large temperature ratio across the interface, White derived the expression

$$1 + \frac{\Delta V}{V} = \frac{1}{2} \left(1 + \frac{c_{p,2}}{c_{p,3}} \right) \quad (5)$$

where ΔV is the change in volume and $c_{p,2}$ and $c_{p,3}$ are the specific heats at constant pressure of the driven gas and the driver gas, respectively. For air and CO₂ driven by helium, excitation of internal degrees of freedom increases the effective specific heat, and thus provides significant volume changes. However, for tests made with helium as the test gas, the helium flow behaves ideally, and although imperfect (inter-molecular force) effects are present in the helium driver, ΔV is essentially zero. The helium tests of figure 22(d) show that measured shock velocity exceeds predictions which take into account elevated driver temperature and formation from compression, even in the absence of appreciable volume change due to mixing. Although mixing may be a contributor to higher velocities than predicted for the present results, it is not a principal contributor.

Nonequilibrium flow. - For low quiescent test-gas pressures, corresponding to low values of density in the post-shock region, the relaxation of dissociation and ionization may be slow compared with the particle residence time behind the shock. This results in a lower density ratio across the shock wave ρ_2/ρ_1 (higher temperature in post-shock region) and thus a faster shock velocity for a given flow velocity behind the shock wave (conservation of mass considerations). The effect of nonequilibrium cannot be an important contributor to the difference observed in shock velocity between prediction and measurement because (1) shock velocities exceeding prediction are observed for values of p_1 sufficiently high to suppress an extensive departure from equilibrium flow, and (2) the helium results, in which chemistry and ionization are not factors, also display higher measured shock velocities than predicted.

Departures from one-dimensional flow. - In the previous theoretical analyses the shock-tube flow is assumed to be one-dimensional throughout. However, several factors,

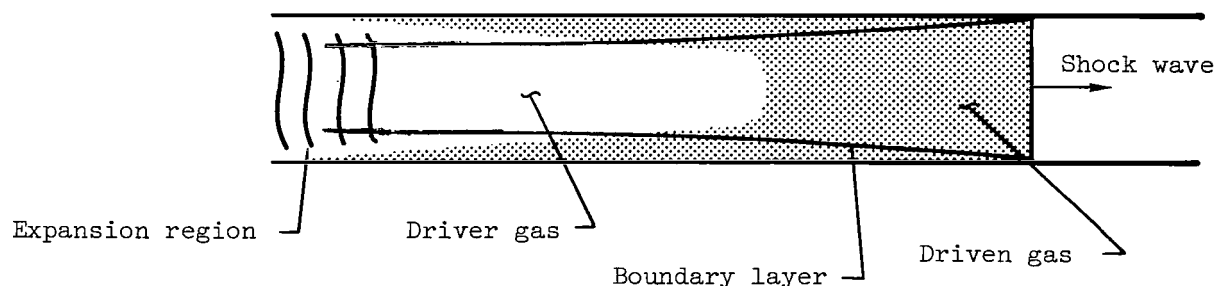
particularly the diaphragm opening and the unsteady wall boundary layer, may cause significant departures from one-dimensional flow. Analysis of these effects on the flow has received only limited attention in the literature.

When a scribed metal diaphragm first ruptures, the driver gas issues from the opened portion and expands as a free jet to fill the driven-section cross section. A number of curved compression waves propagate downstream and coalesce to form a curved shock wave. The profile of this shock wave becomes less curved as it proceeds down the driven section. Such a shock formation process is discussed and illustrated in reference 23. At the interface a mixing process is initiated by the jet-plume nature of the expanded driver gas. Near the diaphragm an oblique shock system is required to deflect the three-dimensional emerging jet to rectilinear flow. This shock system will exist until the diaphragm is fully open. In reference 24 the diaphragm opening process was assumed to be a circular aperture enlarging with time, and the resulting flow was treated two-dimensionally by a finite-difference technique. Both driver and driven gases were assumed to be ideal air, and diaphragm pressure ratios p_4/p_1 of 10, 100, and 1000 were considered. The results of this study were in good agreement with the shock strength predictions of reference 20 for pressure ratios of 10 and 100. At a pressure ratio of 1000, the two-dimensional shock strength prediction of reference 24 was slightly greater than the one-dimensional prediction of reference 20. Thus, the predictions of reference 24 demonstrate that the trend resulting from departure from one-dimensional flow is to increase the shock velocity for a given pressure ratio.

The wall boundary layer represents another departure from one-dimensional flow, and examination of the interface velocities has suggested the possibility that mixing of the driver and driven gases by the boundary layer may be important. The velocity of the interface was not measured accurately in the present experiments; however, for one group of tests, an attempt was made to determine the interface velocity from the photomultiplier traces. The test gas was air and the driver pressure was about 54 MN/m². Interface arrival was assumed to correspond to the rapid decay of the photomultiplier signal. The resultant determinations of shock-interface separation were in good agreement with the prediction method of reference 25.

Average velocities of the interface and the corresponding measured static pressures are shown in figure 26 for the group of five tests. Also shown in the figure is the predicted variation of pressure with velocity for an isentropic unsteady expansion of the helium driver, in which the initial state was assumed to be p_4 equal to 54 MN/m² and T_4 equal to 330 K. Comparison of the theory with experiment shows that velocity is significantly underpredicted for a given pressure. It appears that some mechanism is present which imparts additional energy to the expanding driver gas.

The unsteady wall boundary layer is one possible source for this additional energy. In the shocked gas region ahead of the interface, the boundary layer entrains a significant portion of the mass of gas passing through the shock wave (ref. 25). This shock-heated gas tends to "surround" the driver gas as illustrated in the sketch below. This boundary



layer in the driver-gas region may in many cases be thick compared with the tube radius and is likely to be turbulent. Extensive mixing between the cold (expanded) driver gas and the entrained driven gas, resulting in an appreciably warmer driver gas, may occur. As this warmed driver gas expands, it will display a different pressure-velocity relationship than that assumed for isentropic expansion of the pure driven gas.

The previous discussion is speculative and is not supported by calculation because of lack of an adequate flow model to represent the thick two-gas boundary layer. No applicable studies have been found in the literature. Since the various one-dimensional analyses considered have not provided a totally adequate explanation for the present data, it appears likely that phenomena such as those discussed may play a contributing role.

CONCLUDING REMARKS

Because the incident shock velocity in the intermediate section of an expansion tube is a basic input to conventional expansion-tube theory for predicting test-section flow quantities, it is measured for each test. This measured shock velocity must be known accurately, since small uncertainties in velocity result in large uncertainties in predicted test-section quantities. Existing methods for inferring shock velocity were studied by operating the Langley 6-inch expansion tube as a shock tube with air, argon, carbon dioxide, and helium as test gases. Unheated helium was employed as the driver gas, and most data were obtained at pressures of approximately 34 and 54 MN/m². A range of pressure ratio across the primary diaphragm was obtained by varying the quiescent test-gas pressure from 0.0276 to 34.5 kN/m².

Shock velocities were inferred from microwave interferometer measurements, response of pressure transducers positioned along the driven section (time-of-arrival

transducers), and measured tube-wall pressure. The microwave technique gives better definition of shock-wave characteristics (acceleration-deceleration trends) along the tube and is a viable method provided that microwave reflection occurs at the shock front. For the present range of conditions, the microwave proved to be rather limited in application. It is recommended that values obtained by the microwave method should always be verified by one of the other methods. Shock velocities inferred from time-of-arrival transducers and from measured wall pressures agree within the experimental accuracies. The time-of-arrival method avoids many of the shortcomings of the other two methods and is believed to be the most acceptable method of those examined. Measured shock velocities were observed to accelerate initially and then to decelerate with distance downstream from the diaphragm for all test gases. This trend was most pronounced for helium; argon, air, and carbon dioxide experienced successively less attenuation. The distance required for the shock velocity to reach a maximum value increased with increasing pressure ratio across the diaphragm for all test gases. At the higher pressure ratios, the shock velocity remained more nearly constant with distance after the initial acceleration for the present tube length of 29.0 m. For a given test gas and pressure ratio, minor differences in shock velocity were observed between single- and double-diaphragm modes of operation. The measured maximum shock velocity with helium as the test gas and a pressure ratio of approximately 10^3 was 1.08 to 1.11 times the velocity predicted from conventional shock-tube theory for all diaphragm materials tested; however, the distance for the shock velocity to reach a maximum value varied with diaphragm material.

Measured shock velocities exceeded real-gas predictions from conventional shock-tube theory and predictions from formation-from-compression theories for all test gases, with the exception of some argon results. Primary contributing factors to this discrepancy are believed to be (1) the effect of the helium driver temperature increasing upon pressurization of the driver section, (2) effects resulting from the finite opening time of the primary diaphragm, and (3) two-dimensional or nonplanar flow effects. Tests with helium as the test gas discounted interface mixing and flow chemistry as primary contributors to this difference between measured shock velocity and theory.

Langley Research Center
National Aeronautics and Space Administration
Hampton, Va. 23665
November 20, 1975

REFERENCES

1. Creel, Theodore R., Jr.: Experimental Performance of an Internal Resistance Heater for Langley 6-Inch Expansion Tube Driver. NASA TN D-7070, 1972.
2. Moore, John A.: Description and Initial Operating Performance of the Langley 6-Inch Expansion Tube Using Heated Helium Driver Gas. NASA TM X-3240, 1975.
3. Trimpi, Robert L.: A Preliminary Theoretical Study of the Expansion Tube, A New Device for Producing High-Enthalpy Short-Duration Hypersonic Gas Flows. NASA TR R-133, 1962.
4. Laney, Charles C., Jr.: Microwave Interferometry Technique for Obtaining Gas Interface Velocity Measurements in an Expansion Tube Facility. NASA TM X-72625, 1974.
5. Miller, Charles G., III: A Program for Calculating Expansion-Tube Flow Quantities for Real-Gas Mixtures and Comparison With Experimental Results. NASA TN D-6830, 1972.
6. Mulac, A. J.: Experimental and Theoretical Investigation of Shock-Tube Precursors. SUDAAR No. 358 (NASA Grant NGR 05-020-245), Stanford Univ., Sept. 1968. (Available as NASA CR-97190.)
7. Dobbins, Richard A.: Precursor Photoexcitation and Photoionization of Argon in Shock Tubes. AIAA J., vol. 8, no. 3, Mar. 1970, pp. 407-414.
8. Oettinger, Peter E.; and Bershader, Daniel: A Unified Treatment of the Relaxation Phenomenon in Radiating Argon Plasma Flows. AIAA J., vol. 5, no. 9, Sept. 1967, pp. 1625-1632.
9. Schneider, Klaus-Peter; and Park, Chul: Shock Tube Study of Ionization Rates of NaCl-Contaminated Argon. Phys. Fluids, vol. 18, no. 8, Aug. 1975, pp. 969-981.
10. White, Donald R.: Influence of Diaphragm Opening Time on Shock-Tube Flows. J. Fluid Mech., vol. 4, pt. 6, Nov. 1958, pp. 585-599.
11. Simpson, C. J. S. M.; Chandler, T. R. D.; and Bridgman, K. B.: Effect on Shock Trajectory of the Opening Time of Diaphragms in a Shock Tube. Phys. Fluids, vol. 10, no. 9, Sept. 1967, pp. 1894-1896.
12. Curzon, F. L.; and Phillips, M. G. R.: Low Attenuation Shock Tube: Driving Mechanism and Diaphragm Characteristics. Canadian J. Phys., vol. 49, no. 15, Aug. 1, 1971, pp. 1982-1993.
13. Jones, Jim J.: Experimental Investigation of Attenuation of Strong Shock Waves in a Shock Tube With Hydrogen and Helium as Driver Gases. NACA TN 4072, 1957.

14. Stalker, R. J.; Healey, G. J.; Kerr, D. W. M.; and Bennett, J. G.: A High-Performance Shock Tube With Air Driver. AIAA J., vol. 9, no. 8, Aug. 1971, pp. 1646-1647.
15. Yamaki, Yoshio; and Rooker, James R.: Experimental Investigation of Circular, Flat, Grooved and Plain Steel Diaphragms Bursting Into a 30.5-Centimeter-Square Section. NASA TM X-2549, 1972.
16. Nagamatsu, H. T.; Geiger, R. E.; and Sheer, R. E., Jr.: Hypersonic Shock Tunnel. ARS J., vol. 29, no. 5, May 1959, pp. 332-340.
17. Whitfield, Jack D.; Norfleet, Glenn D.; and Wolny, W.: Status of Research on a High Performance Shock Tunnel. AEDC-TR-65-272, U.S. Air Force, May 1966. (Available from DDC as AD 482 454.)
18. Gaydon, A. G.; and Hurle, I. R.: The Shock Tube in High-Temperature Chemical Physics. Reinhold Pub. Corp., 1963.
19. Russo, Anthony L.; and Hertzberg, A.: Modifications of the Basic Shock Tube To Improve Its Performance. AFOSR TN 58-716, AD 162 251, U.S. Air Force, Aug. 1958.
20. Ikui, Takefumi; Matsuo, Kazuyasu; and Nagai, Minoru: Investigations of the Aerodynamic Characteristics of the Shock Tubes (Part 2, On the Formation of Shock Waves). Bull. JSME, vol. 12, no. 52, Aug. 1969, pp. 783-792.
21. Alpher, R. A.; and White, D. R.: Flow in Shock Tubes With Area Change at the Diaphragm Section. J. Fluid Mech., vol. 3, pt. 5, Feb. 1958, pp. 457-470.
22. Weilmuenster, Kenneth James: One-Dimensional Finite Difference Solutions of the Navier-Stokes Equations With Applications to the Flow Phenomena in Expansion Tubes and Expansion Tunnels. M.S. Thesis, North Carolina State Univ. at Raleigh, 1974.
23. Henshall, B. D.: On Some Aspects of the Use of Shock Tubes in Aerodynamic Research. R. & M. No. 3044, British A.R.C., 1957.
24. Satofuka, Nobuyuki: A Numerical Study of Shock Formation in Cylindrical and Two-Dimensional Shock Tubes. ISAS Rep. No. 451, Univ. of Tokyo, 1970.
25. Mirels, Harold: Test Time in Low-Pressure Shock Tubes. Phys. Fluids, vol. 6, no. 9, Sept. 1963, pp. 1201-1214.

**TABLE I.- LOCATION OF TRANSDUCERS USED TO GENERATE
TIME-OF-ARRIVAL DATA FOR BOTH SERIES OF TESTS**

First series ^a			Second series ^b			
Station	x, m	Oscilloscope	Station	x, m	Oscilloscope	Counter-timer
7	2.297	✓	7	2.297	✓	✓
8	3.507	✓	8	3.493	✓	✓
10	4.118	✓	9	3.796	✓	✓
11	4.248	✓	10	4.101	✓	✓
12	4.412	✓	11	4.231		✓
13	4.575	✓	13	4.561	✓	✓
14	6.943	✓	14	5.377	✓	✓
15	8.065	✓	15	6.250	✓	✓
17	9.358	✓	16	6.927	✓	✓
19	10.780	✓	17	8.042	✓	✓
20	13.045	✓	18	10.163	✓	✓
21	15.249	✓	20	11.453	✓	✓
23	19.737	✓	21	11.640	✓	
24	21.612	✓	22	11.801		✓
			23	12.871	✓	✓
			24	15.159	✓	✓
			25	17.446	✓	✓
			26	19.729	✓	✓
			27	22.672	✓	✓
			28	25.549	✓	✓
			29	27.305	✓	✓

^a21.6-m-long driven section.

^b29.0-m-long driven section.

TABLE II. - CALCULATED THERMOCHEMICAL-EQUILIBRIUM PROPERTIES BEHIND INCIDENT
SHOCK FOR TESTS WITH DOUBLE DIAPHRAGM AND DRIVER PRESSURE OF
APPROXIMATELY 33 MN/m² FOR VARIOUS TEST GASES

(a) Argon

Run	T ₁ , K	p ₁ , kN/m ²	U _{s,max} , km/sec	At U _{s,max}			U _{s,final} , km/sec	At U _{s,final}		
				p ₂ , kN/m ²	T ₂ , K	N _e , electrons/cm ³		p ₂ , kN/m ²	T ₂ , K	N _e , electrons/cm ³
571	297.0	34.5	2.088	1820	4 186	1.62×10^{11}	1.807	1360	3201	1.51×10^8
570	297.6	6.90	2.743	627	7 030	7.47×10^{14}	2.271	429	4906	2.02×10^{12}
569	297.0	3.45	3.094	403	8 720	7.82×10^{15}	2.475	256	5777	2.70×10^{13}
566	297.0	.690	3.523	109	9 986	1.57×10^{16}	2.987	75.1	8135	1.56×10^{15}
567	297.0	.345	3.688	61.1	10 160	1.36×10^{16}	3.261	45.9	9068	3.96×10^{15}
593	298.2	.0690	3.947	14.4	10 030	5.70×10^{15}	3.758	12.9	9727	4.10×10^{15}
594	297.0	.0356	4.069	8.06	9 939	3.87×10^{15}	3.978	7.66	9817	3.38×10^{15}

(b) Air

Run	T ₁ , K	p ₁ , kN/m ²	U _{s,max} , km/sec	At U _{s,max}			U _{s,final} , km/sec	At U _{s,final}		
				p ₂ , kN/m ²	T ₂ , K	N _e , electrons/cm ³		p ₂ , kN/m ²	T ₂ , K	N _e , electrons/cm ³
561	297.0	34.5	2.057	1470	2060	2.99×10^7	1.905	1250	1833	1.05×10^6
559	297.2	6.90	2.606	479	2883	6.73×10^{10}	2.332	380	2480	2.17×10^9
557	297.8	3.45	2.911	302	3227	4.63×10^{11}	2.576	233	2819	2.95×10^{10}
553	298.7	.690	3.414	84.5	3543	1.07×10^{12}	3.100	69.1	3262	2.52×10^{11}
554	297.6	.345	3.551	46.1	3573	8.36×10^{11}	3.283	39.2	3339	2.70×10^{11}
556	298.2	.0690	4.100	12.4	4111	1.94×10^{12}	3.932	11.4	3807	7.47×10^{11}

Table II. - Concluded

(c) CO₂

Run	T ₁ , K	p ₁ , kN/m ²	U _{S,max} , km/sec	At U _{S,max}			U _{S,final} , km/sec	At U _{S,final}		
				p ₂ , kN/m ²	T ₂ , K	N _e , electrons/cm ³		p ₂ , kN/m ²	T ₂ , K	N _e , electrons/cm ³
580	297.6	6.90	2.301	598	2285	6.69×10^5	2.149	519	2117	2.96×10^4
578	297.6	3.45	2.530	364	2472	7.91×10^6	2.347	312	2308	7.66×10^5
573	298.2	.690	3.155	115	2778	1.72×10^8	2.819	91.0	2578	1.79×10^7
575	297.6	.345	3.338	64.6	2814	2.06×10^8	3.048	53.6	2658	3.68×10^7
576	297.0	.0690	3.804	16.9	2872	2.16×10^8	3.642	15.5	2799	9.75×10^7
577	297.0	.0345	4.084	9.78	2919	2.25×10^8	3.962	9.20	2865	1.37×10^8

(d) Helium

Run	T ₁ , K	p ₁ , kN/m ²	U _{S,max} , km/sec	At U _{S,max}			U _{S,final} , km/sec	At U _{S,final}		
				p ₂ , kN/m ²	T ₂ , K	N _e , electrons/cm ³		p ₂ , kN/m ²	T ₂ , K	N _e , electrons/cm ³
586	297.0	34.5	3.490	502	1355	1.56×10^{-14}	2.865	336	994	3.22×10^{-14}
585	297.0	6.90	3.962	130	1673	1.29×10^{-14}	3.307	90.0	1242	5.00×10^{-15}
582	297.6	3.45	4.206	73.2	1854	5.67×10^{-14}	3.597	53.3	1424	3.67×10^{-15}
583	297.0	.690	4.511	16.9	2094	1.48×10^{-10}	4.298	15.3	1924	3.89×10^{-13}
584	297.6	.345	4.511	8.43	2095	1.06×10^{-10}	4.420	8.09	2021	9.12×10^{-12}

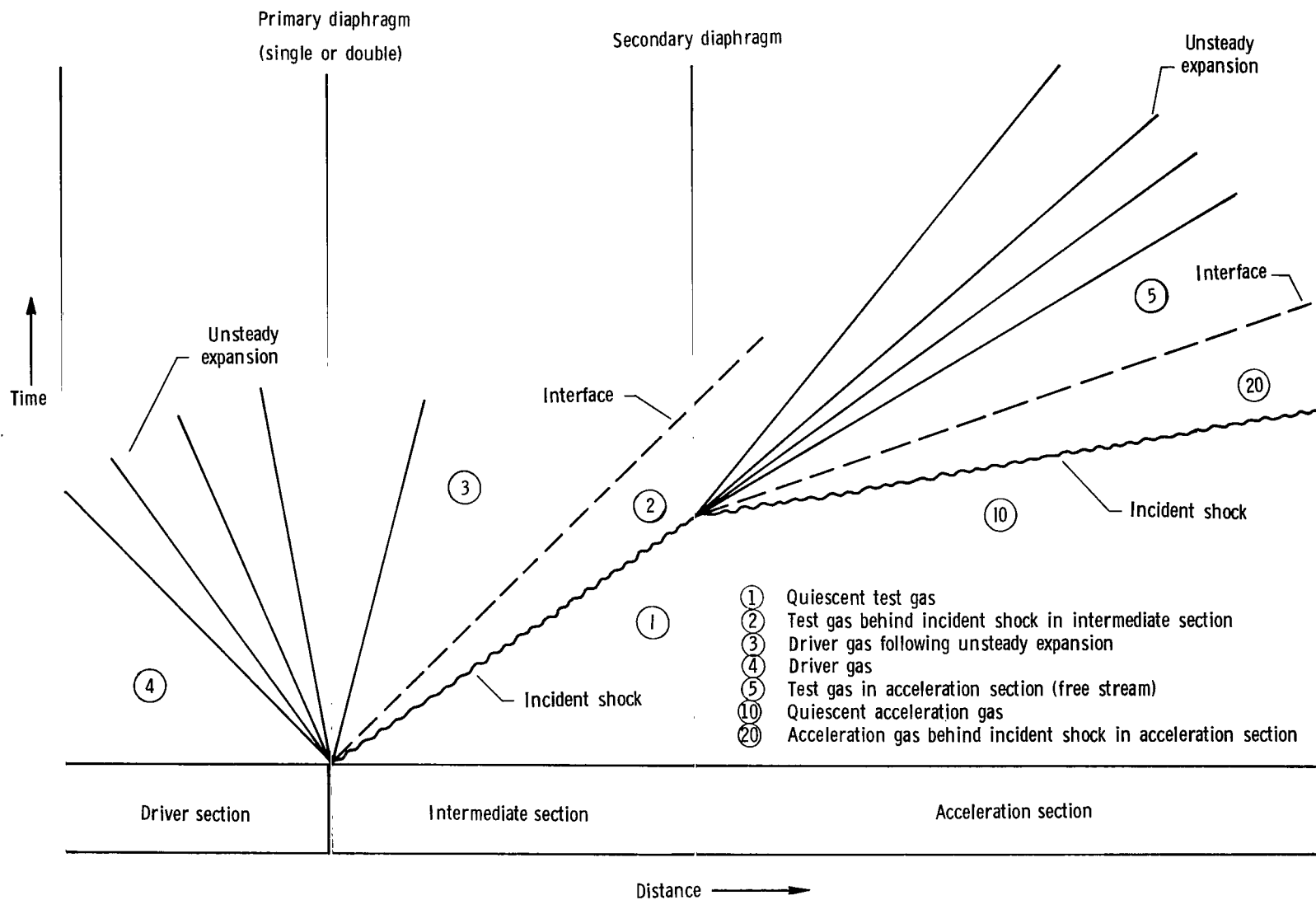


Figure 1.- Schematic diagram of expansion-tube flow sequence.

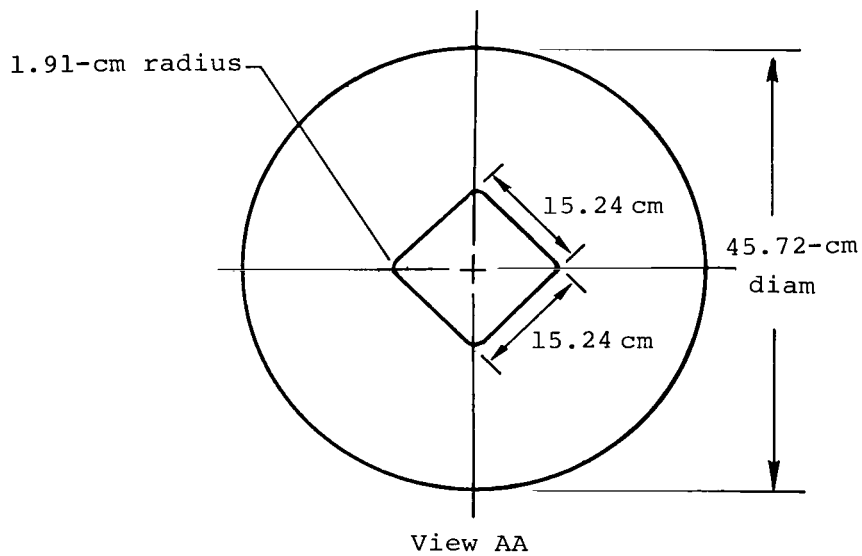
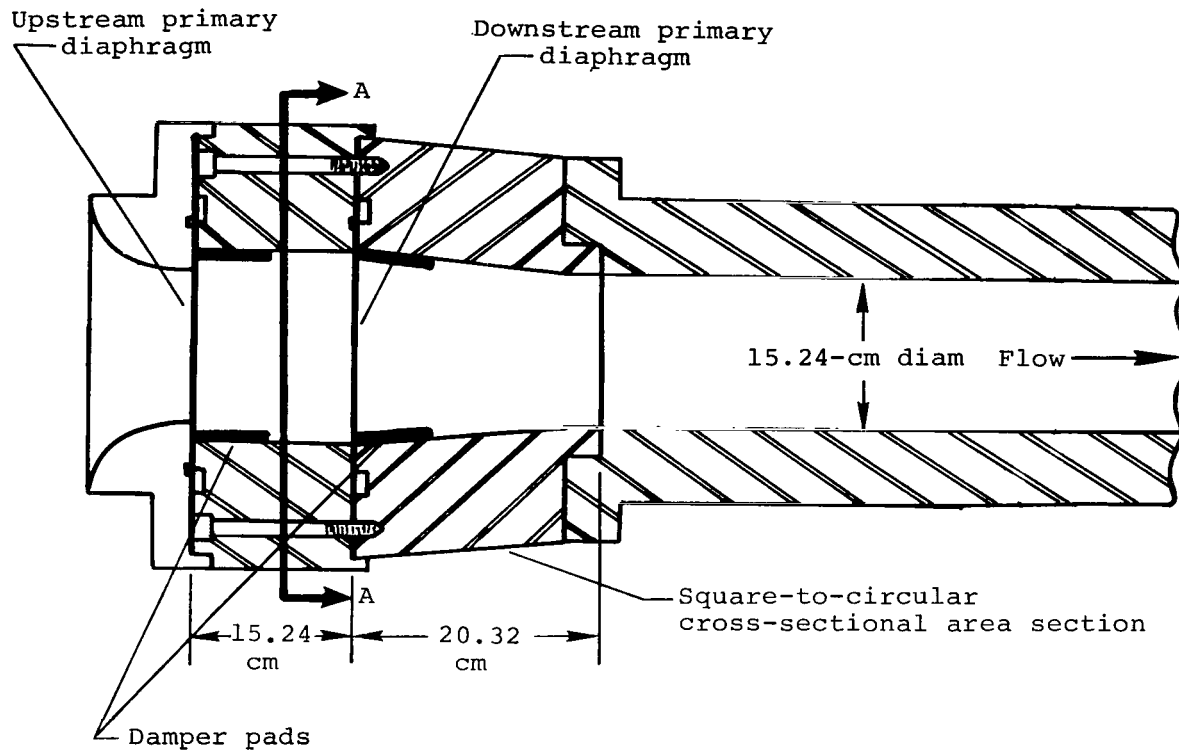


Figure 2.- Sketch of double-diaphragm section and intermediate section.

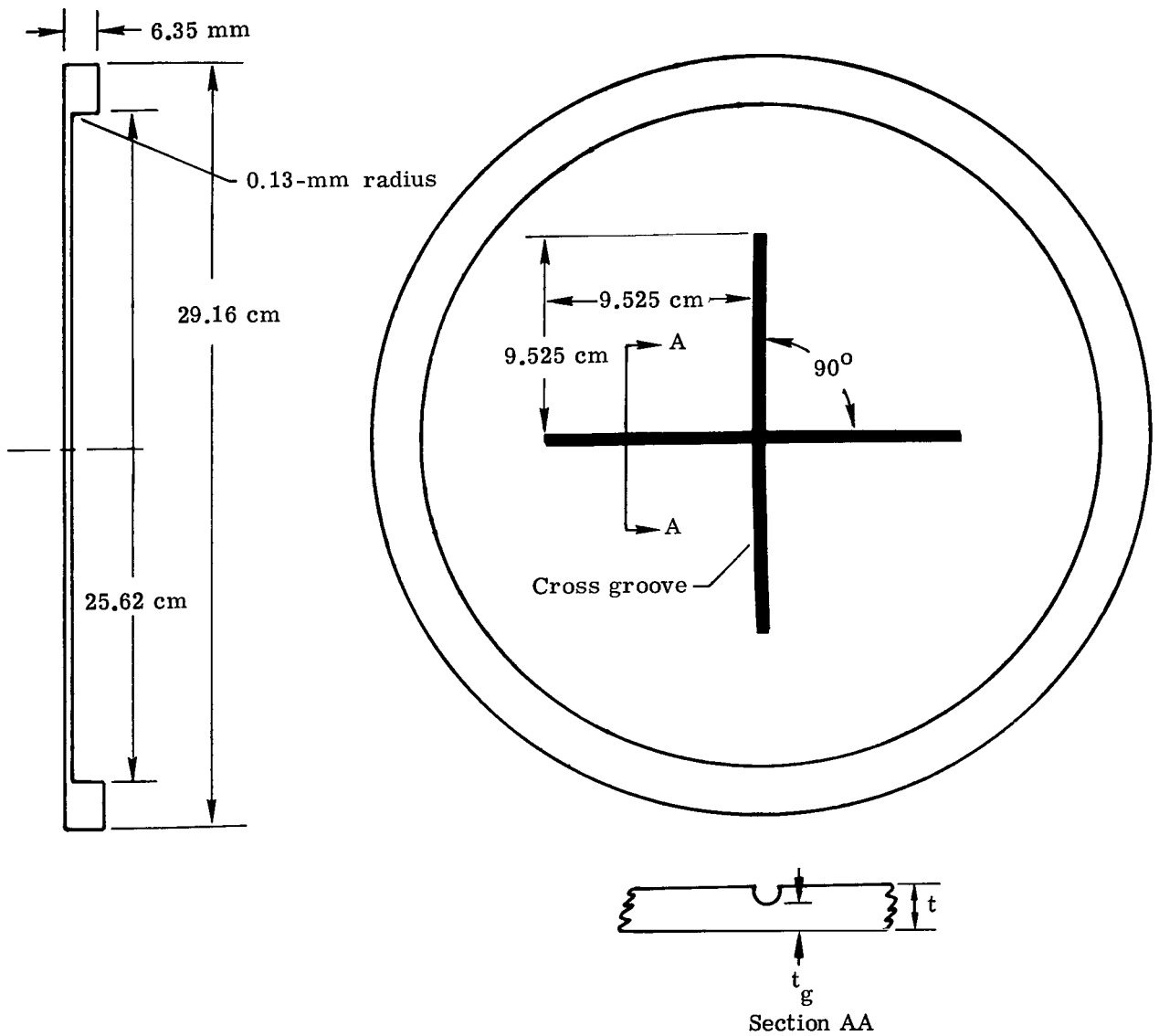
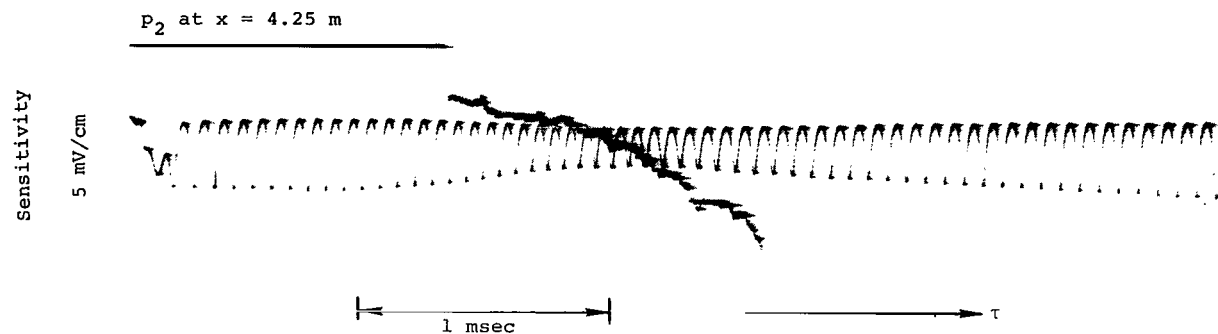
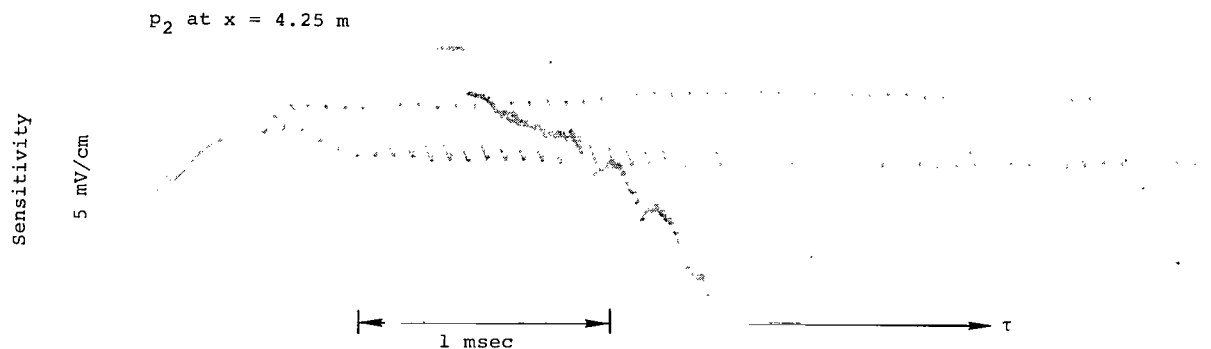


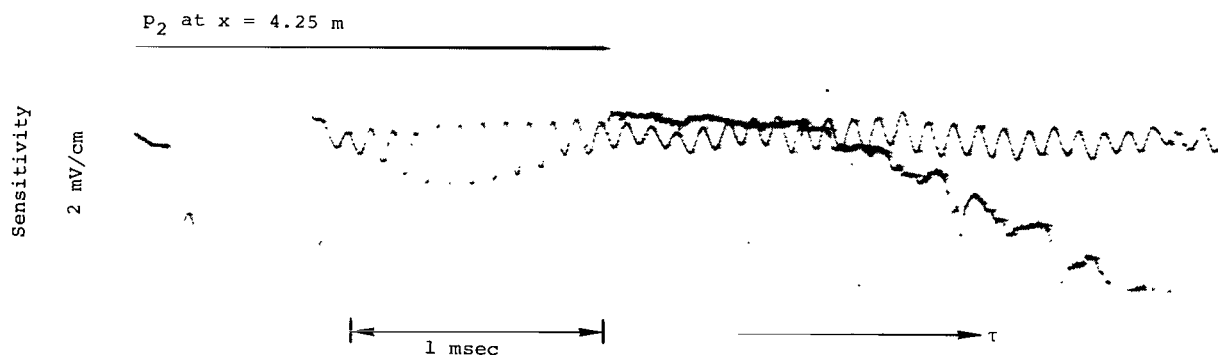
Figure 3. - Diaphragm geometry for metal diaphragms.



(a) Argon. Single diaphragm; $p_1 = 1.38 \text{ kN/m}^2$.



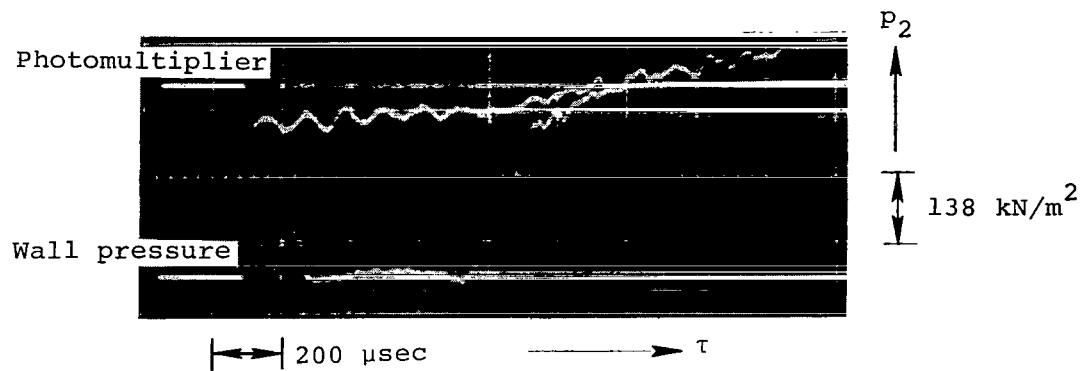
(b) Air. Single diaphragm; $p_1 = 0.690 \text{ kN/m}^2$.



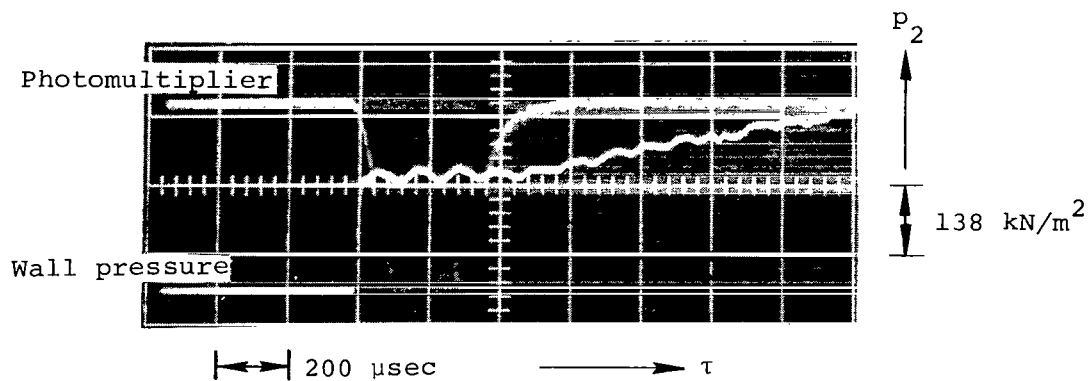
(c) CO_2 . Double diaphragm; $p_1 = 3.45 \text{ kN/m}^2$.

L-75-249

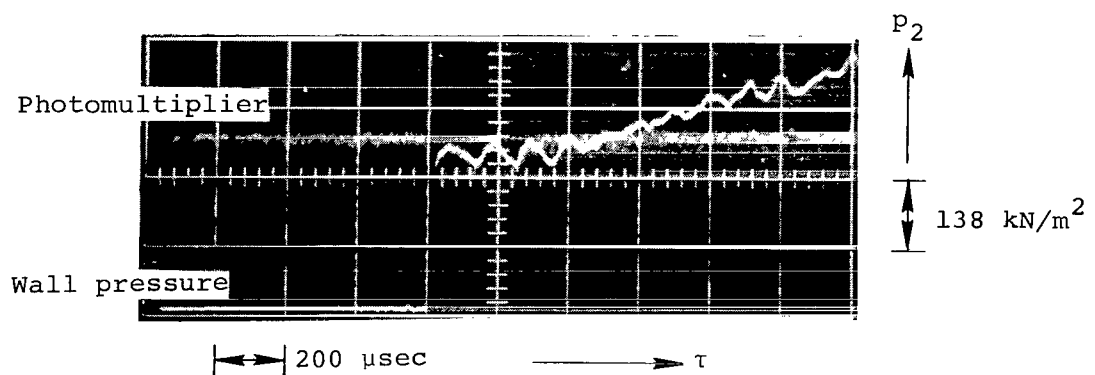
Figure 4.- Sample microwave traces for several test gases.



(a) Argon.



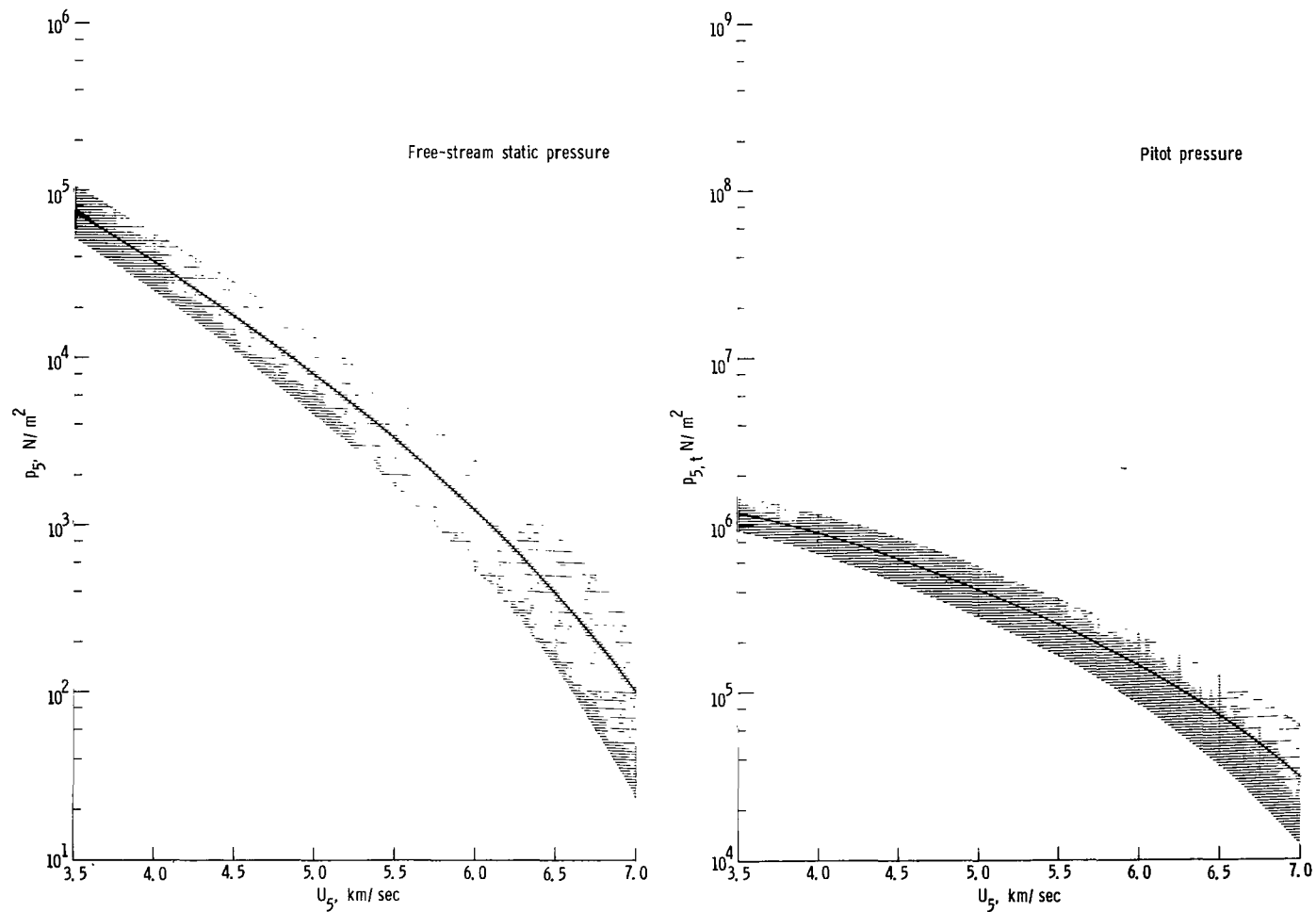
(b) Air.



(c) CO_2 .

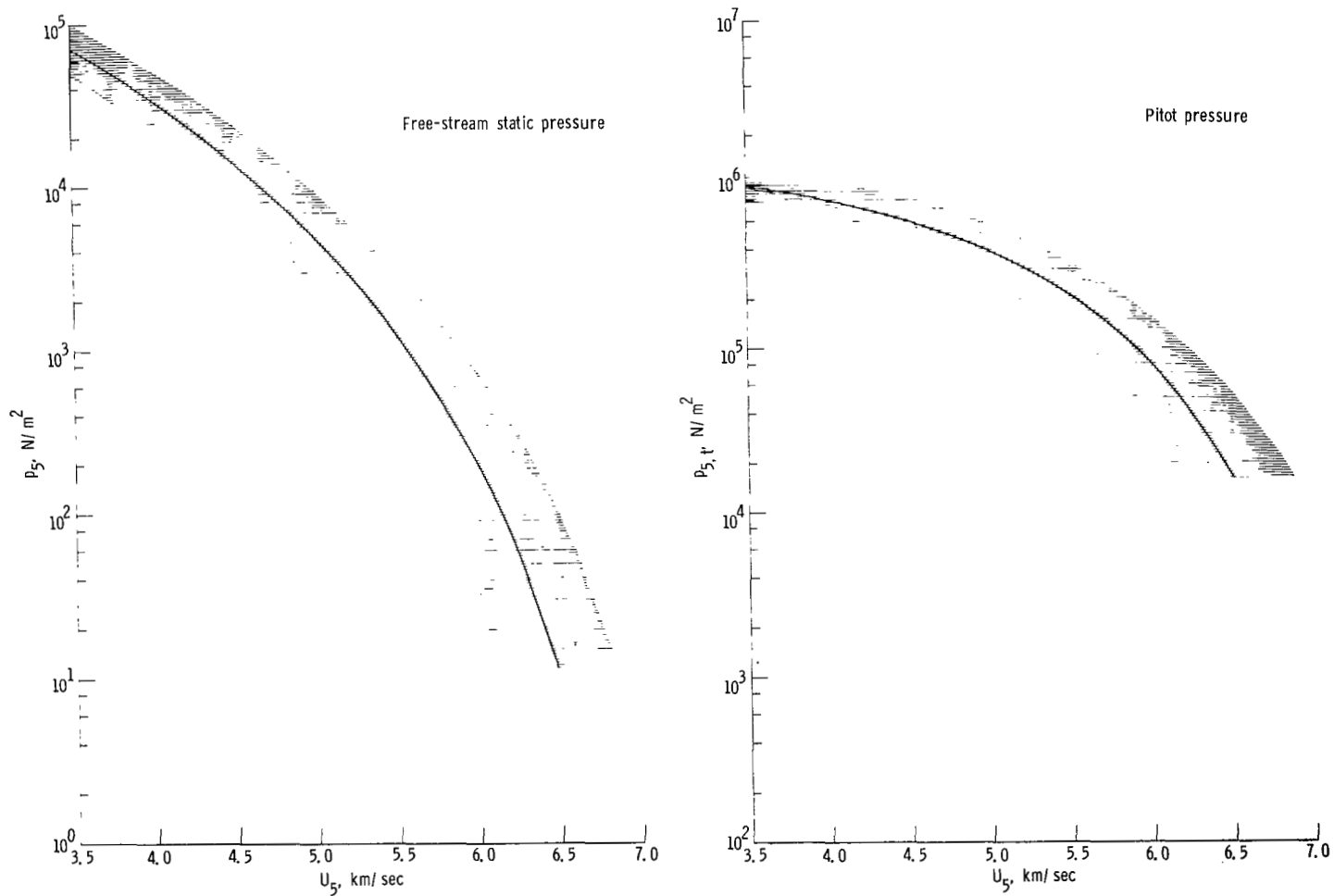
L-75-250

Figure 5.- Sample oscilloscope traces of wall static pressure in driven section for several test gases. $p_1 = 3.45 \text{ kN/m}^2$; $x = 19.75 \text{ m}$.



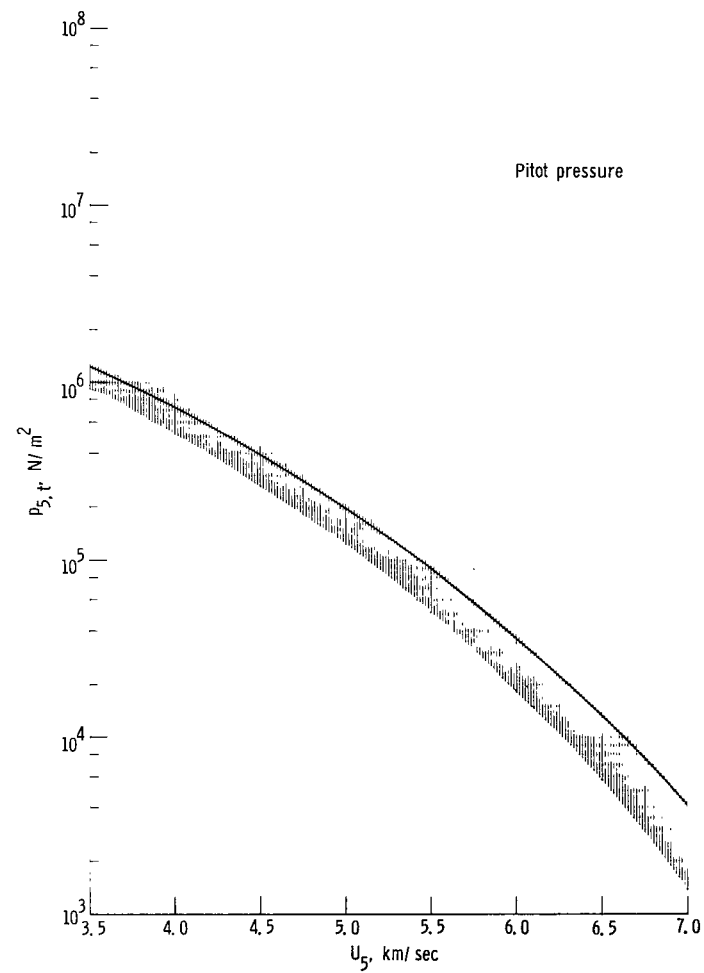
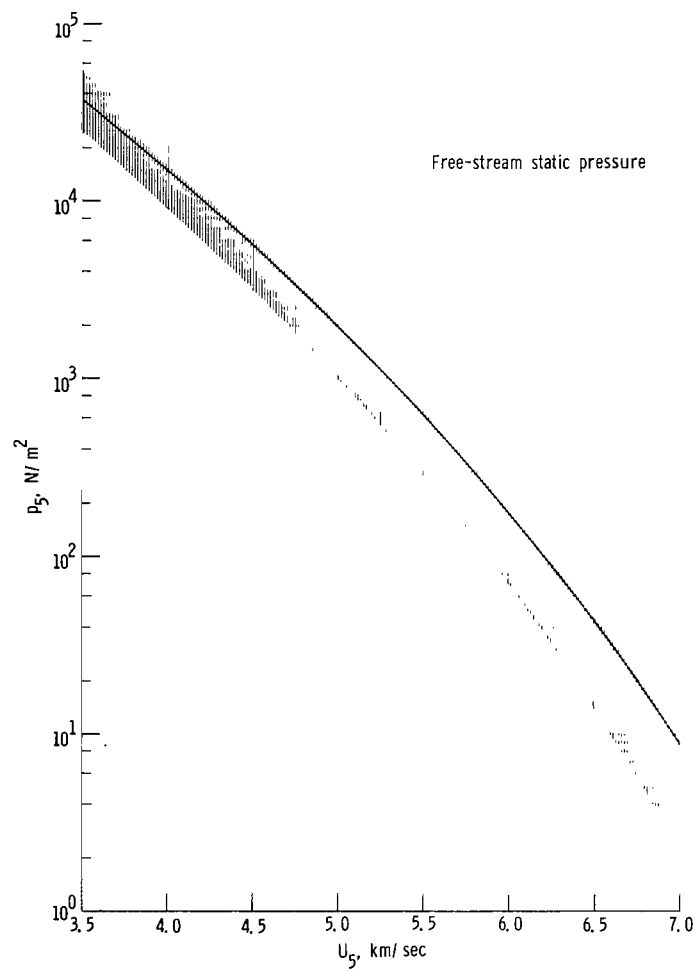
(a) Air. $U_s = 2.8 \text{ km/sec}$.

Figure 6.- Uncertainty in free-stream static pressure and pitot pressure due to corresponding uncertainty in shock velocity in intermediate section of expansion tube for several test gases. $p_1 = 3.45 \text{ kN/m}^2$; $T_1 = 300 \text{ K}$. Solid line was computed with program of reference 5 and shaded region denotes uncertainty corresponding to 5 percent uncertainty in U_s .



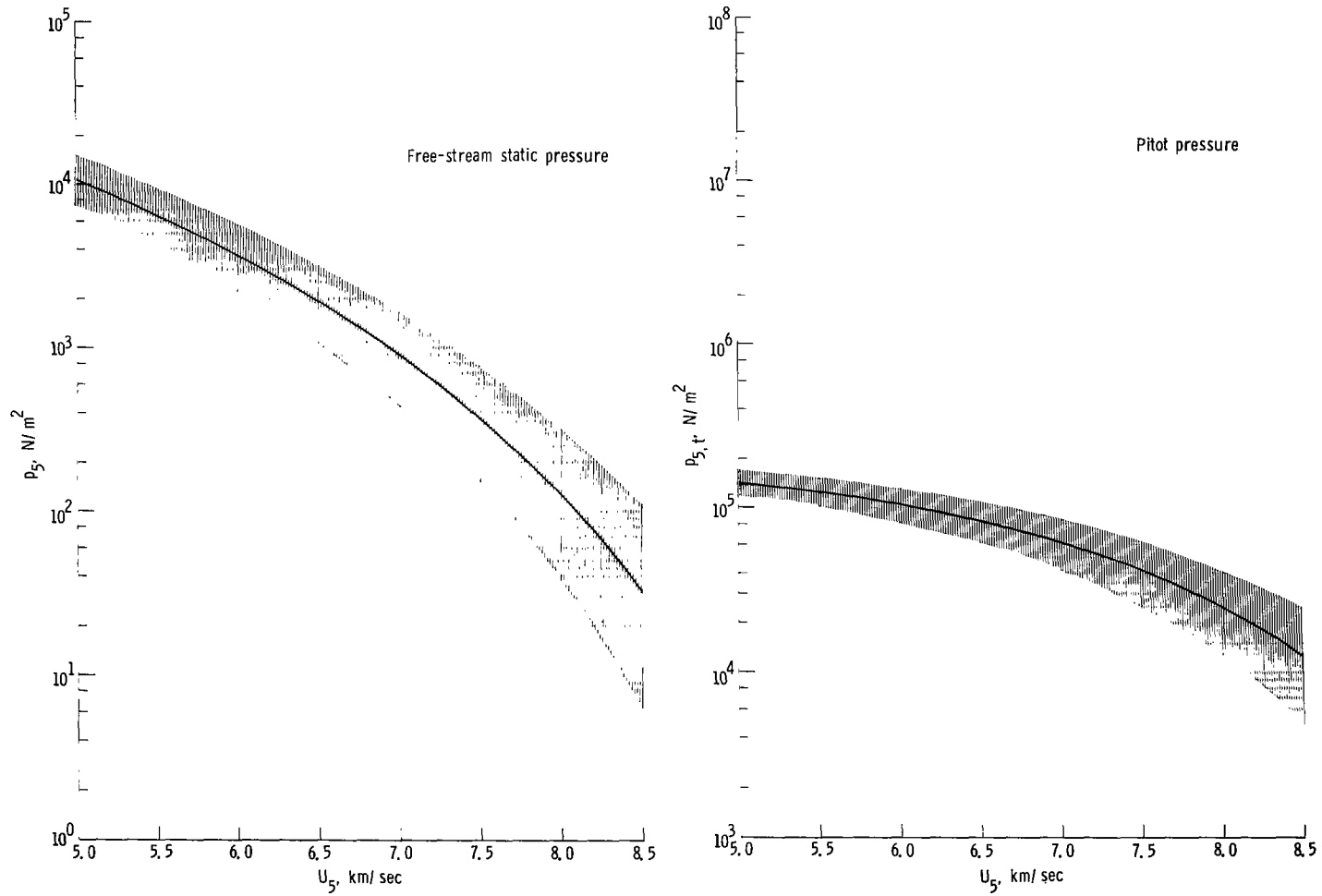
(b) Argon. $U_s = 2.9$ km/sec.

Figure 6.- Continued.



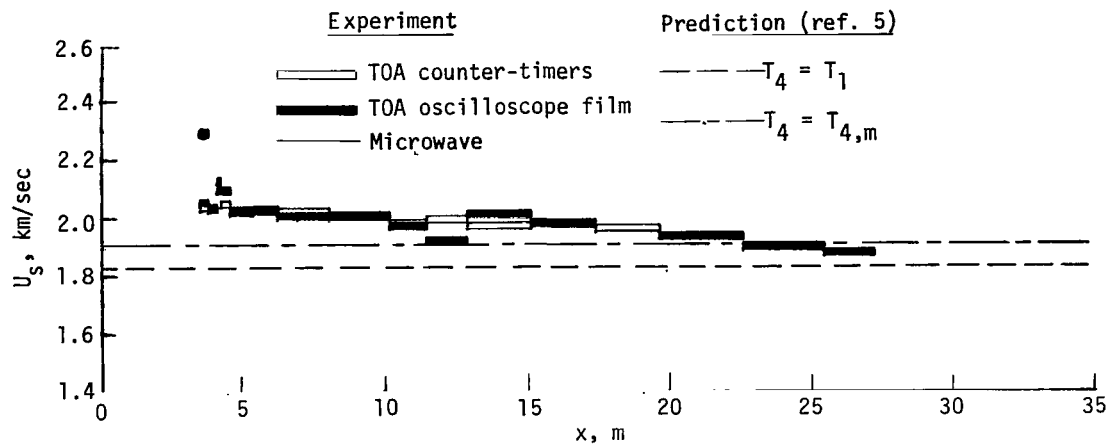
(c) CO_2 . $U_s = 2.4 \text{ km/sec}$.

Figure 6.- Continued.

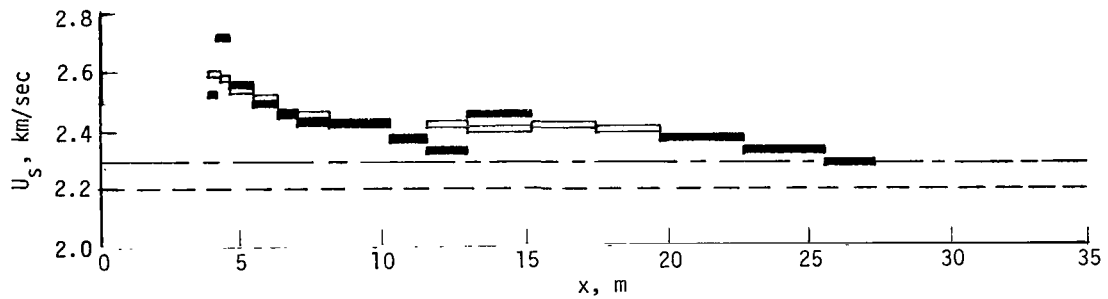


(d) Helium. $U_s = 4.0$ km/sec.

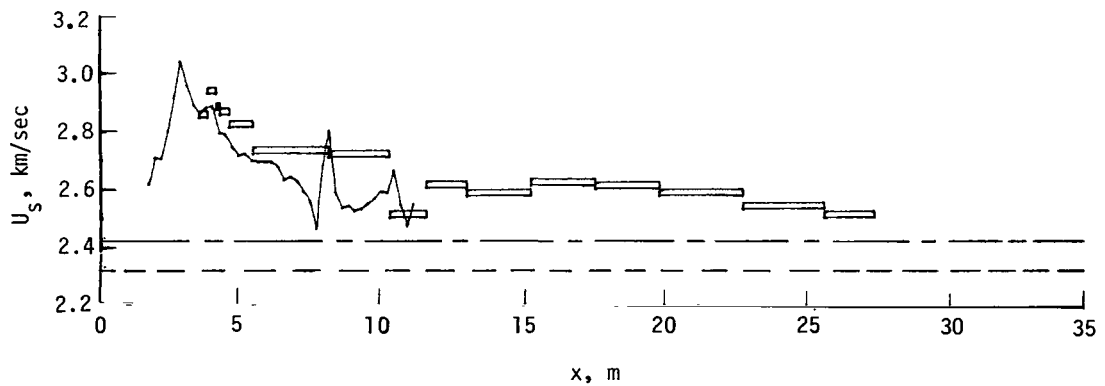
Figure 6.- Concluded.



(a) $p_1 = 34.5 \text{ kN/m}^2$.

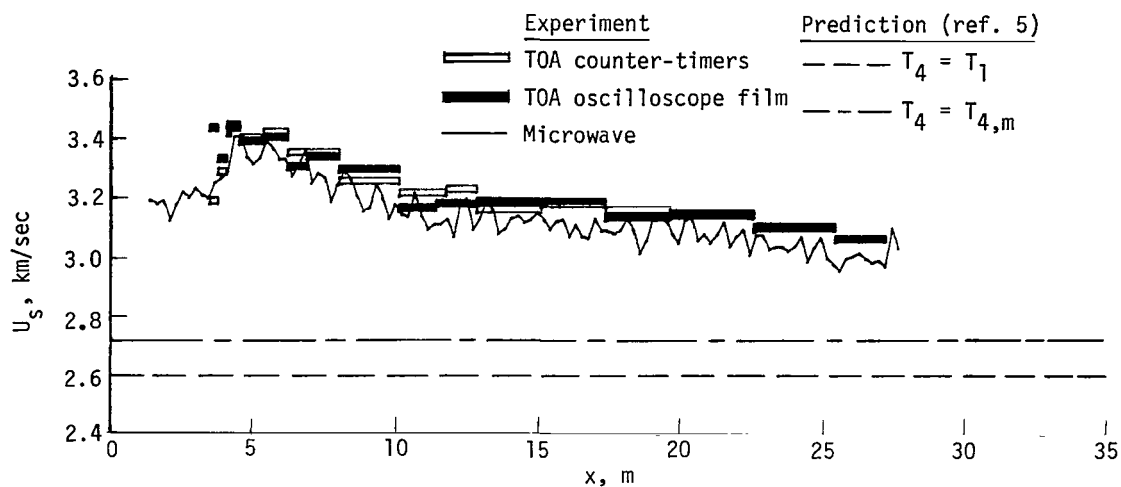


(b) $p_1 = 6.9 \text{ kN/m}^2$.

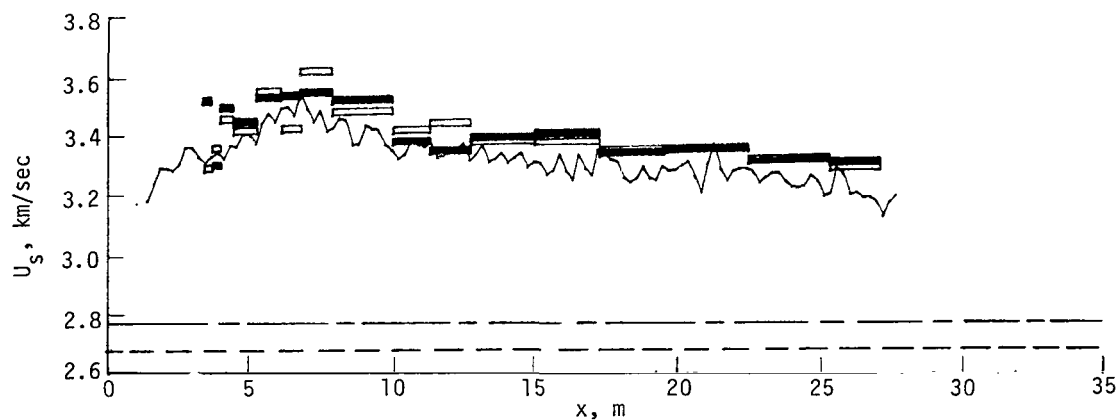


(c) $p_1 = 3.45 \text{ kN/m}^2$.

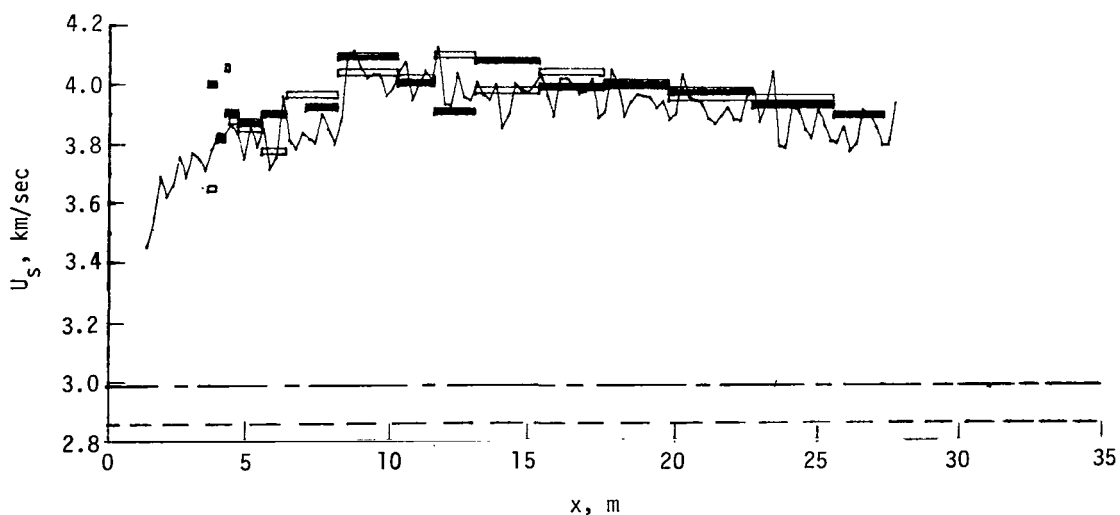
Figure 7.- Incident shock velocity as a function of distance downstream of primary diaphragm for air.



(d) $p_1 = 0.690 \text{ kN/m}^2$.

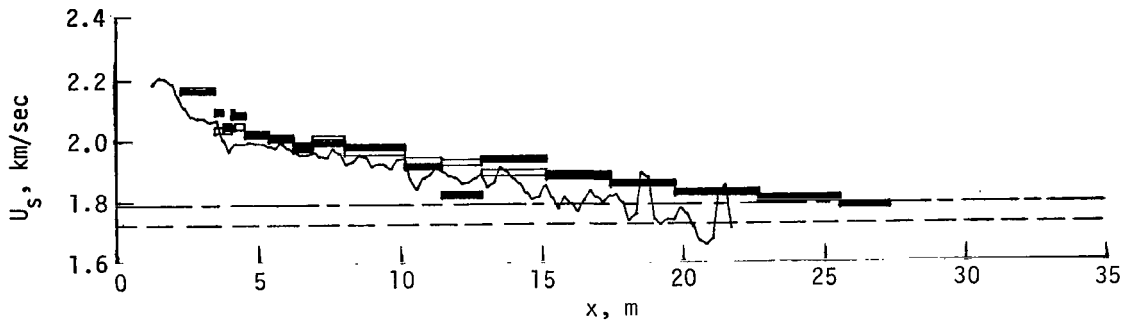


(e) $p_1 = 0.345 \text{ kN/m}^2$.

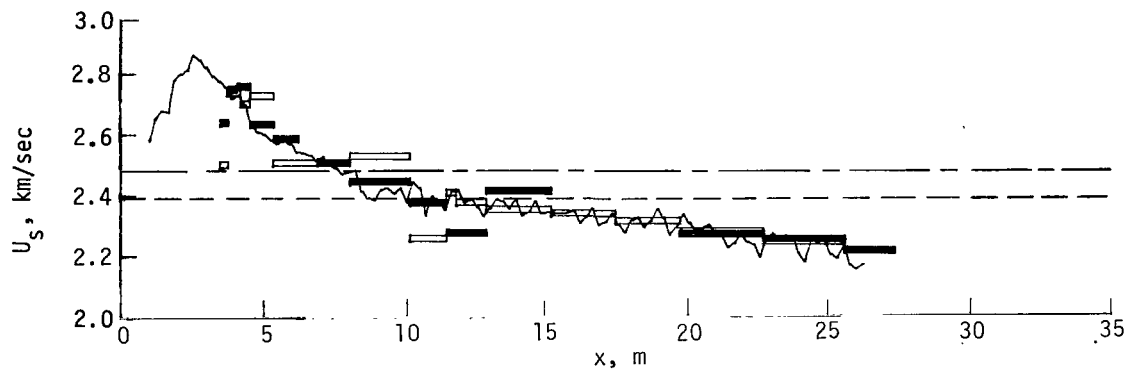


(f) $p_1 = 0.069 \text{ kN/m}^2$.

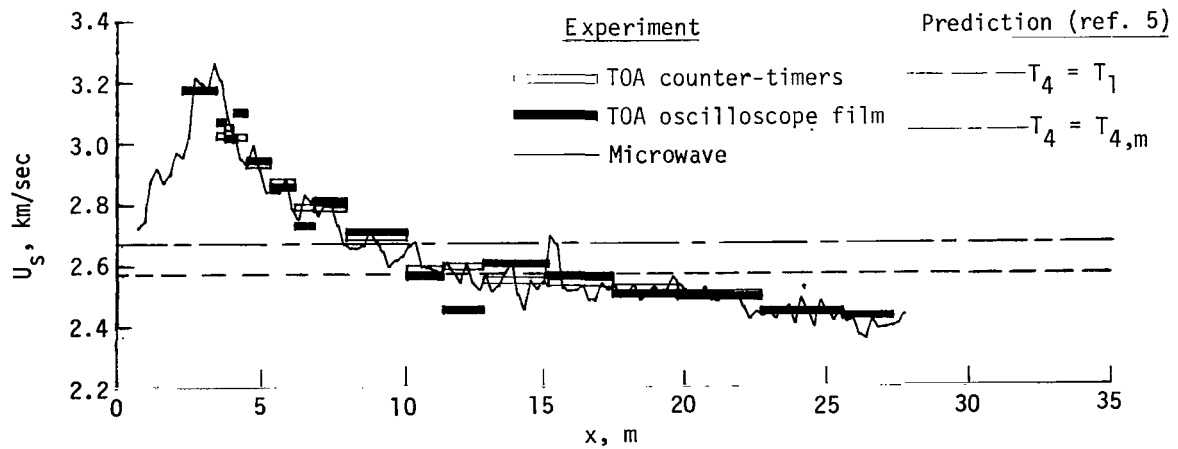
Figure 7.- Concluded.



(a) $p_1 = 34.5 \text{ kN/m}^2$.

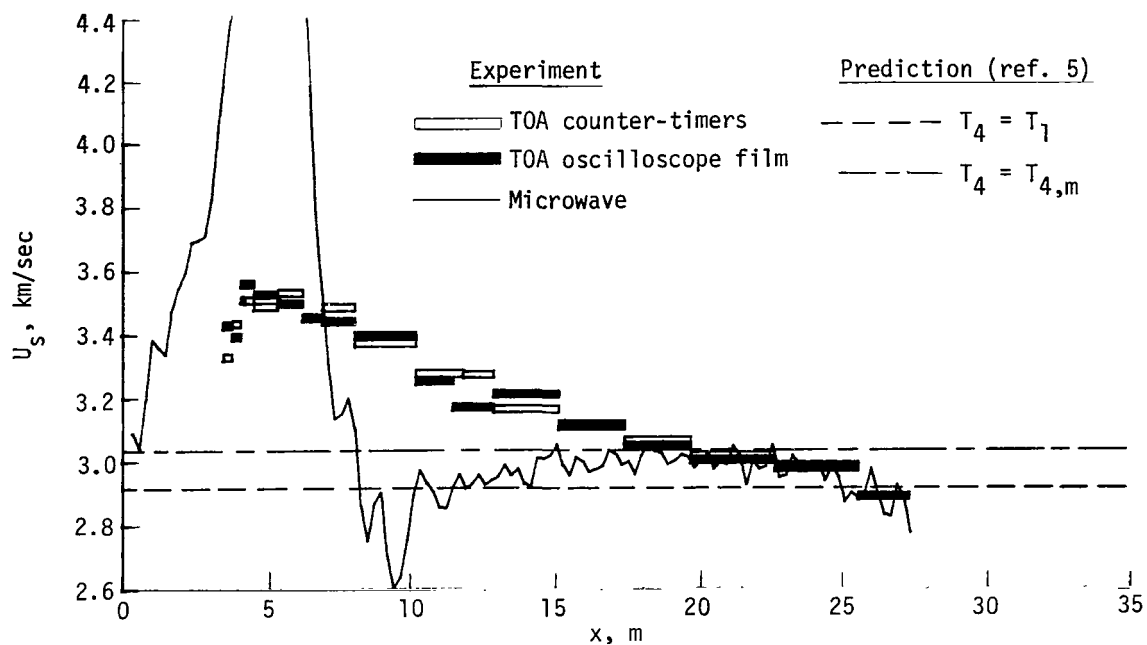


(b) $p_1 = 6.9 \text{ kN/m}^2$.

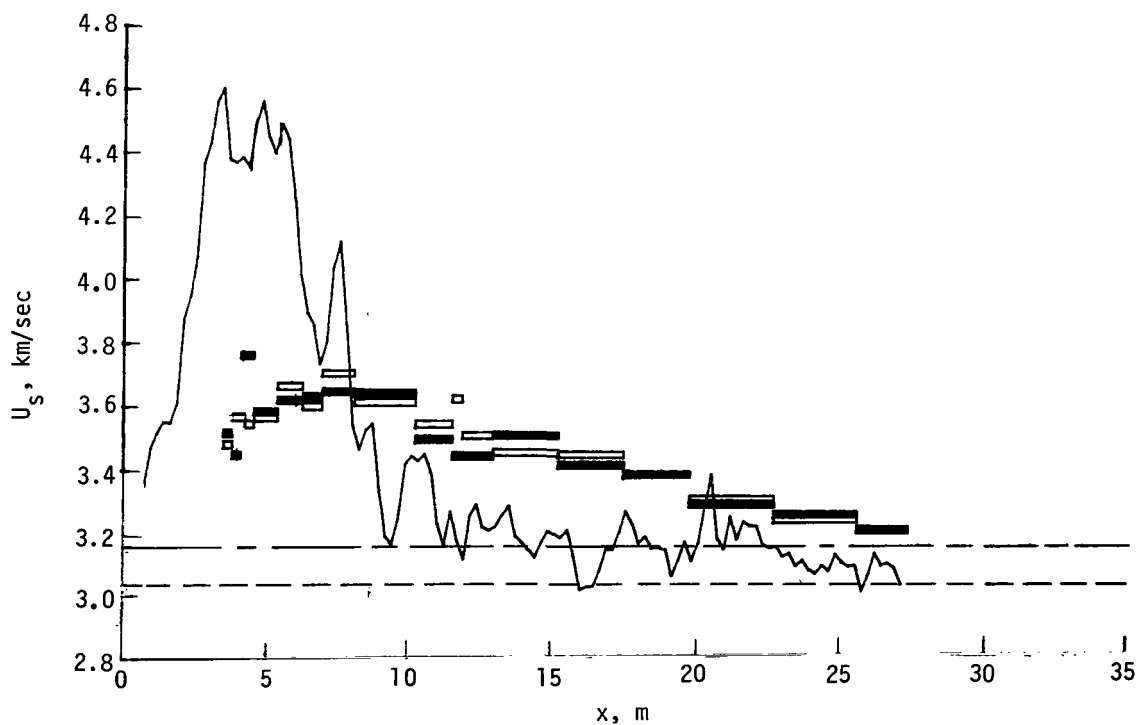


(c) $p_1 = 3.45 \text{ kN/m}^2$.

Figure 8. - Incident shock velocity as a function of distance downstream of primary diaphragm for argon.

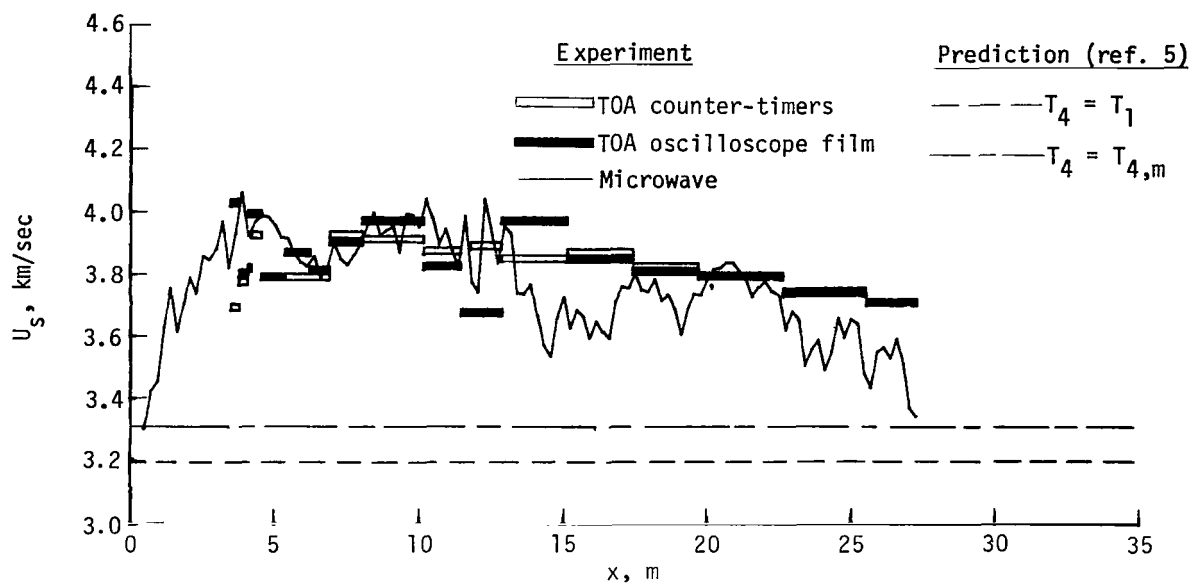


(d) $p_1 = 0.690 \text{ kN/m}^2$.

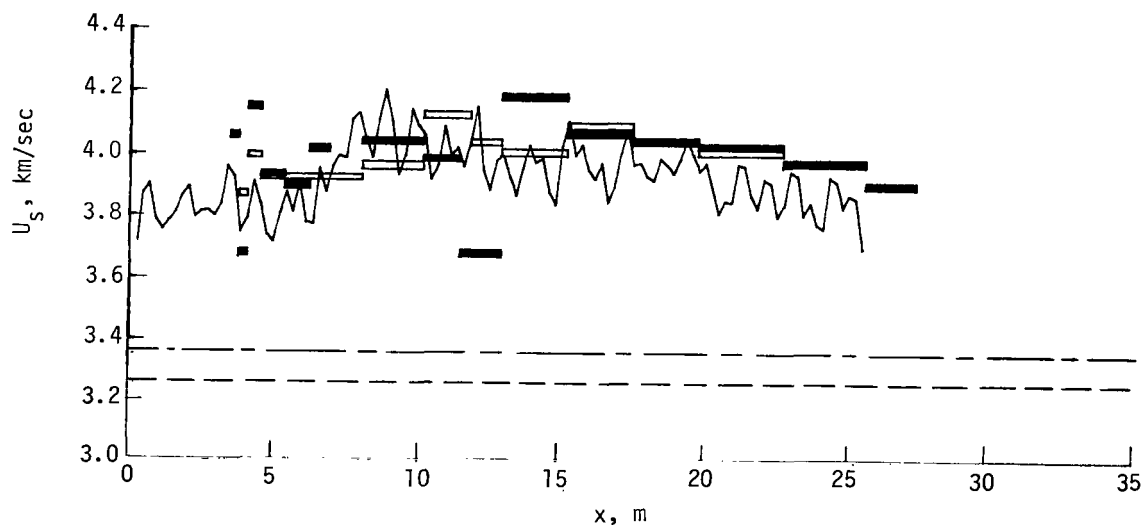


(e) $p_1 = 0.345 \text{ kN/m}^2$.

Figure 8.- Continued.

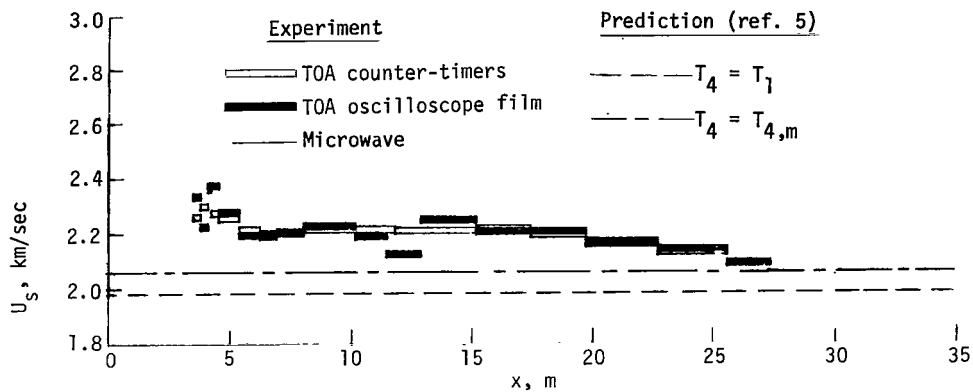


(f) $p_1 = 0.069 \text{ kN/m}^2$.

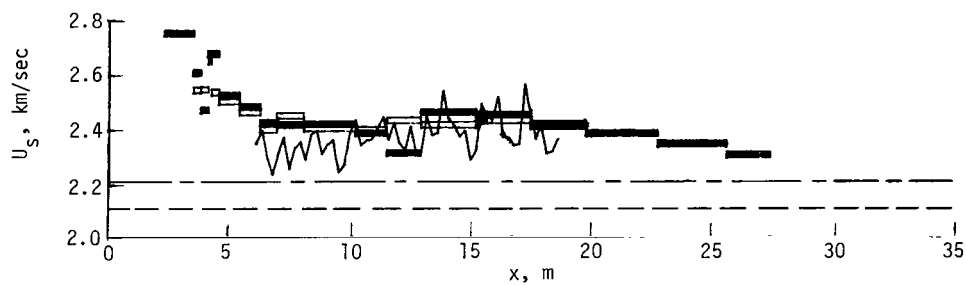


(g) $p_1 = 0.0345 \text{ kN/m}^2$.

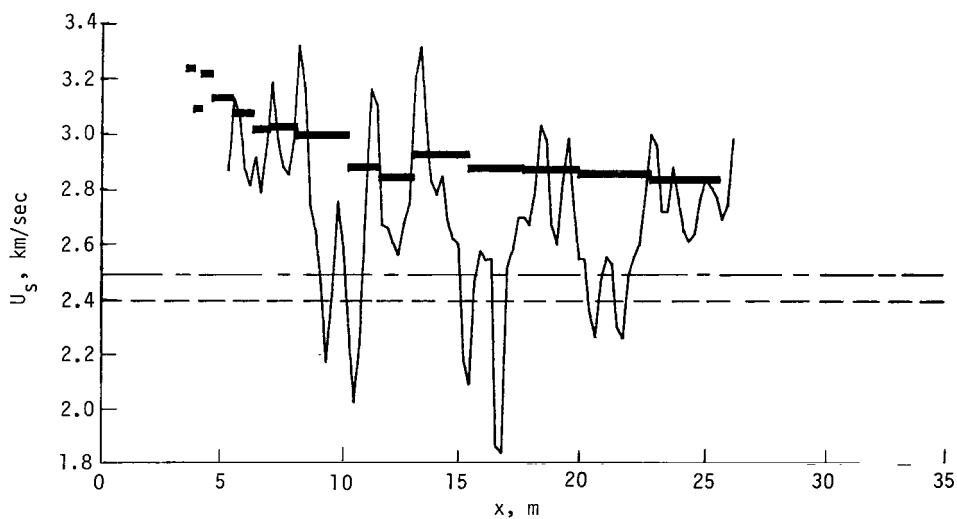
Figure 8.- Concluded.



(a) $p_1 = 6.9 \text{ kN/m}^2$.



(b) $p_1 = 3.45 \text{ kN/m}^2$.



(c) $p_1 = 0.690 \text{ kN/m}^2$.

Figure 9.- Incident shock velocity as a function of distance downstream of primary diaphragm for CO_2 .

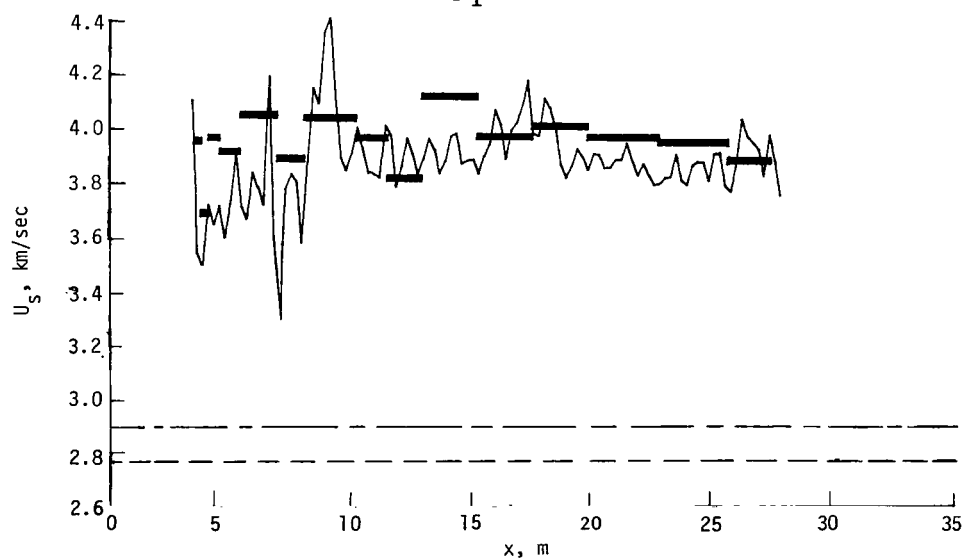
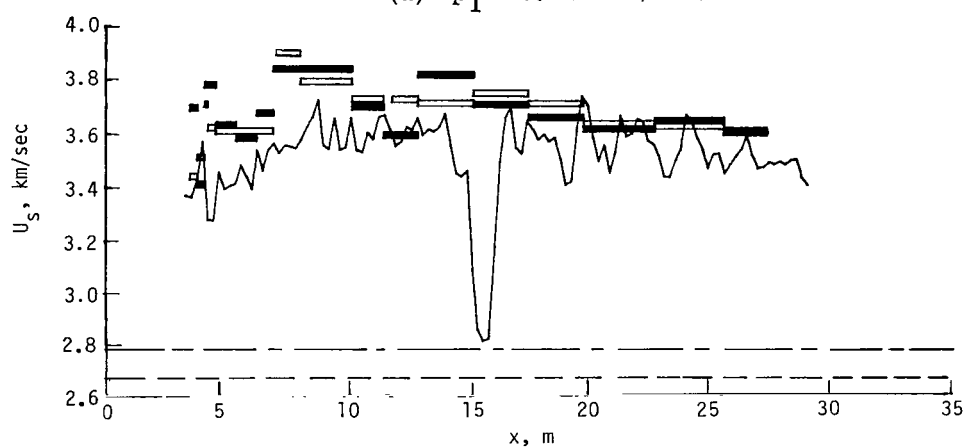
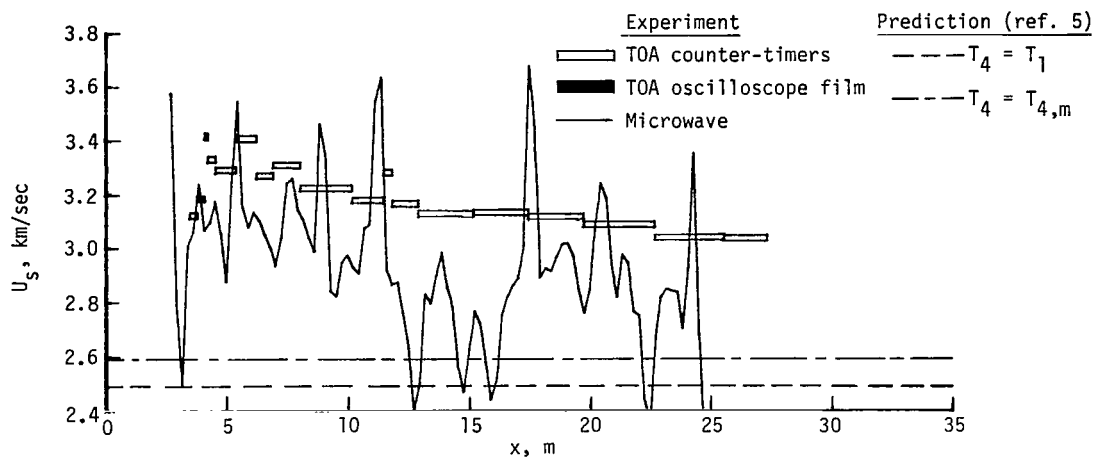
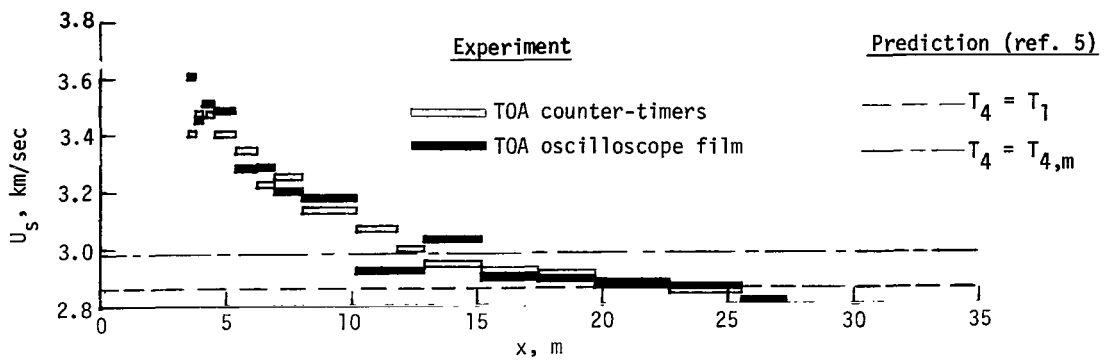
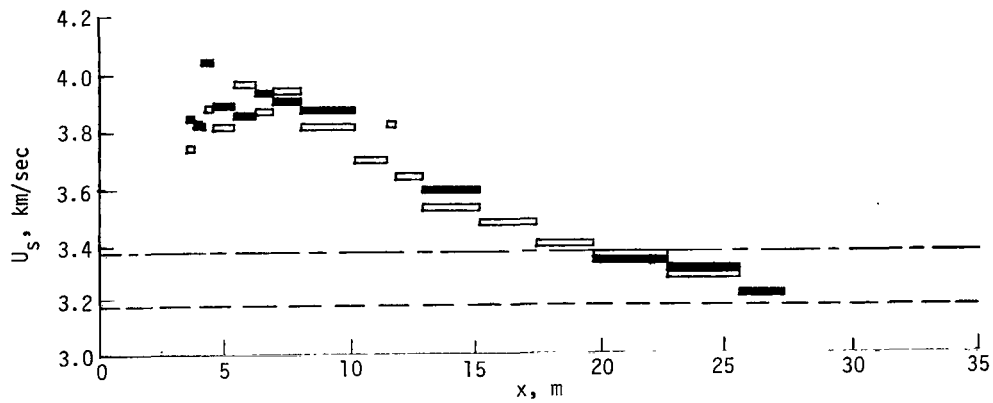


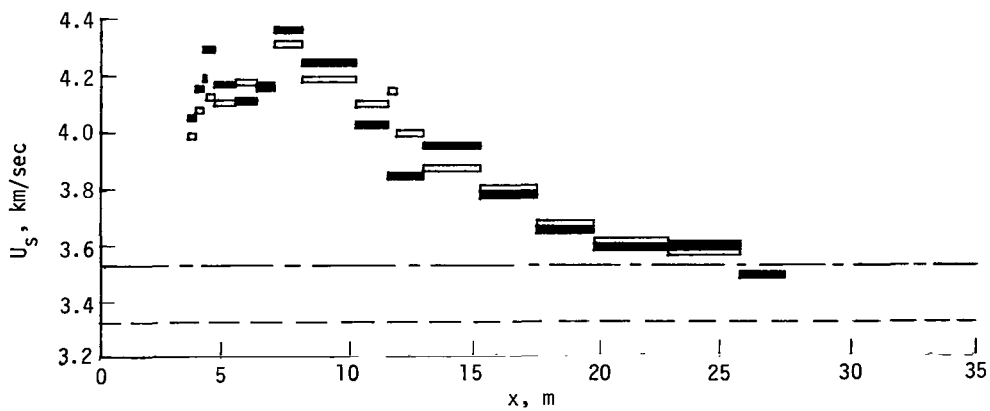
Figure 9.- Concluded.



(a) $p_1 = 34.5 \text{ kN/m}^2$.

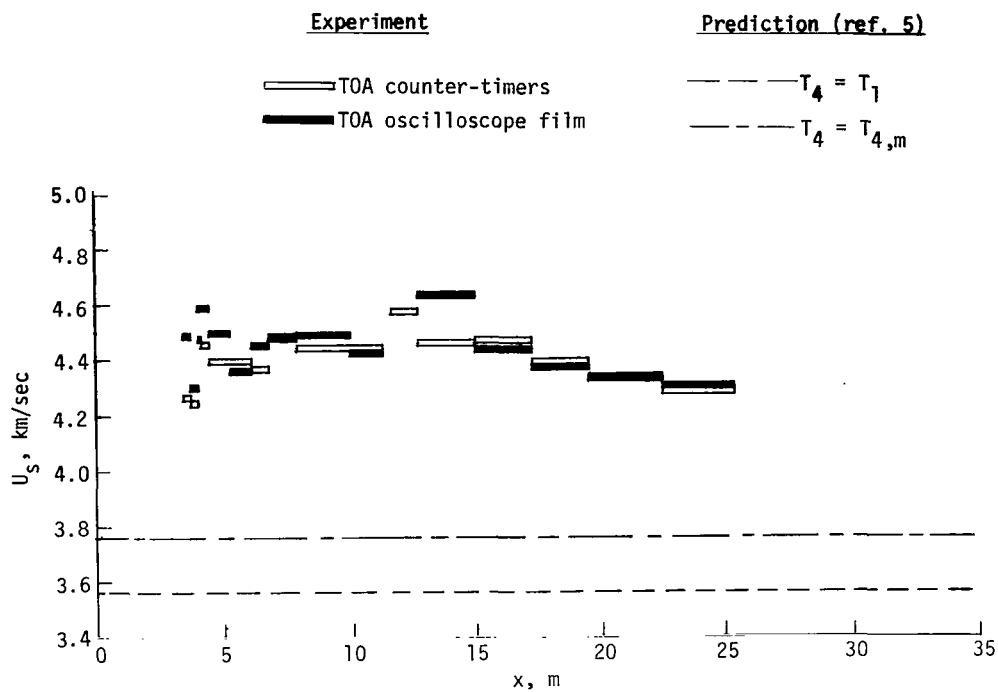


(b) $p_1 = 6.9 \text{ kN/m}^2$.

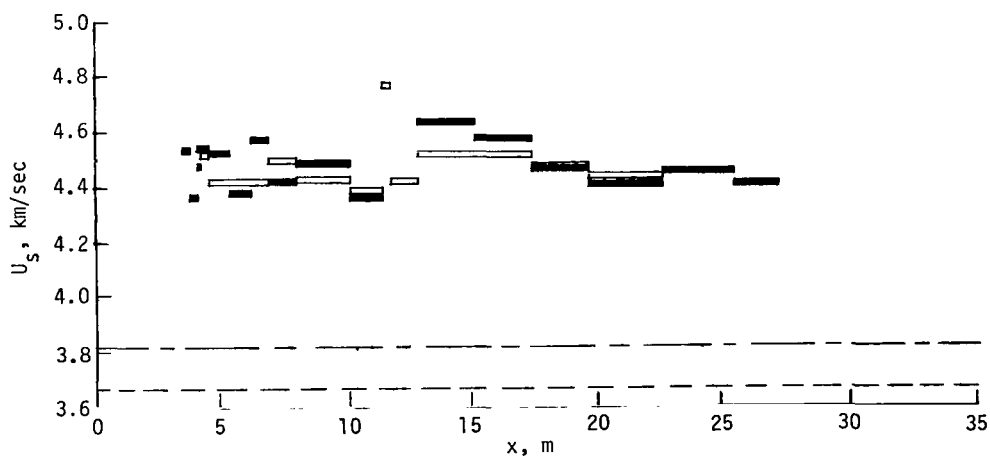


(c) $p_1 = 3.45 \text{ kN/m}^2$.

Figure 10.- Incident shock velocity as a function of distance downstream of primary diaphragm for helium.

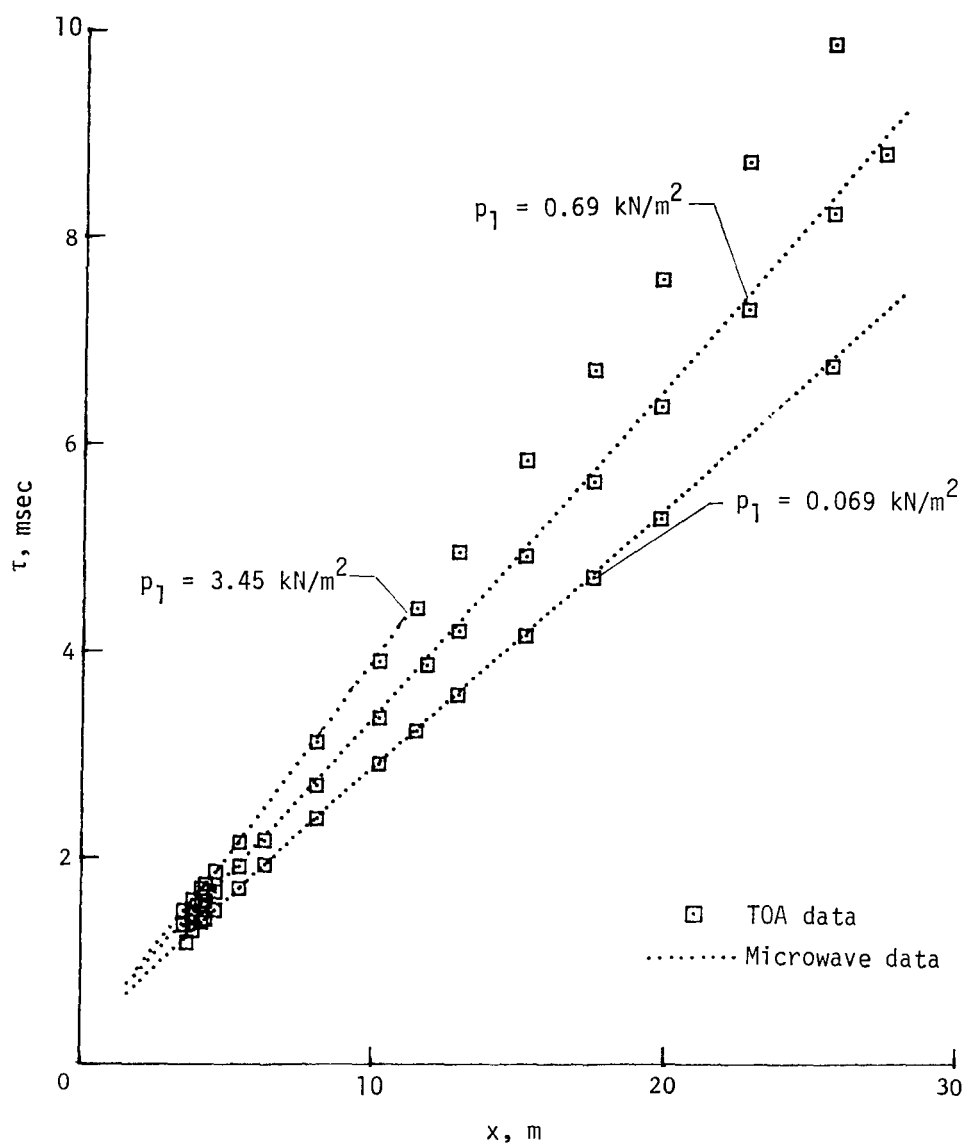


(d) $p_1 = 0.690 \text{ kN/m}^2$.



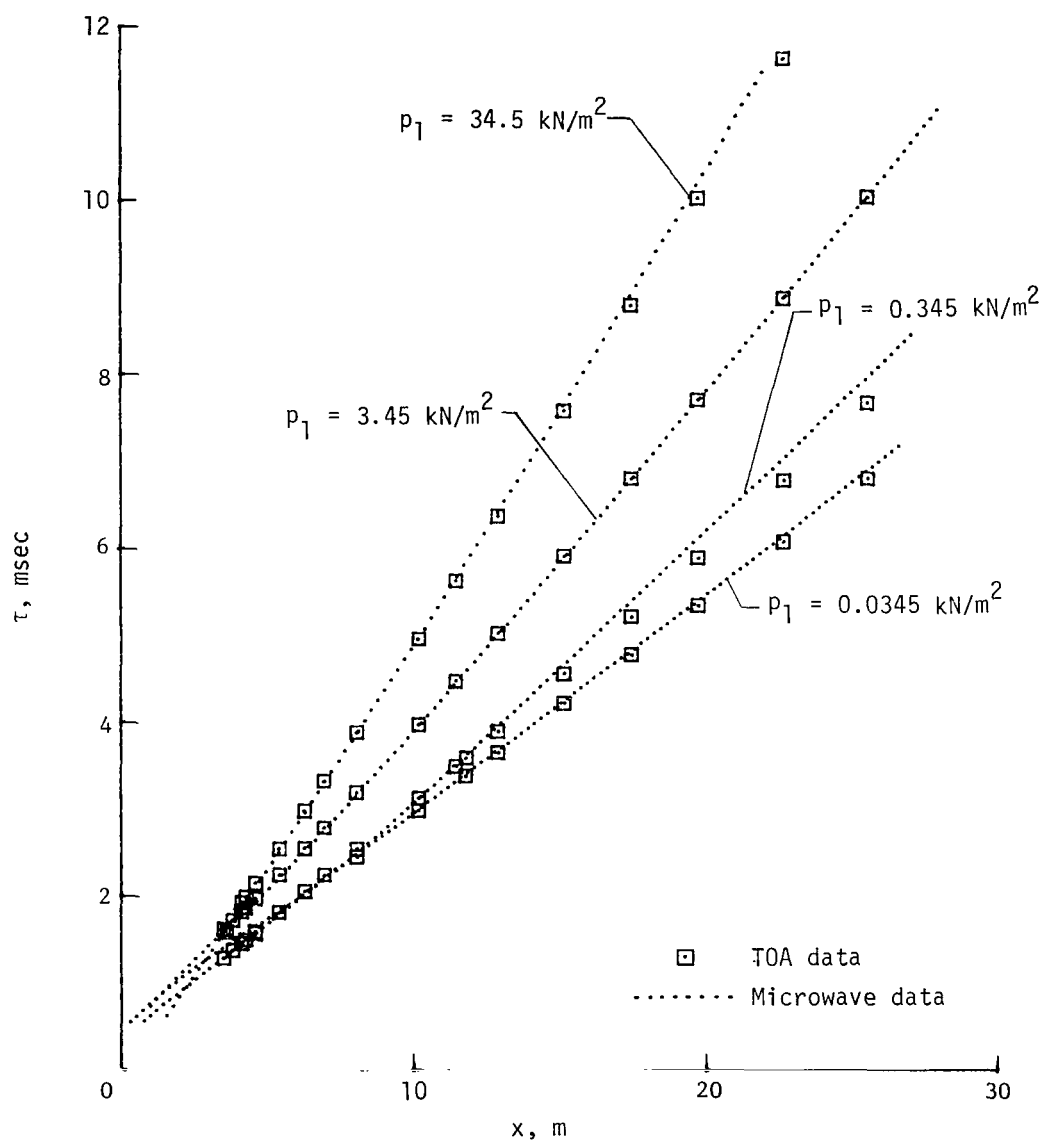
(e) $p_1 = 0.345 \text{ kN/m}^2$.

Figure 10.- Concluded.



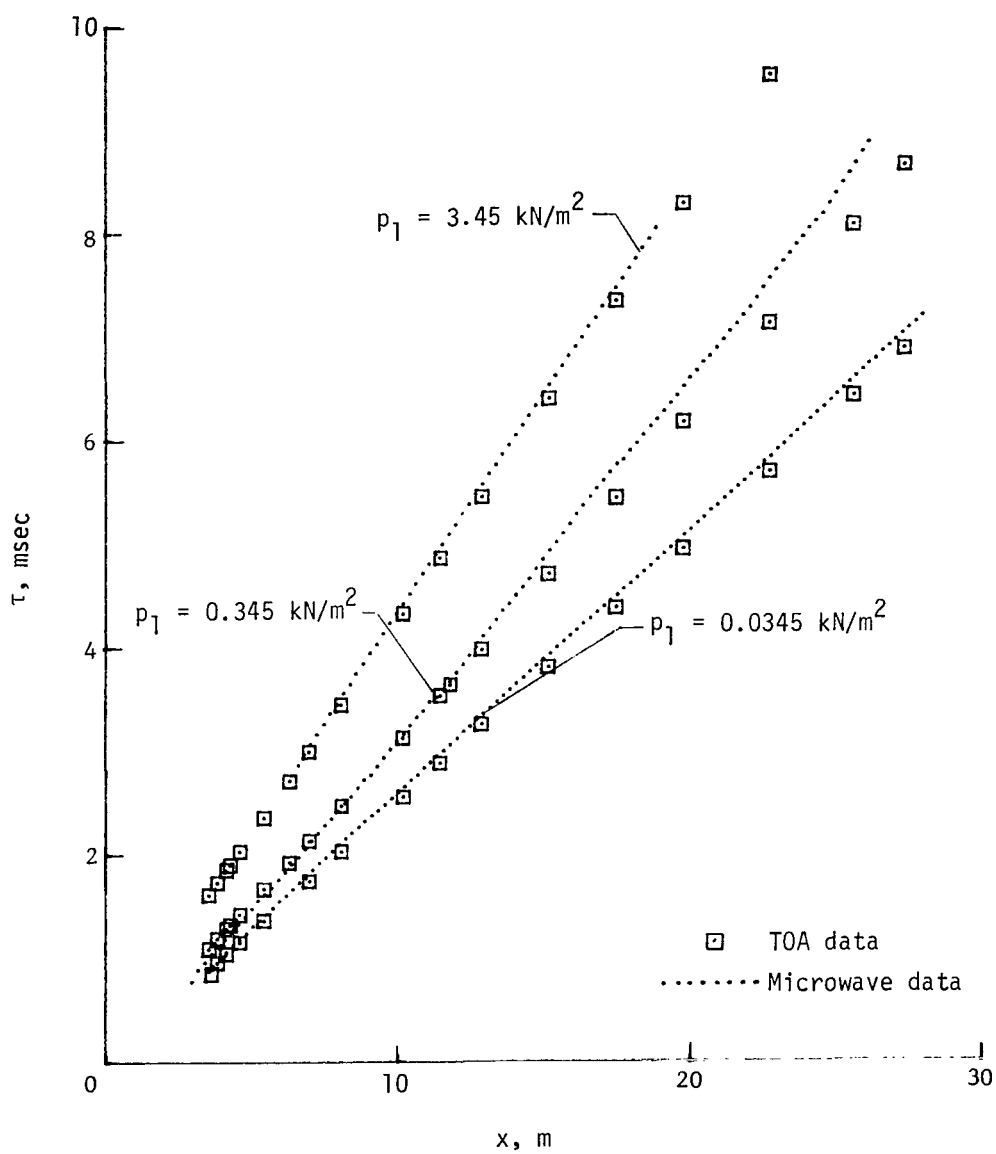
(a) Air.

Figure 11.- Time of shock arrival as a function of axial distance downstream of primary diaphragm.



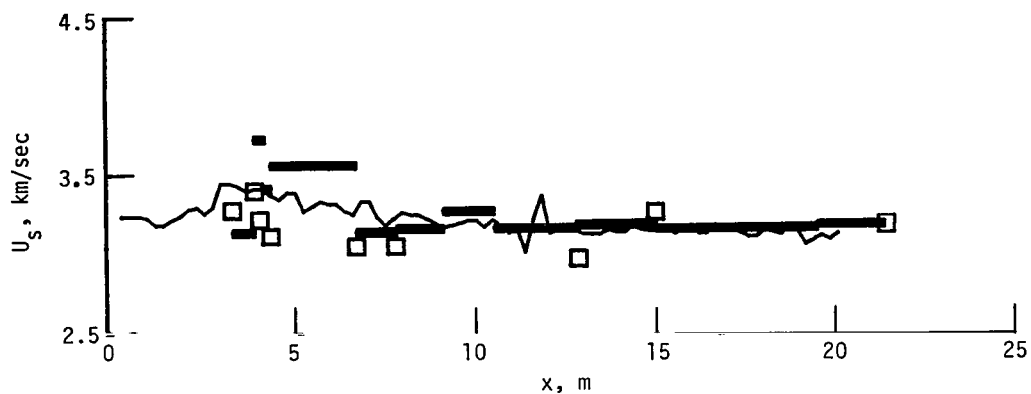
(b) Argon.

Figure 11.- Continued.

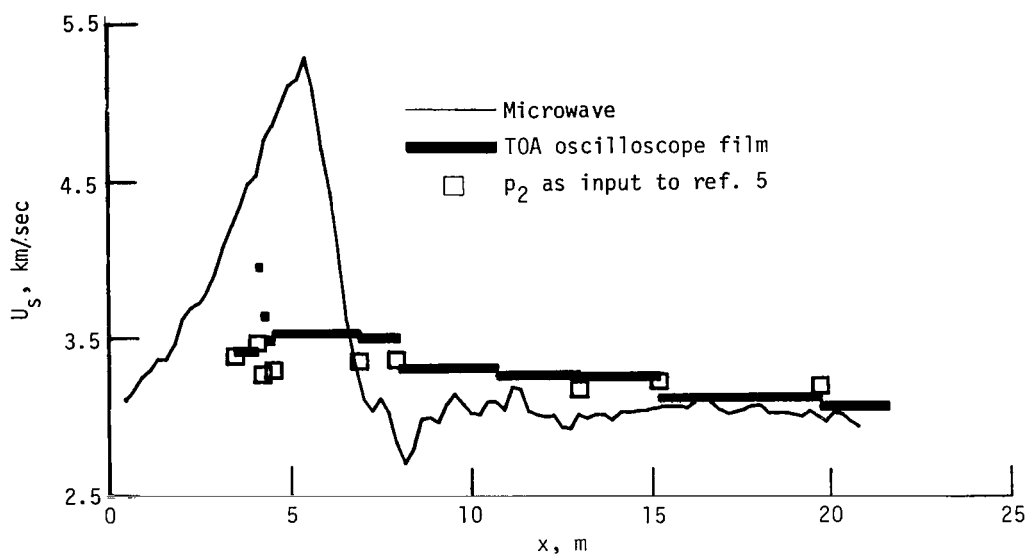


(c) CO_2 .

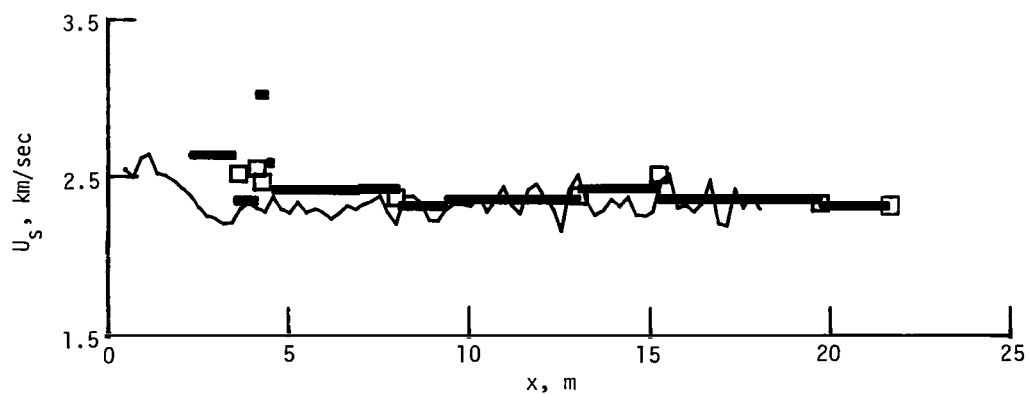
Figure 11.- Concluded.



(a) Air. $p_1 = 0.690 \text{ kN/m}^2$.



(b) Argon. $p_1 = 0.690 \text{ kN/m}^2$.



(c) CO_2 . $p_1 = 3.45 \text{ kN/m}^2$.

Figure 12.- Comparison of three methods used to infer shock velocities in various test gases as a function of distance downstream of diaphragm.

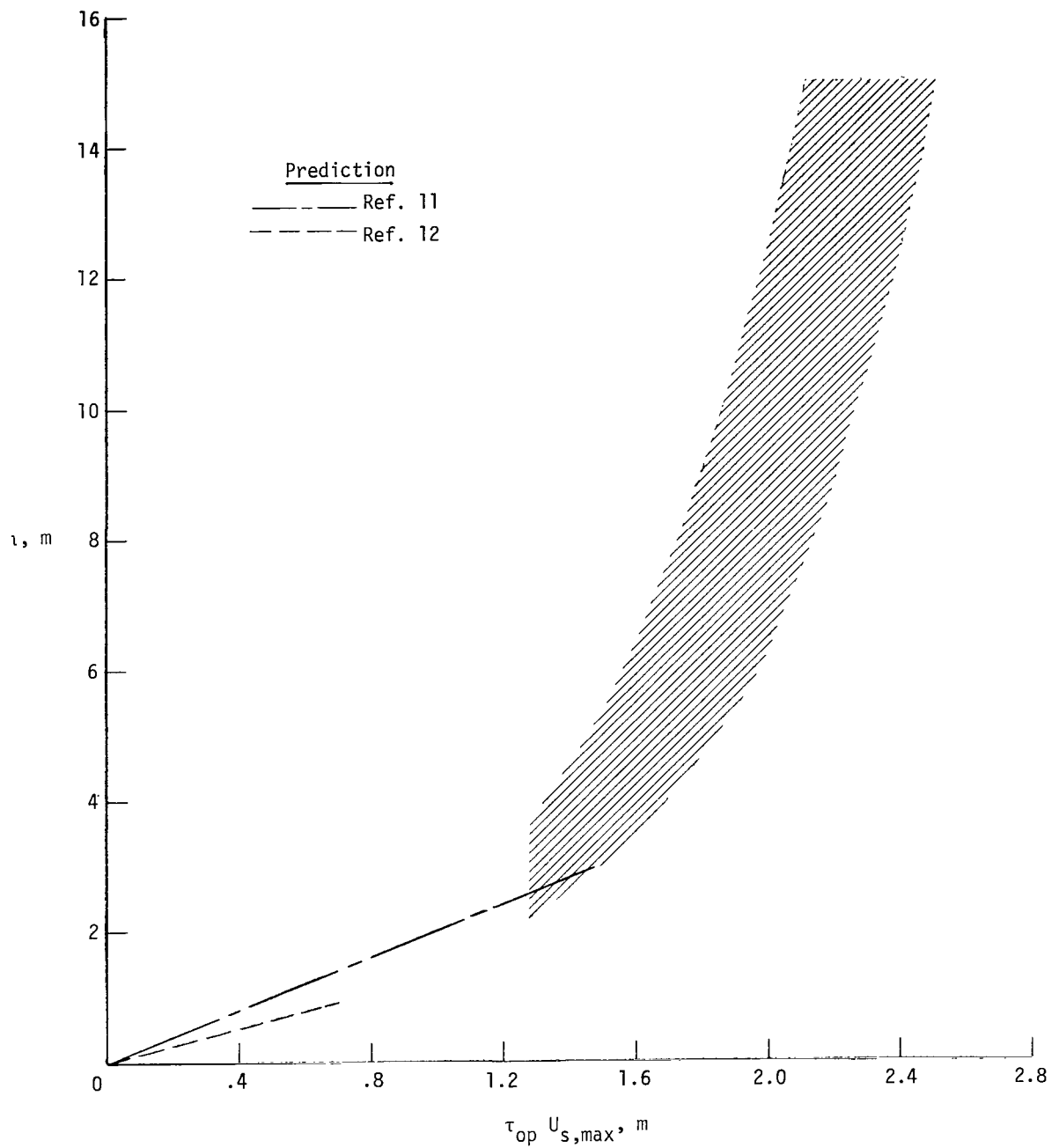


Figure 13.- Distance from diaphragm to location of maximum incident shock velocity as function of product of maximum shock velocity and diaphragm opening time. Shaded region denotes present data for four test gases, double-diaphragm mode of operation, and $p_4 \approx 34 \text{ MN/m}^2$.

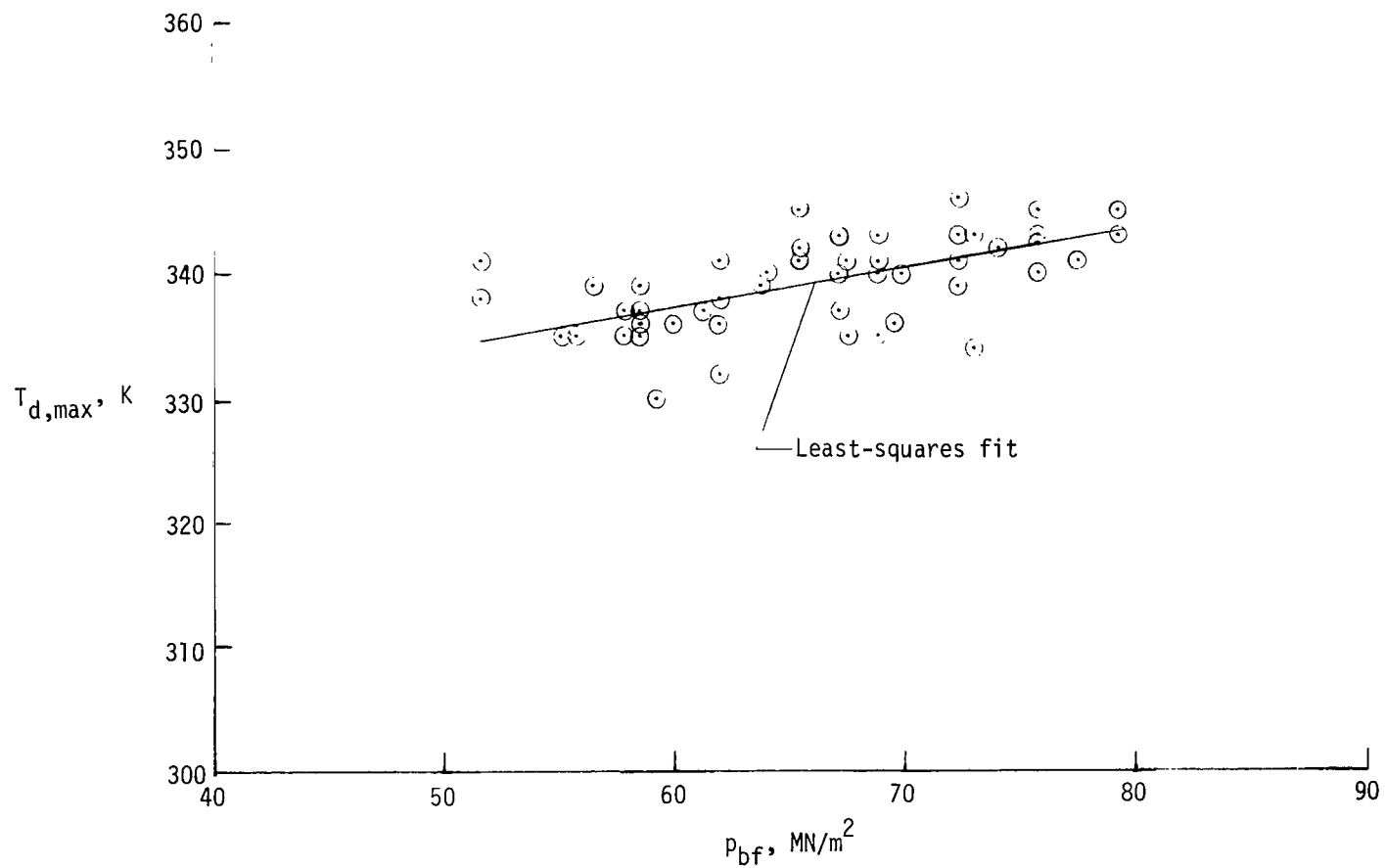
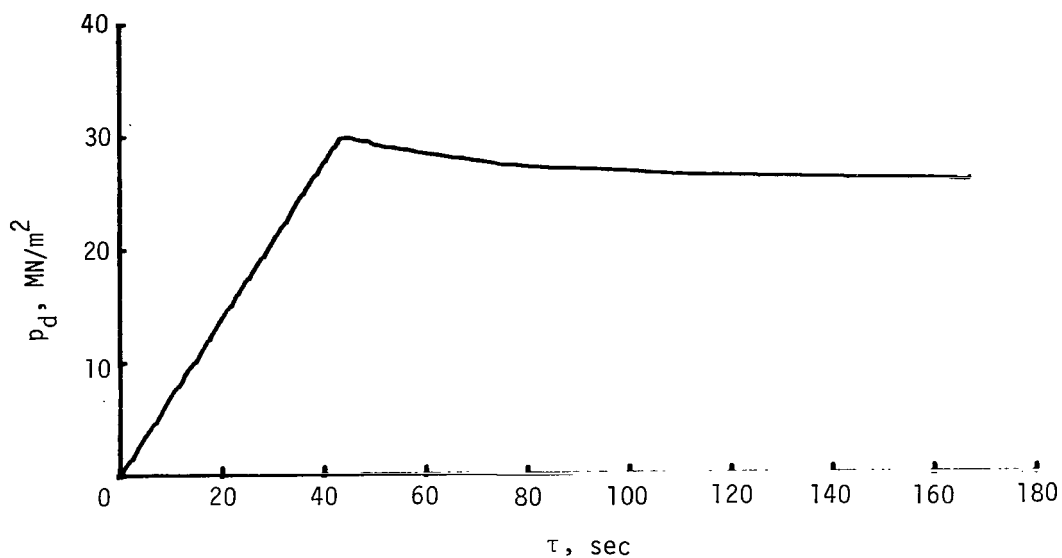
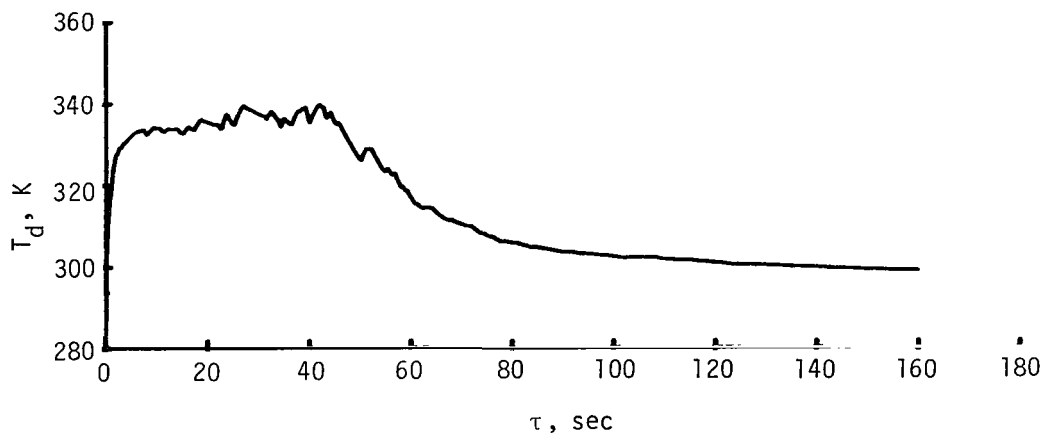


Figure 14.- Measured maximum helium driver temperature during pressurization as a function of bottle-field supply pressure.

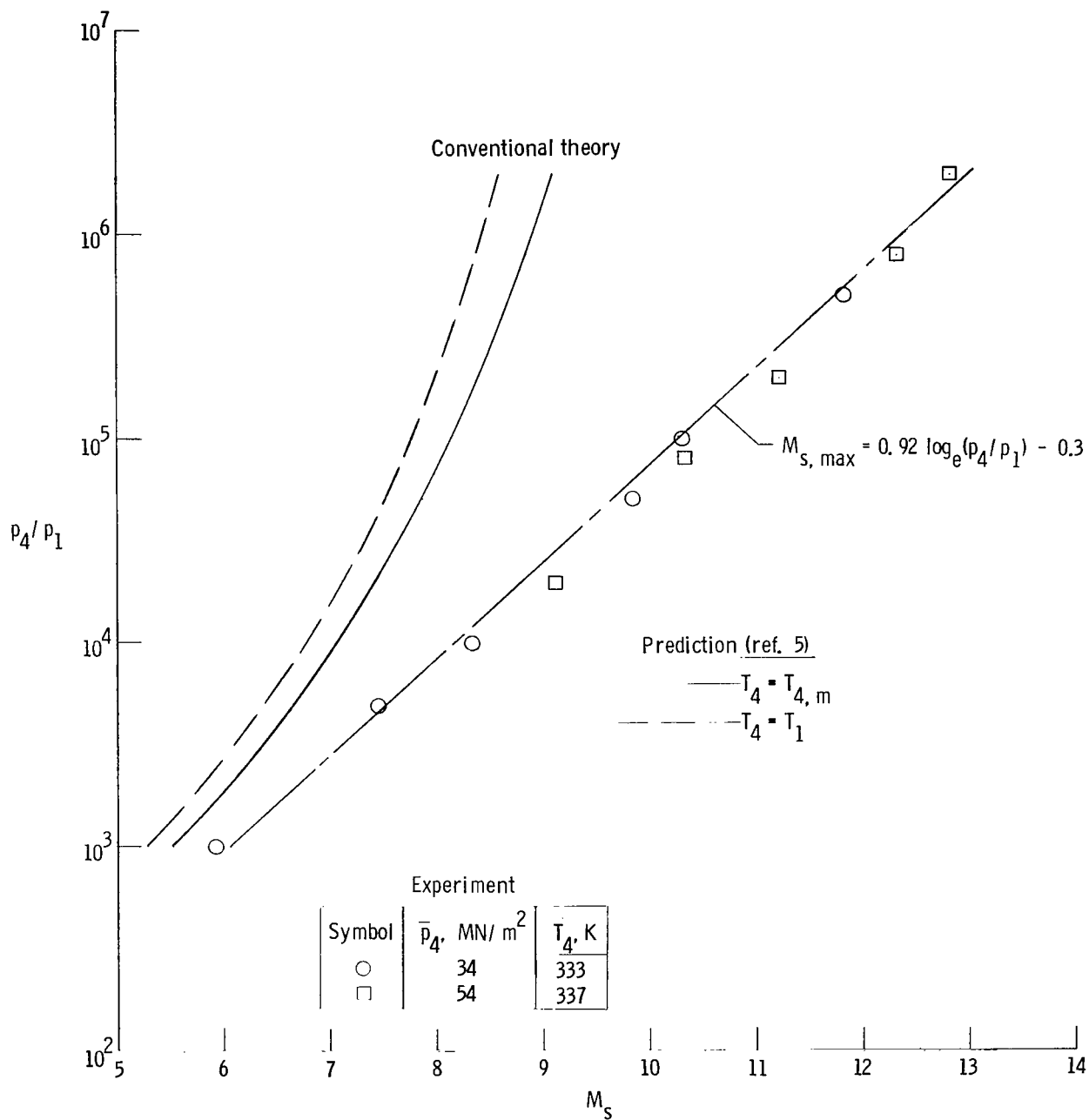


(a) Driver-gas pressure.



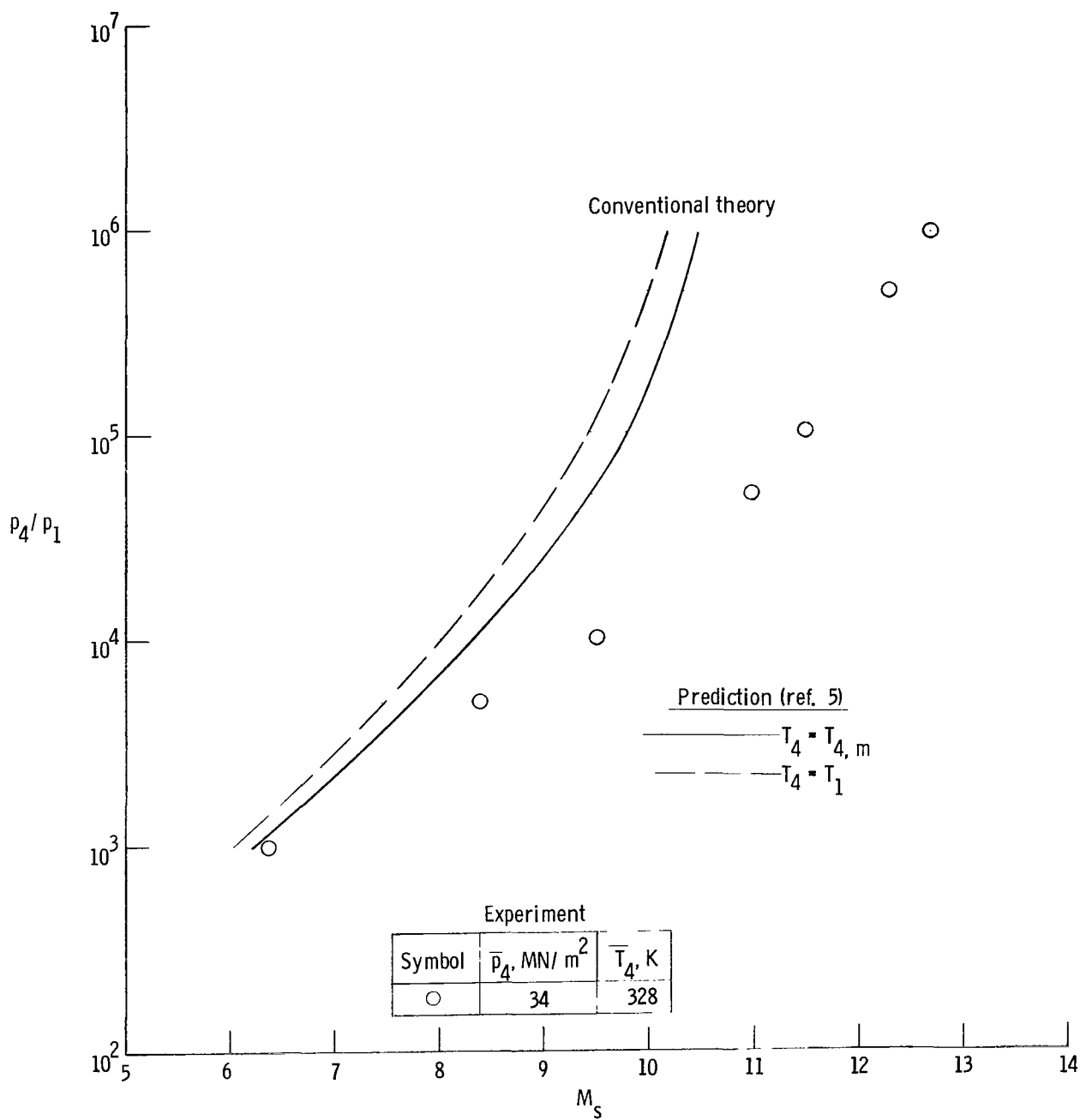
(b) Driver-gas temperature.

Figure 15.- Time history of helium driver pressure and temperature during pressurization of driver section.



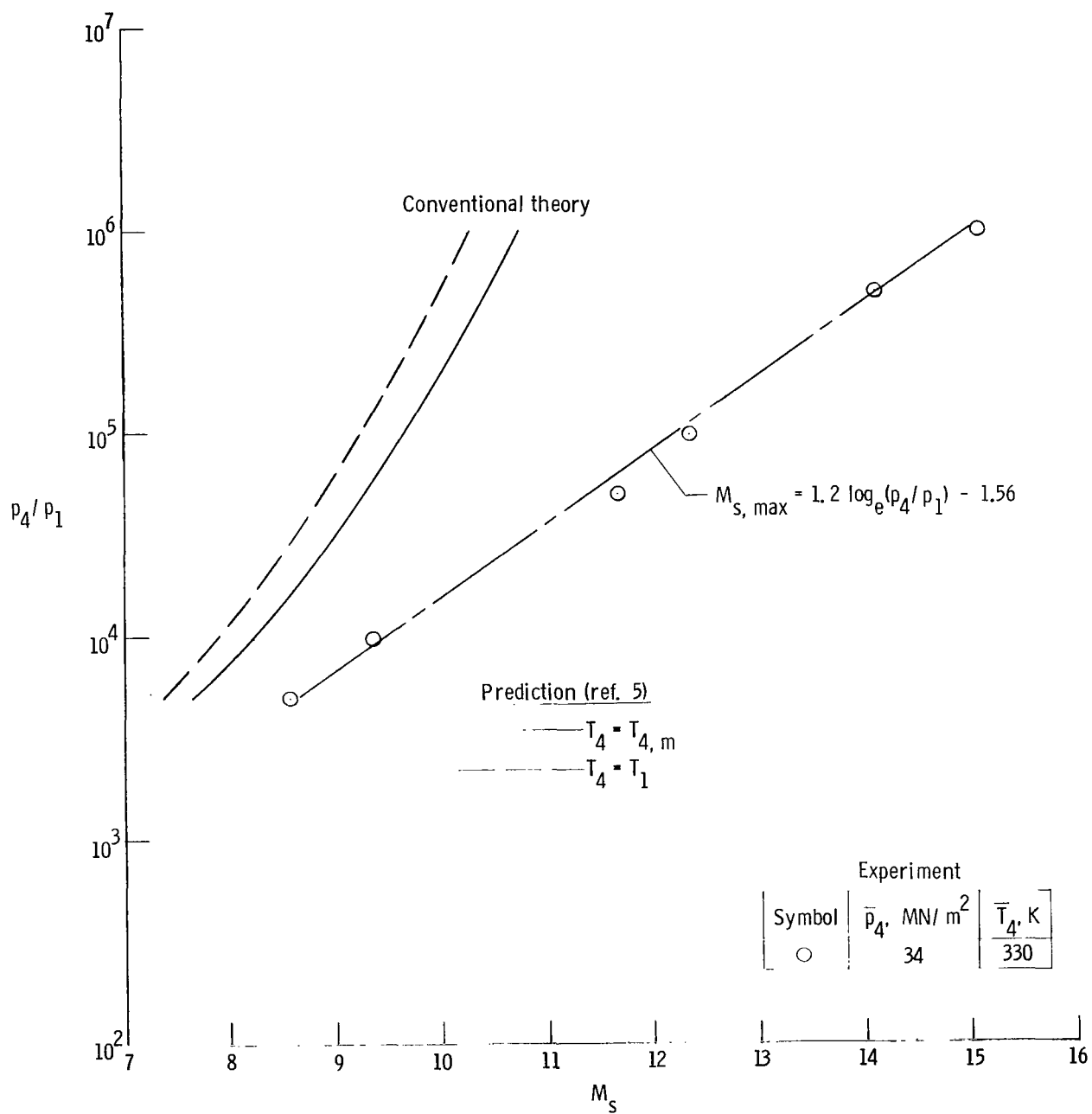
(a) Air.

Figure 16.- Measured maximum incident shock Mach number in various test gases and prediction from conventional real-gas shock-tube theory.



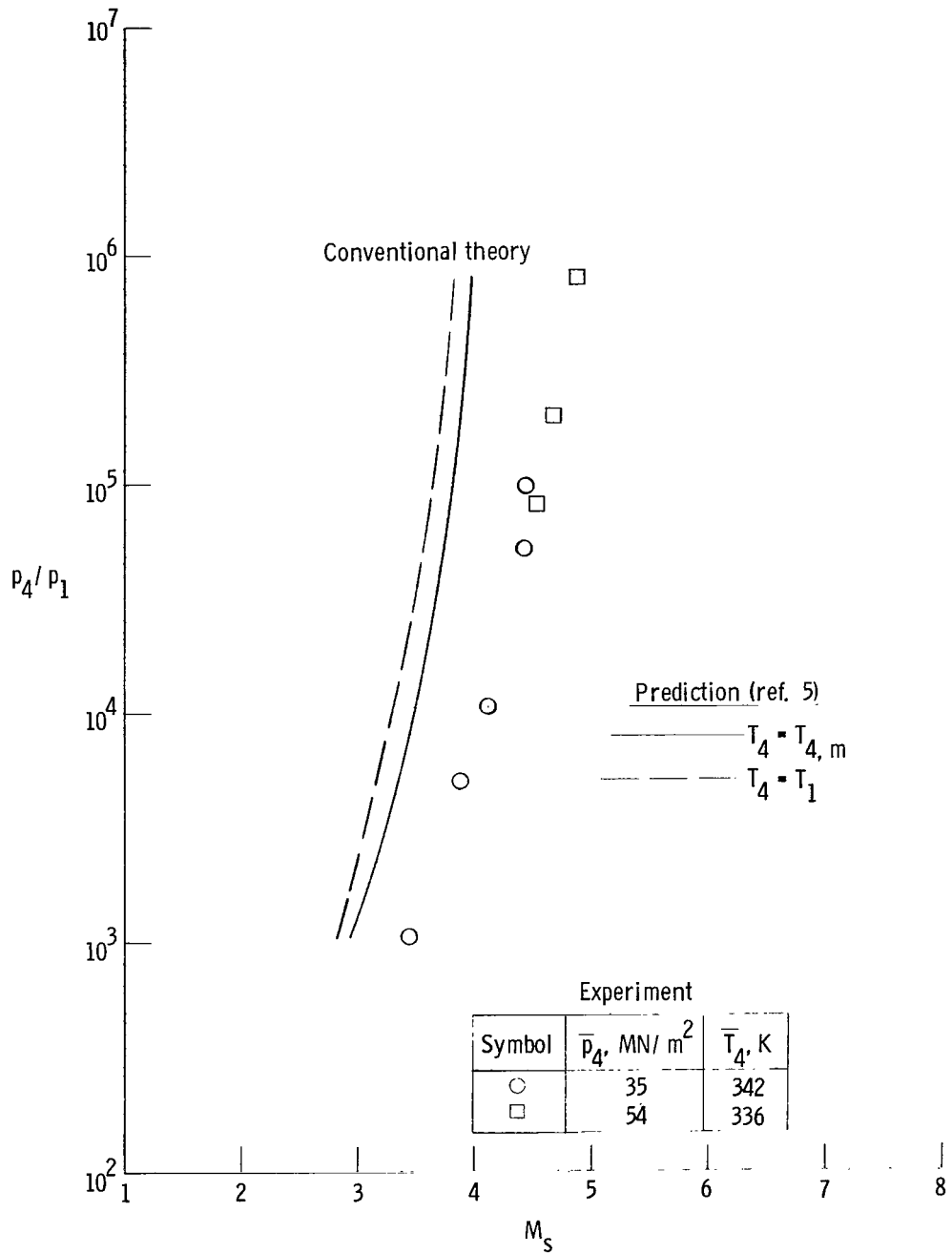
(b) Argon.

Figure 16.- Continued.



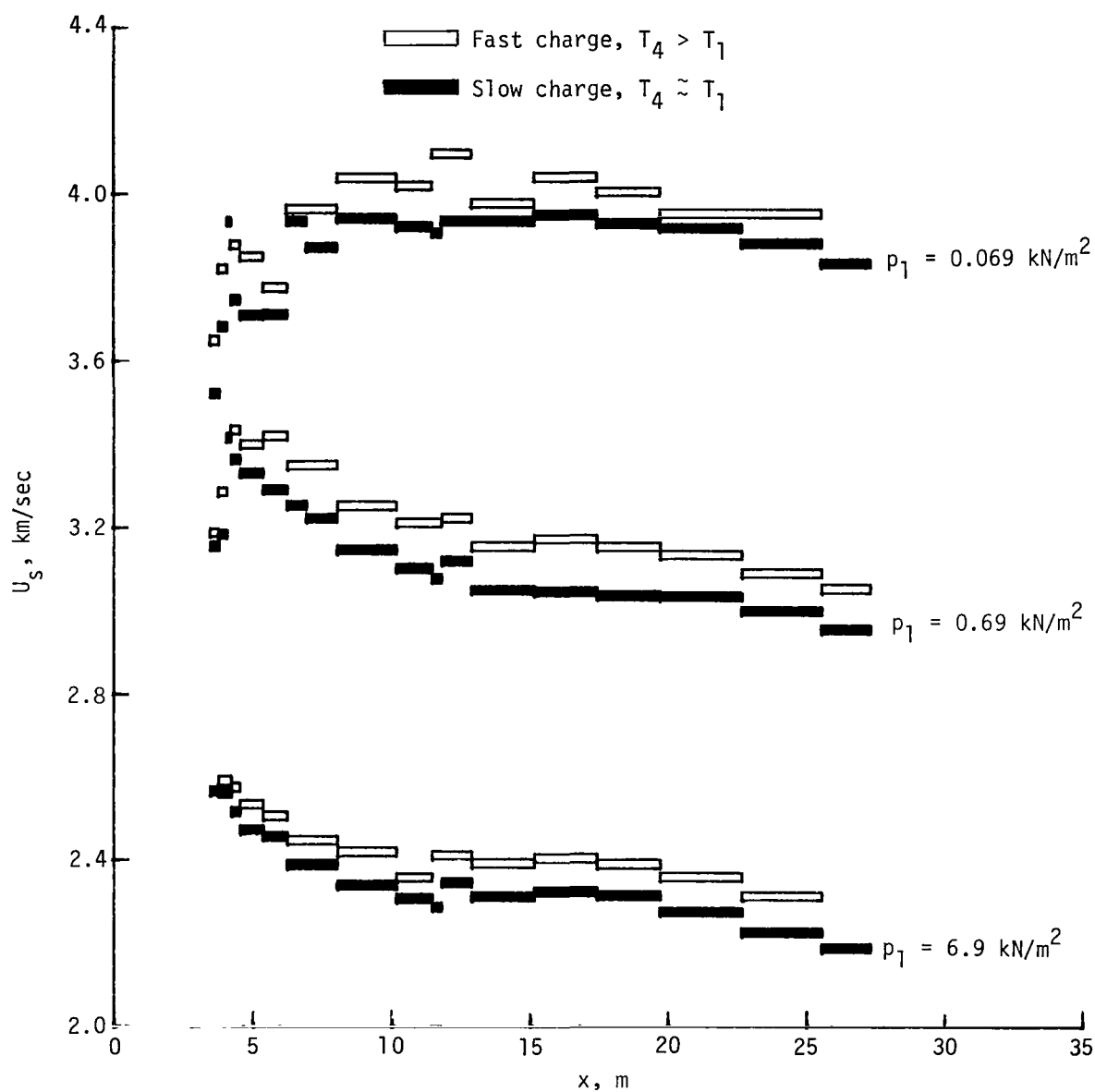
(c) CO₂.

Figure 16.- Continued.



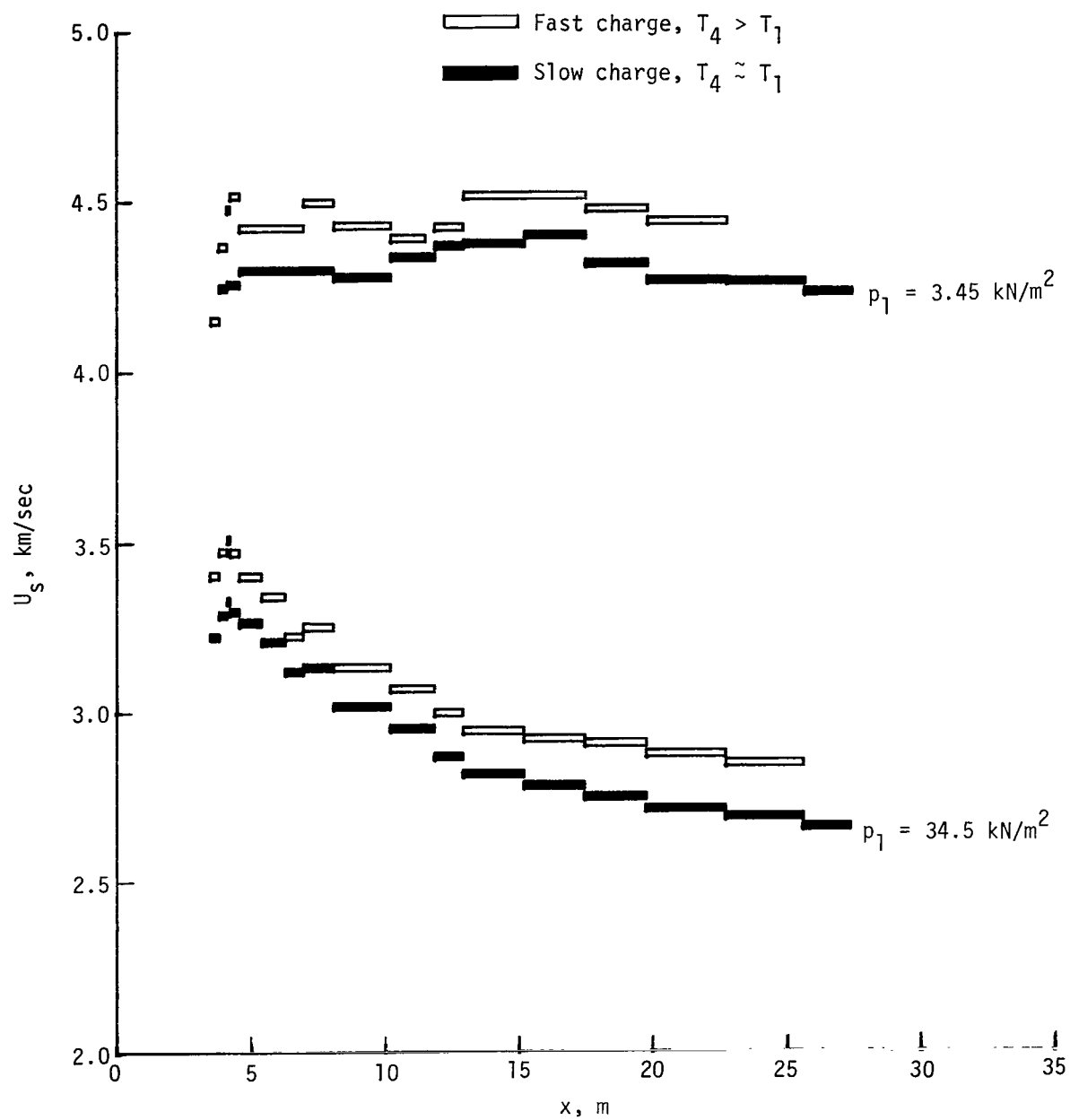
(d) Helium.

Figure 16.- Concluded.



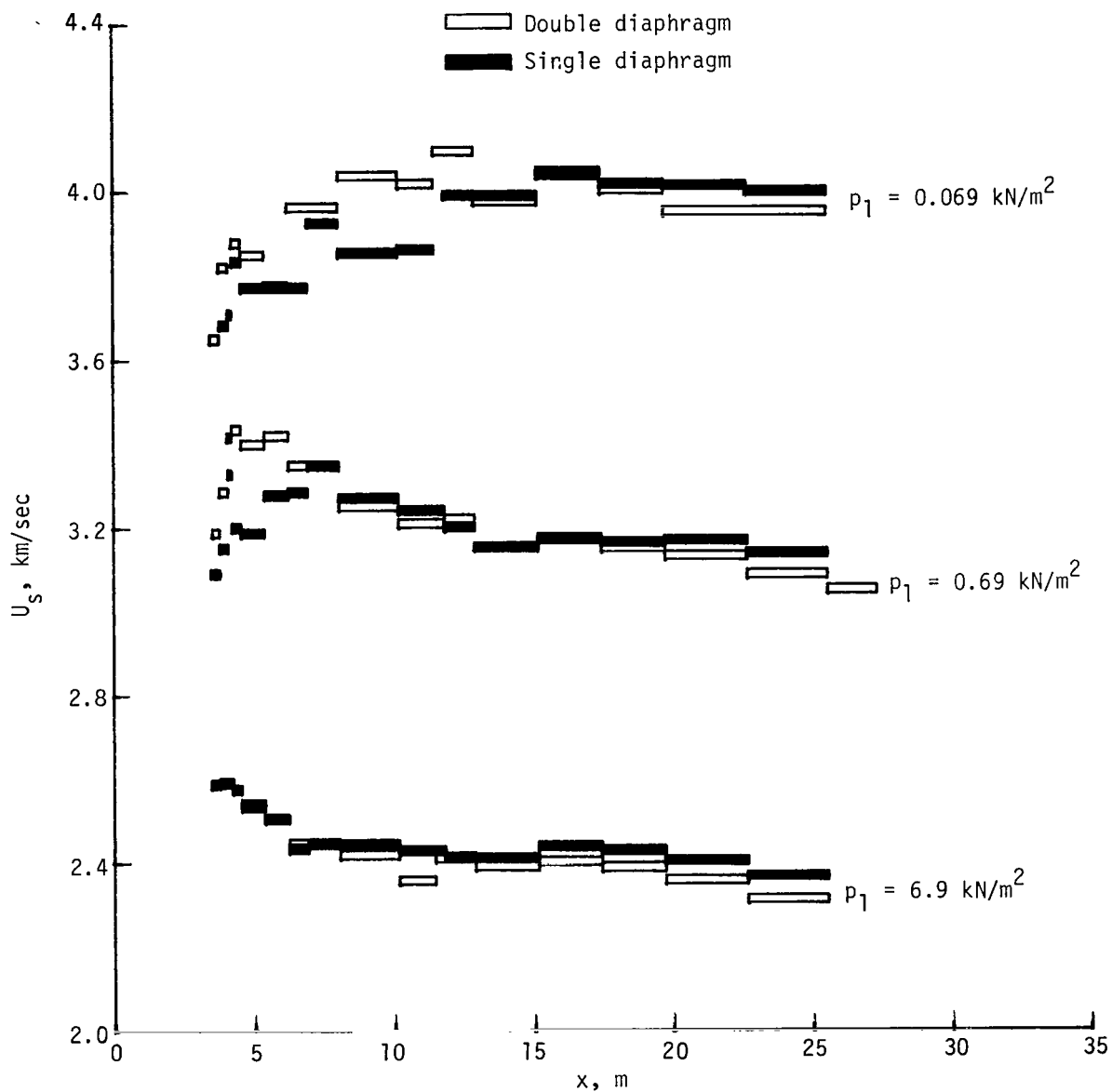
(a) Air.

Figure 17.- Effect of pressurization time of driver section on incident shock velocity for selected values of quiescent pressure. Measured U_s obtained from counter-timer readings; $p_4 \approx 34 \text{ MN/m}^2$.



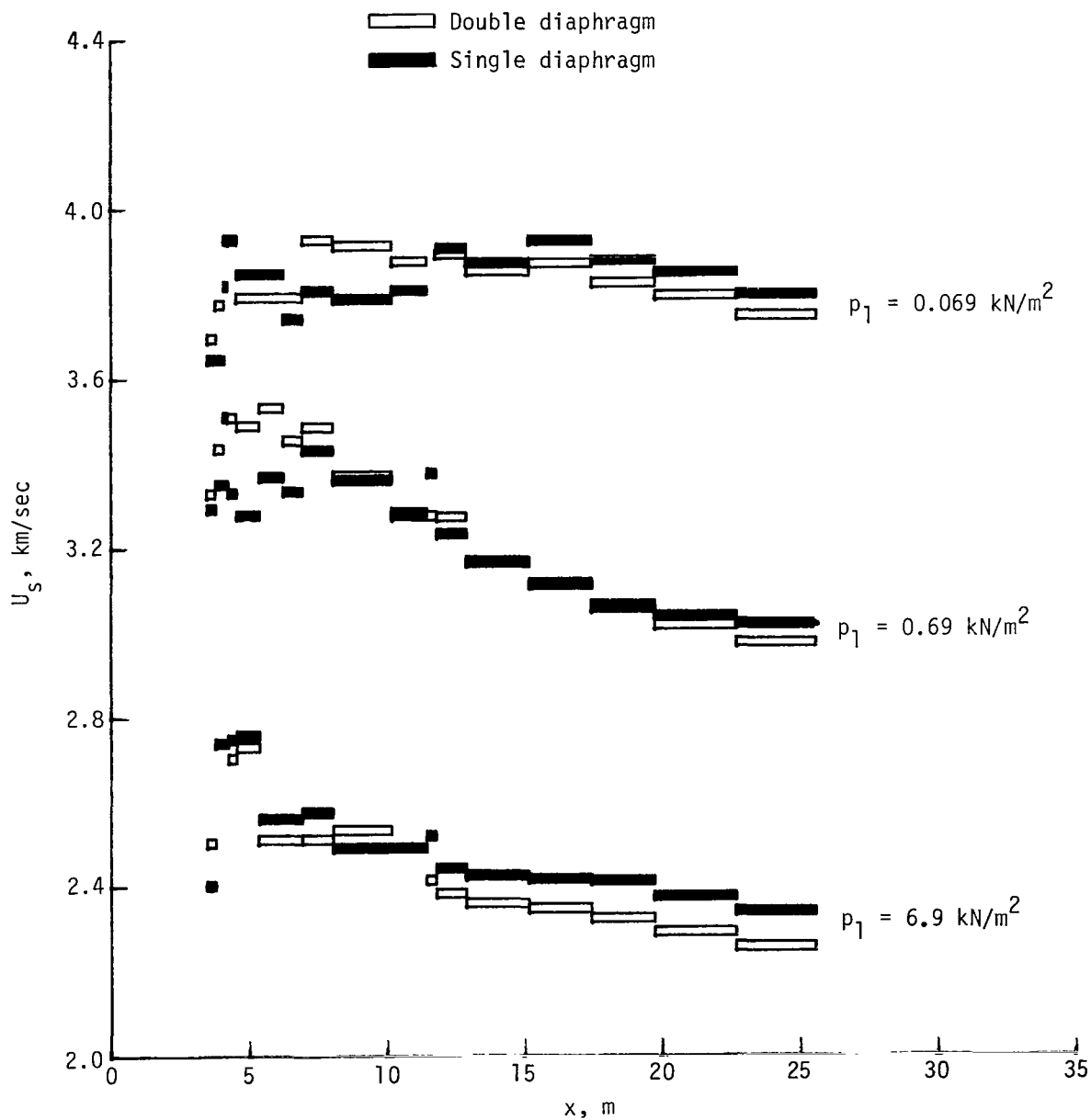
(b) Helium.

Figure 17.- Concluded.



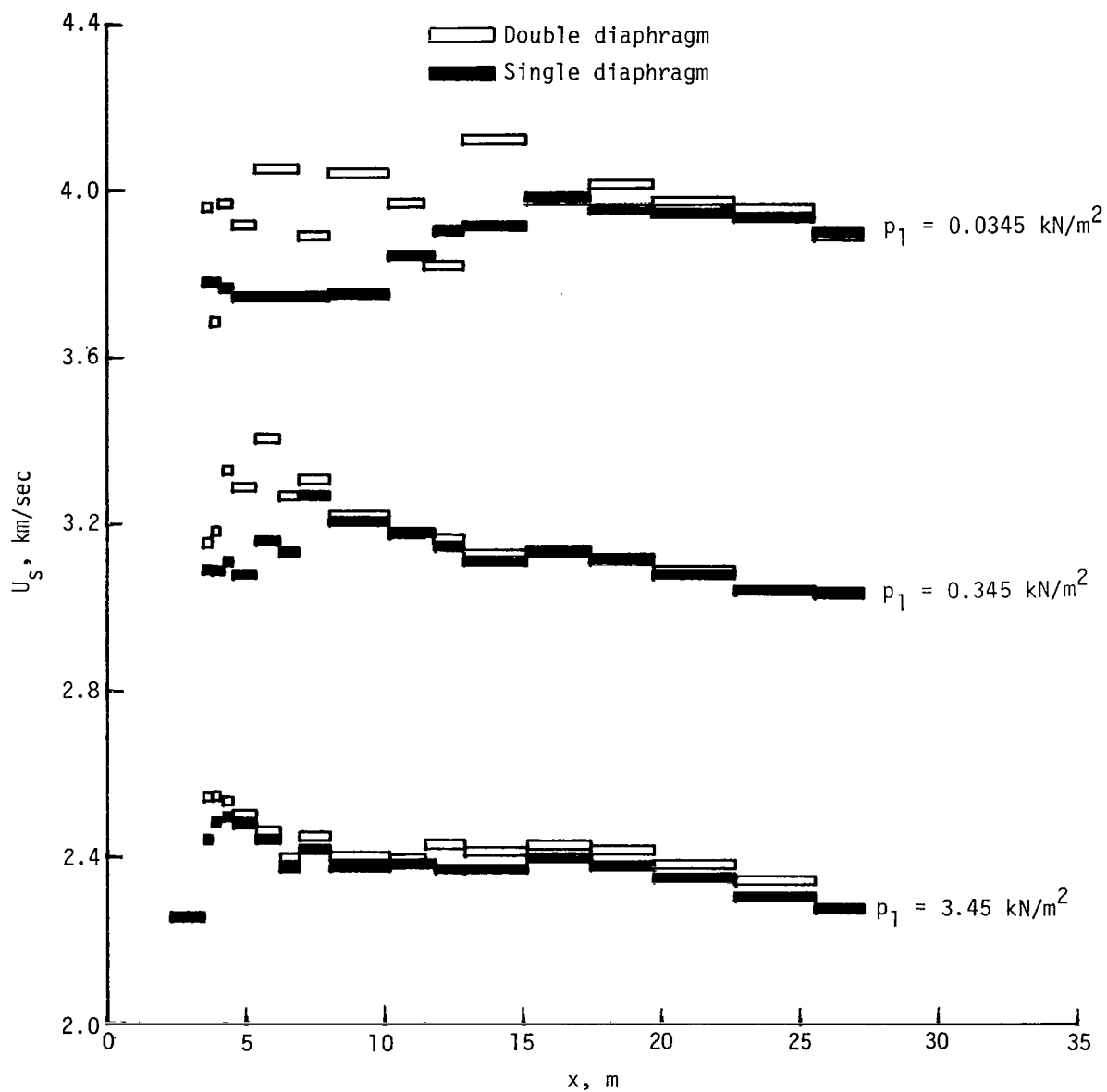
(a) Air.

Figure 18.- Measured incident shock velocities for double- and single-diaphragm modes of operation with various test gases. Measured U_s obtained from counter-timer readings; $p_4 \approx 34 \text{ MN/m}^2$.



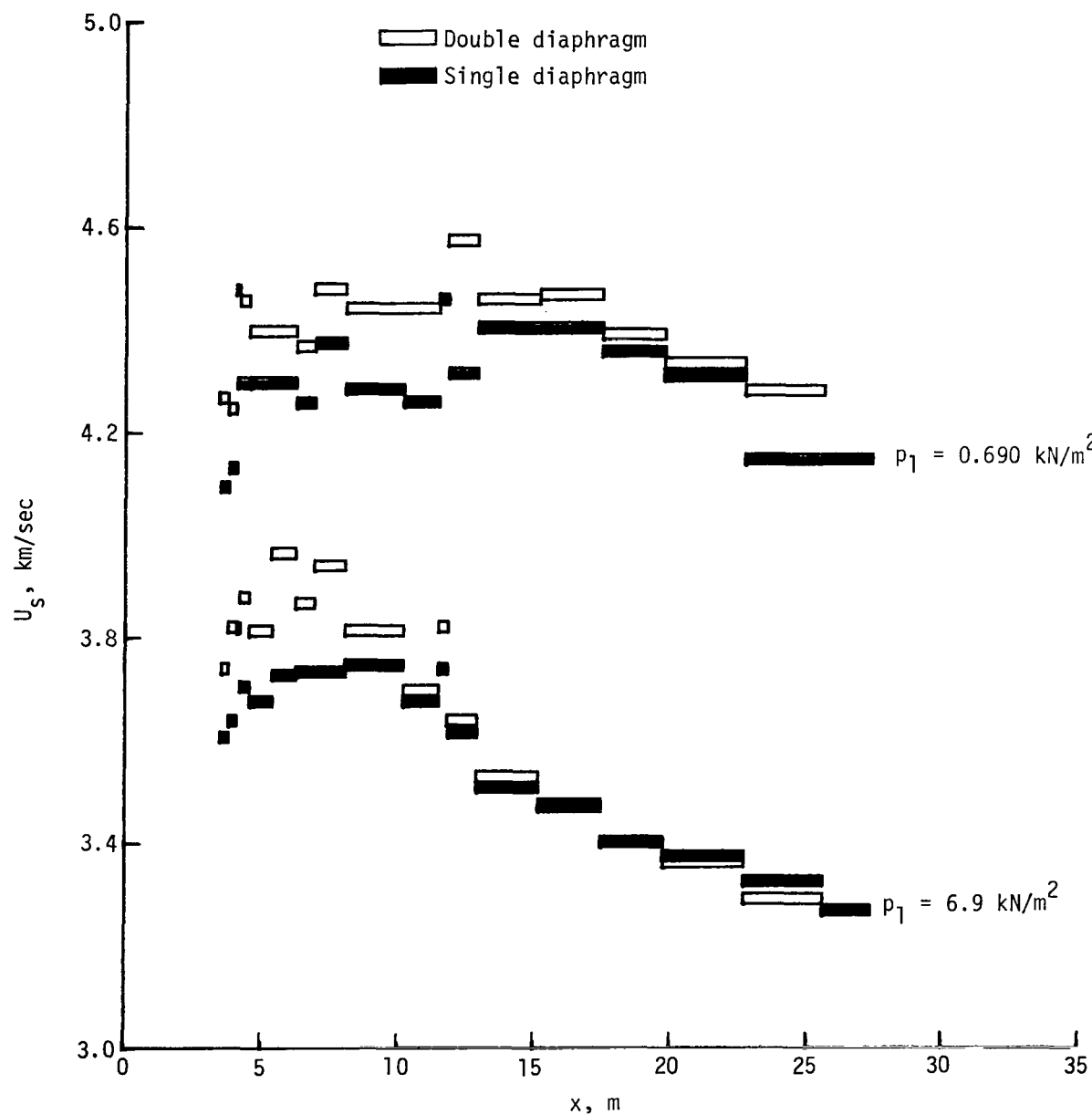
(b) Argon.

Figure 18.- Continued.



(c) CO_2 .

Figure 18.- Continued.



(d) Helium.

Figure 18.- Concluded.

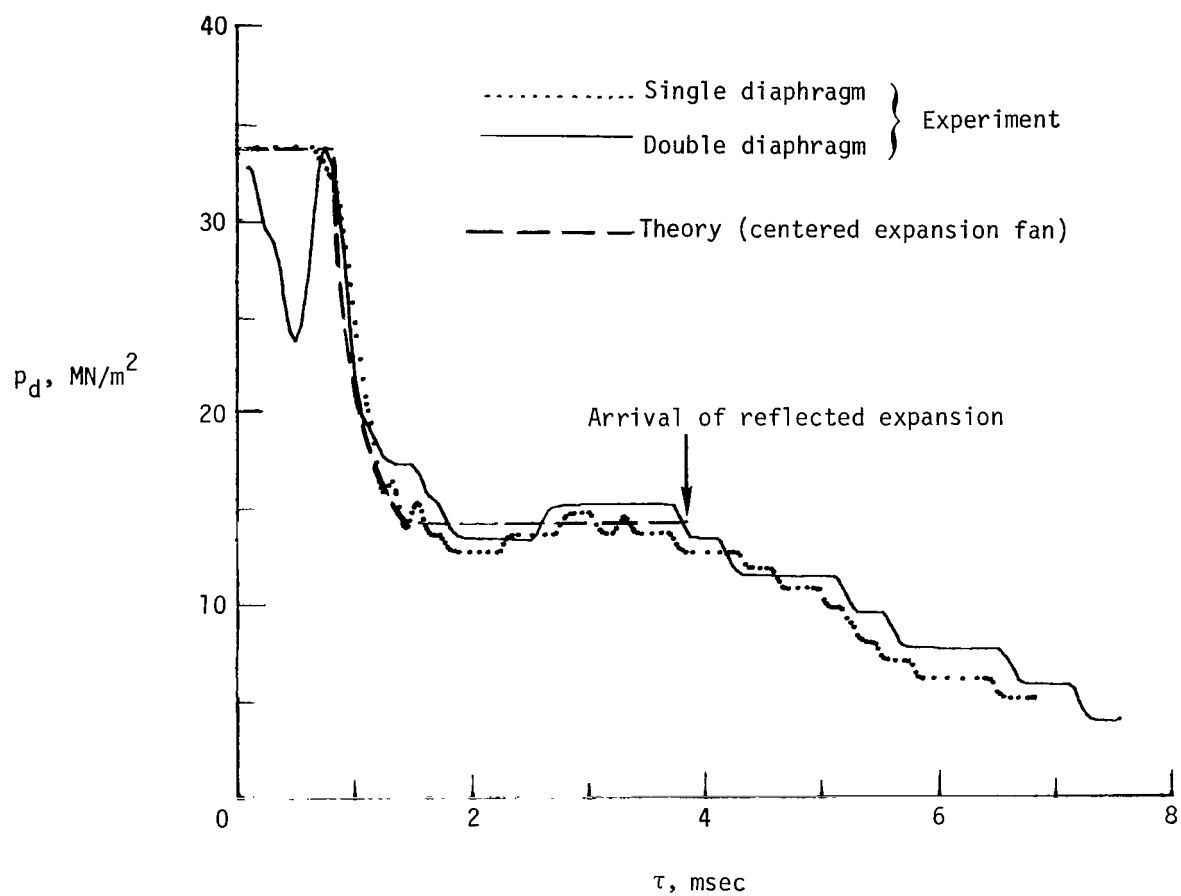
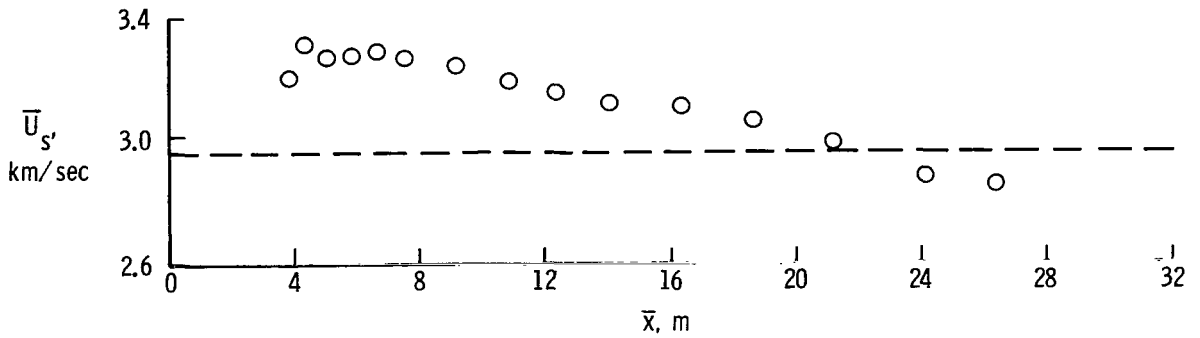
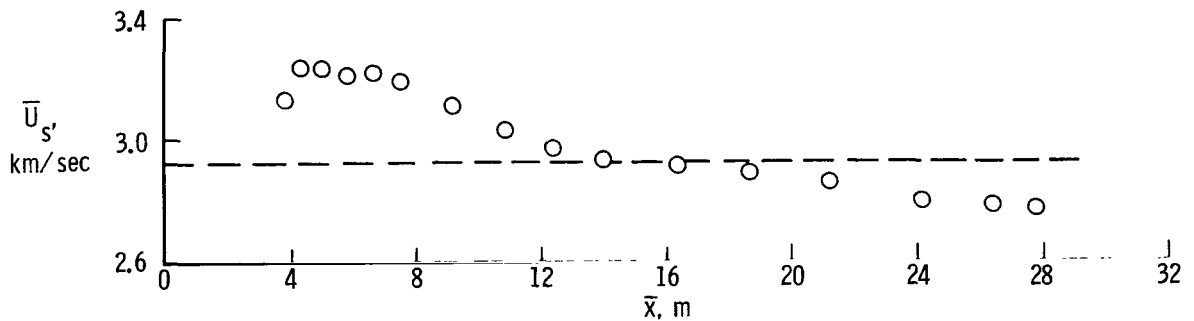


Figure 19.- Helium driver pressure as a function of time for single- and double-diaphragm modes of operation.

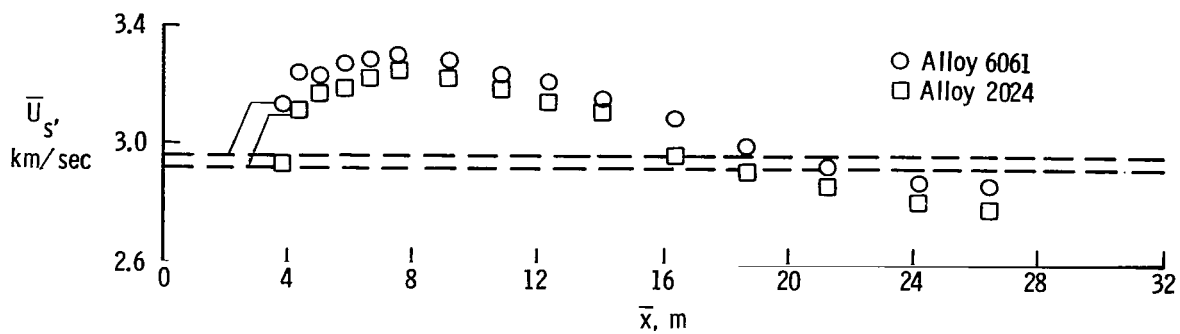


(a) Laminated plastic (polyethylene terephthalate).

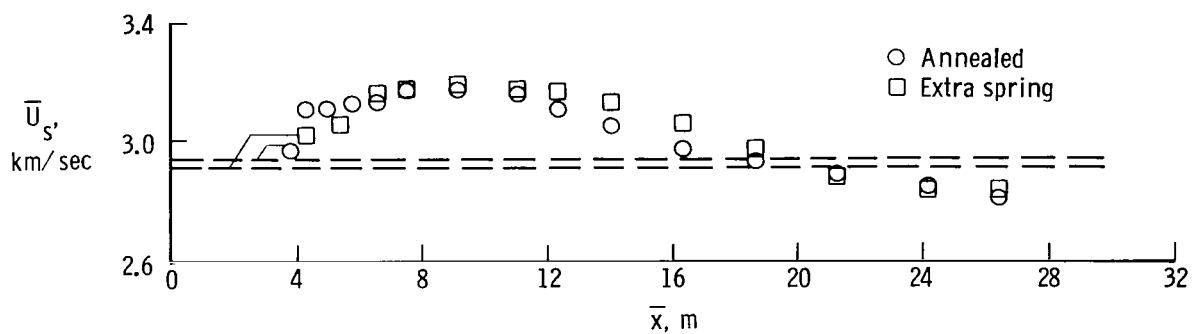


(b) Stainless steel, AISI type 304.

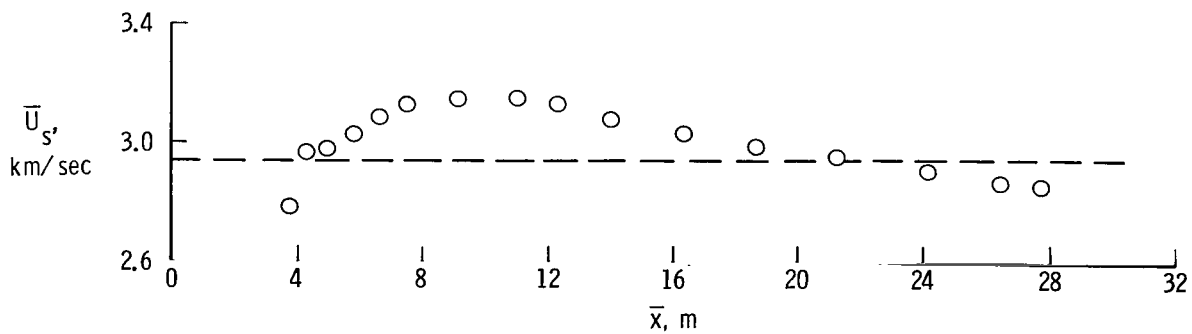
Figure 20.- Incident shock velocity as a function of distance downstream of diaphragm for various diaphragm materials. Helium as test gas; $T_4 \approx 333 \text{ K}$; $p_4/p_1 \approx 1030$. Dashed lines denote conventional theory (ref. 5) with measured p_4 and T_4 as inputs.



(c) Aluminum.



(d) Brass.



(e) Copper, cold roll, light.

Figure 20.- Concluded.

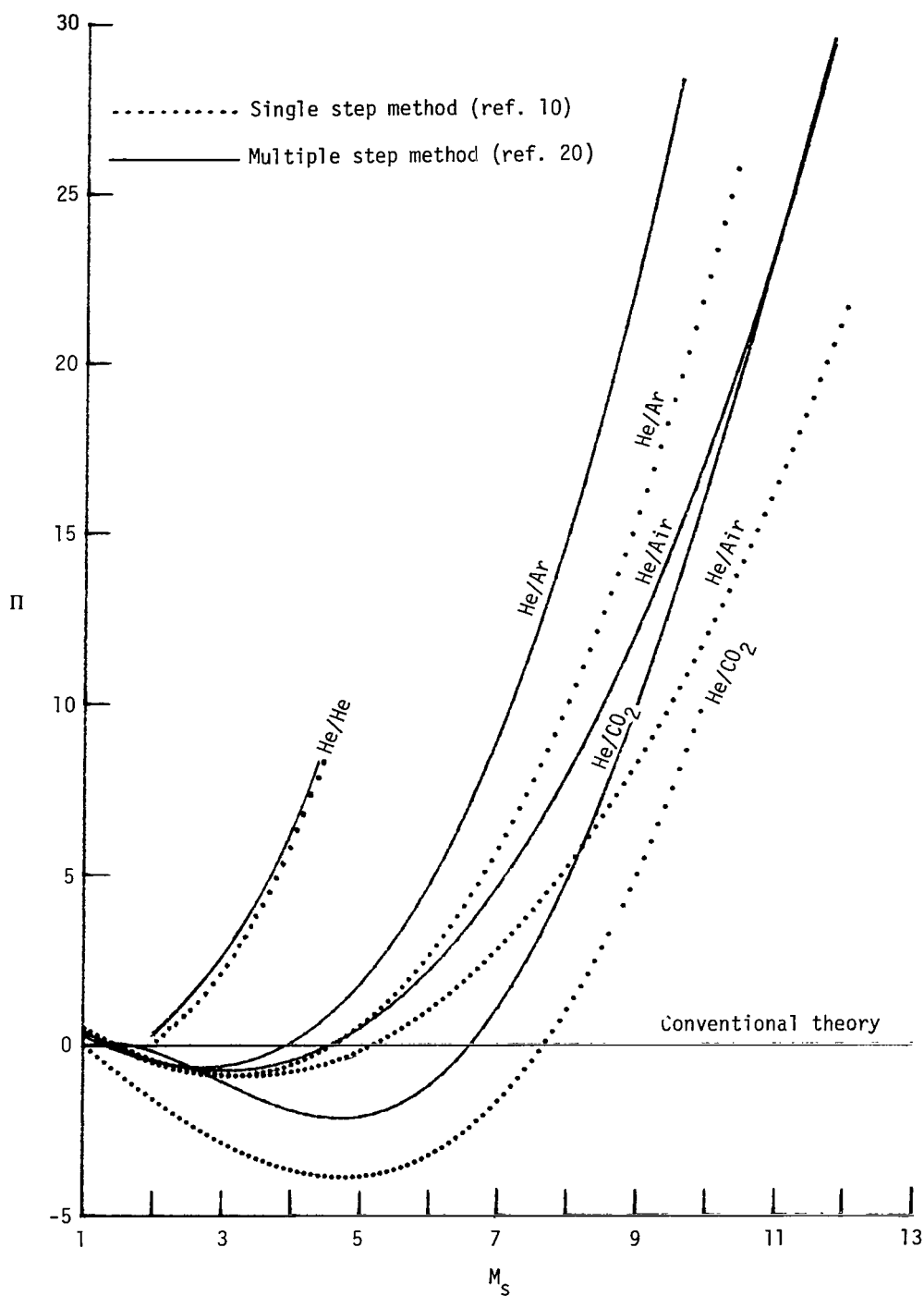
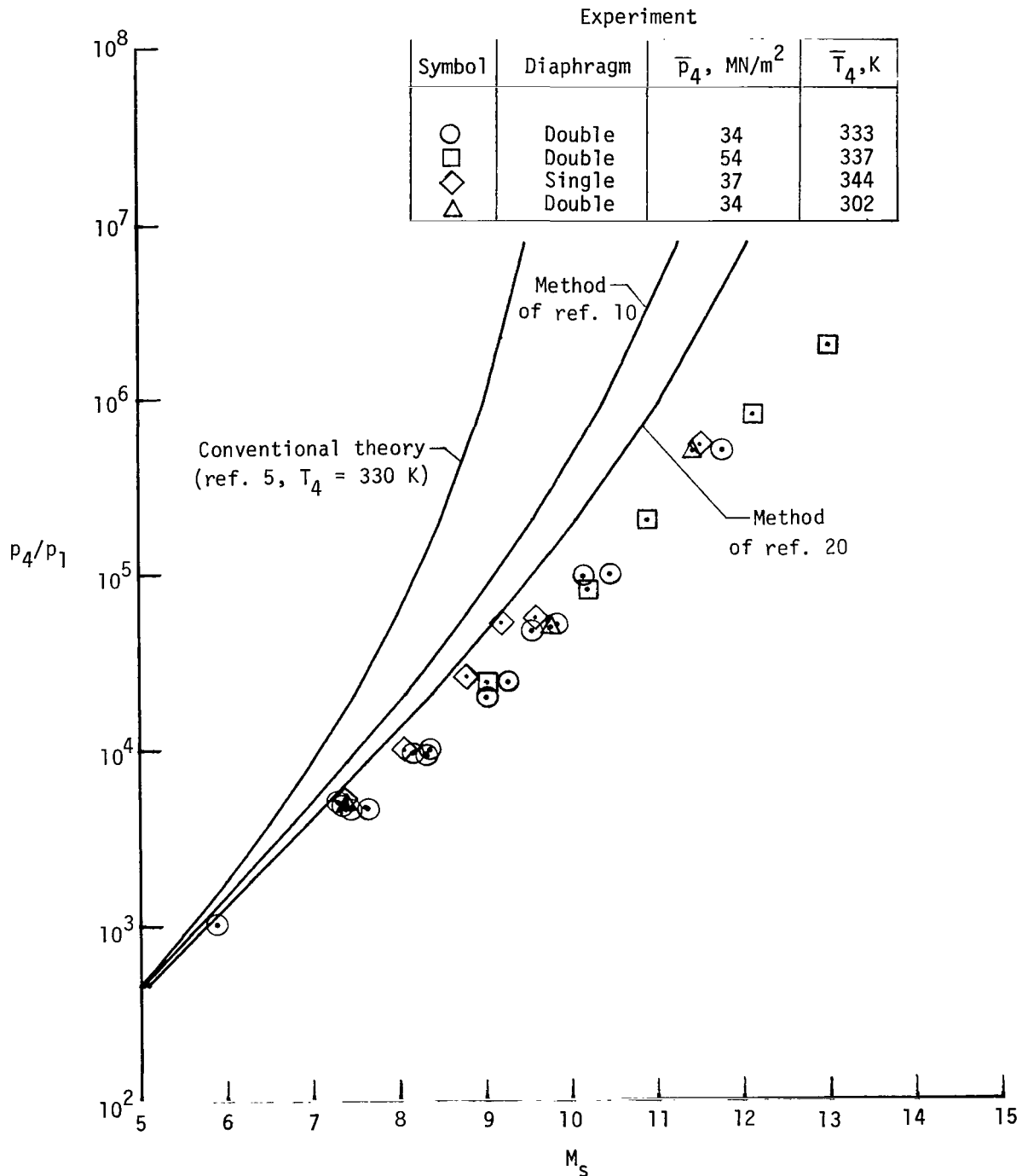
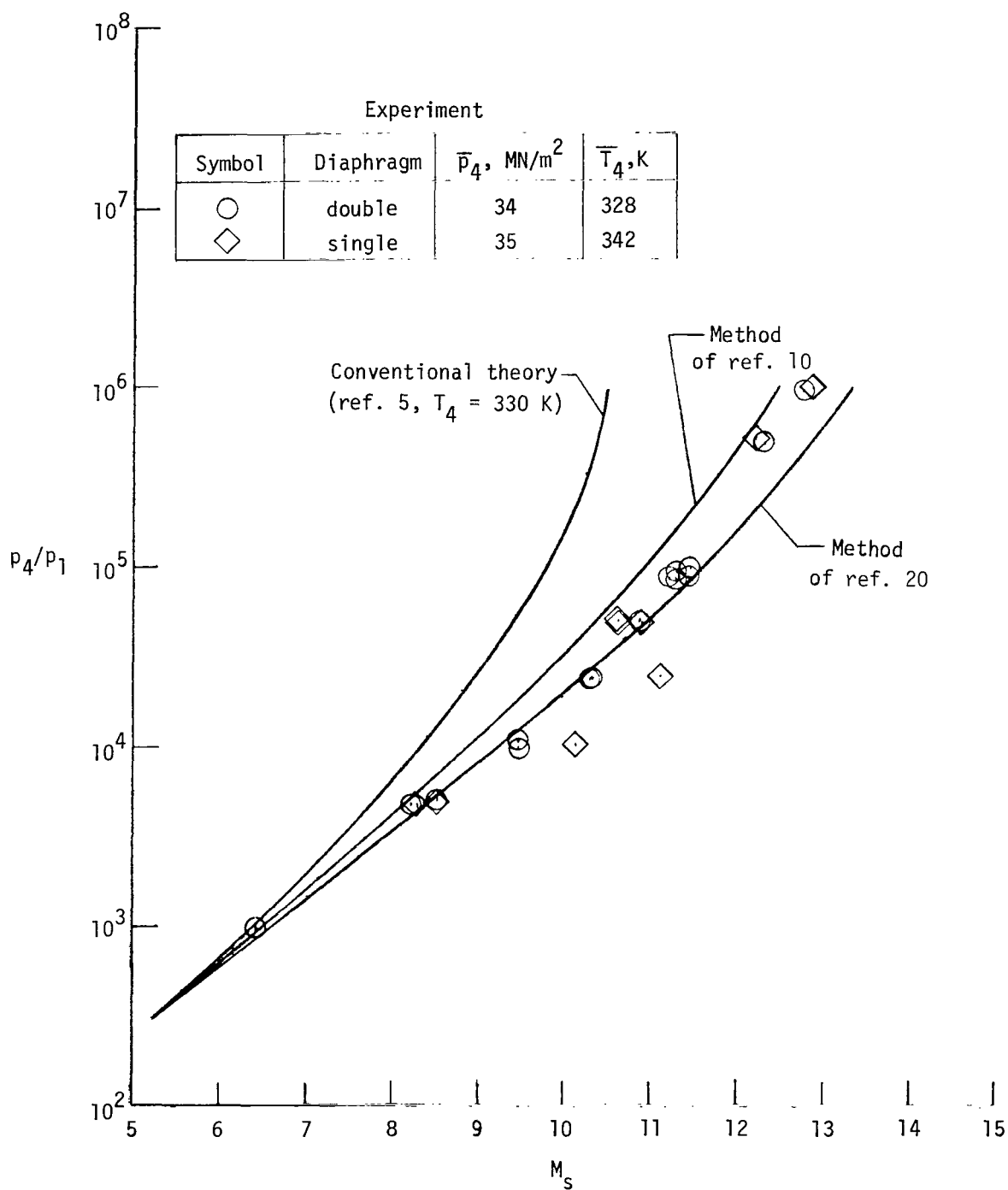


Figure 21.- Parameter Π as a function of shock Mach number for various driver-driven gas combinations. $T_4 = 300$ K; $\tilde{A} = 1.0$.



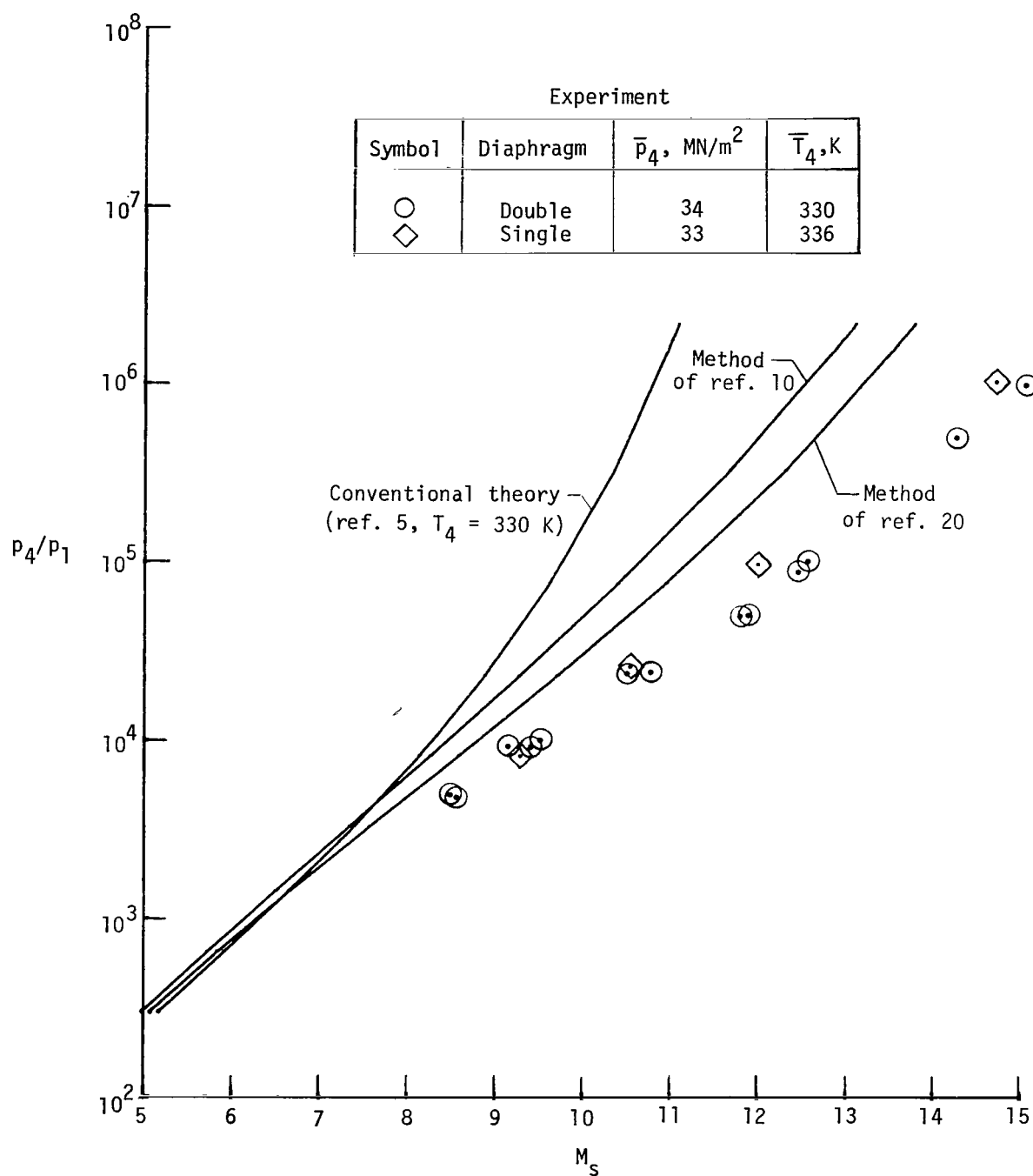
(a) Air.

Figure 22.- Shock Mach number in various test gases as a function of pressure ratio across primary diaphragm. Symbols denote maximum value of M_s .



(b) Argon.

Figure 22.- Continued.



(c) CO₂.

Figure 22. - Continued.

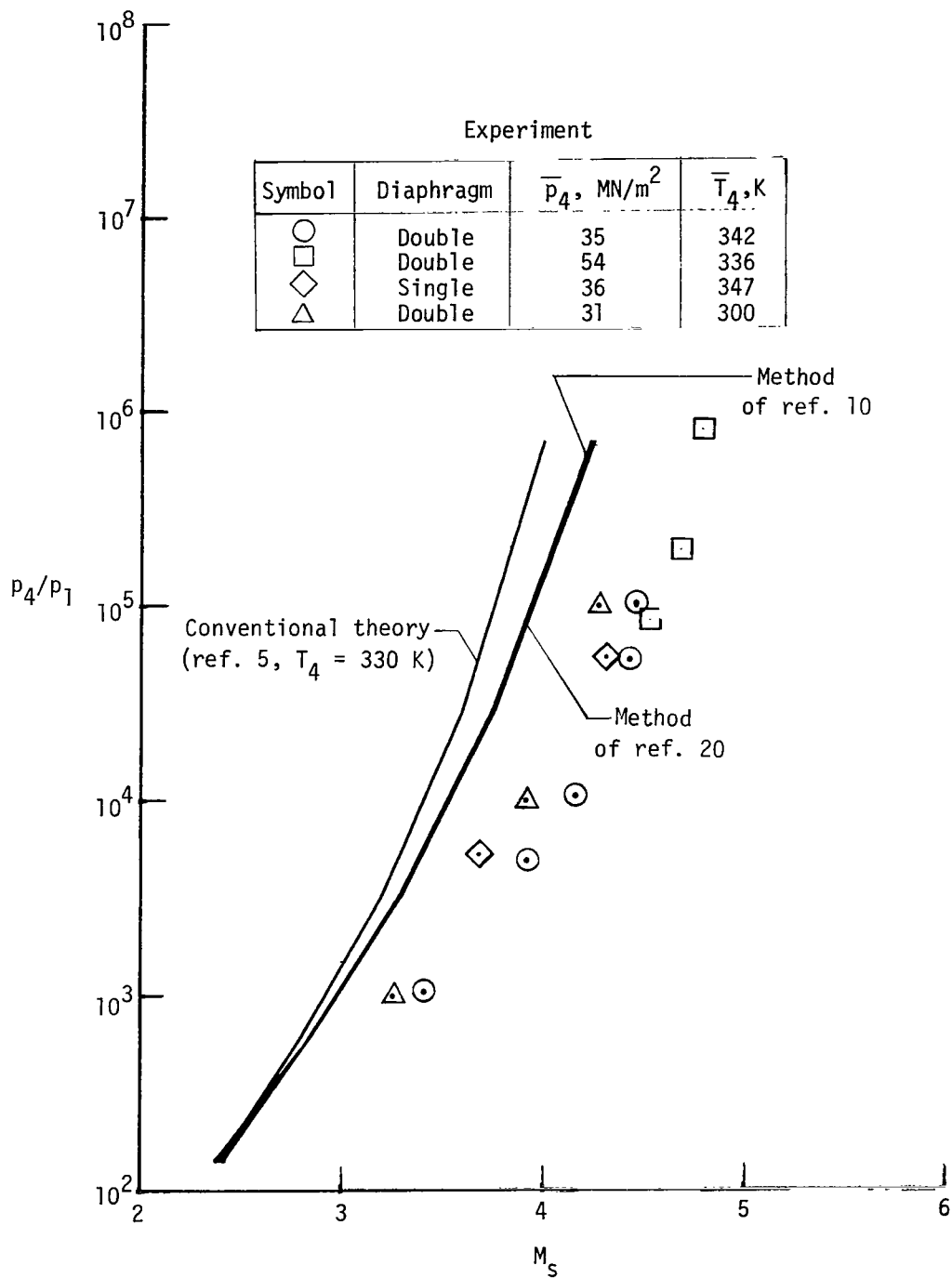


Figure 22. - Concluded.

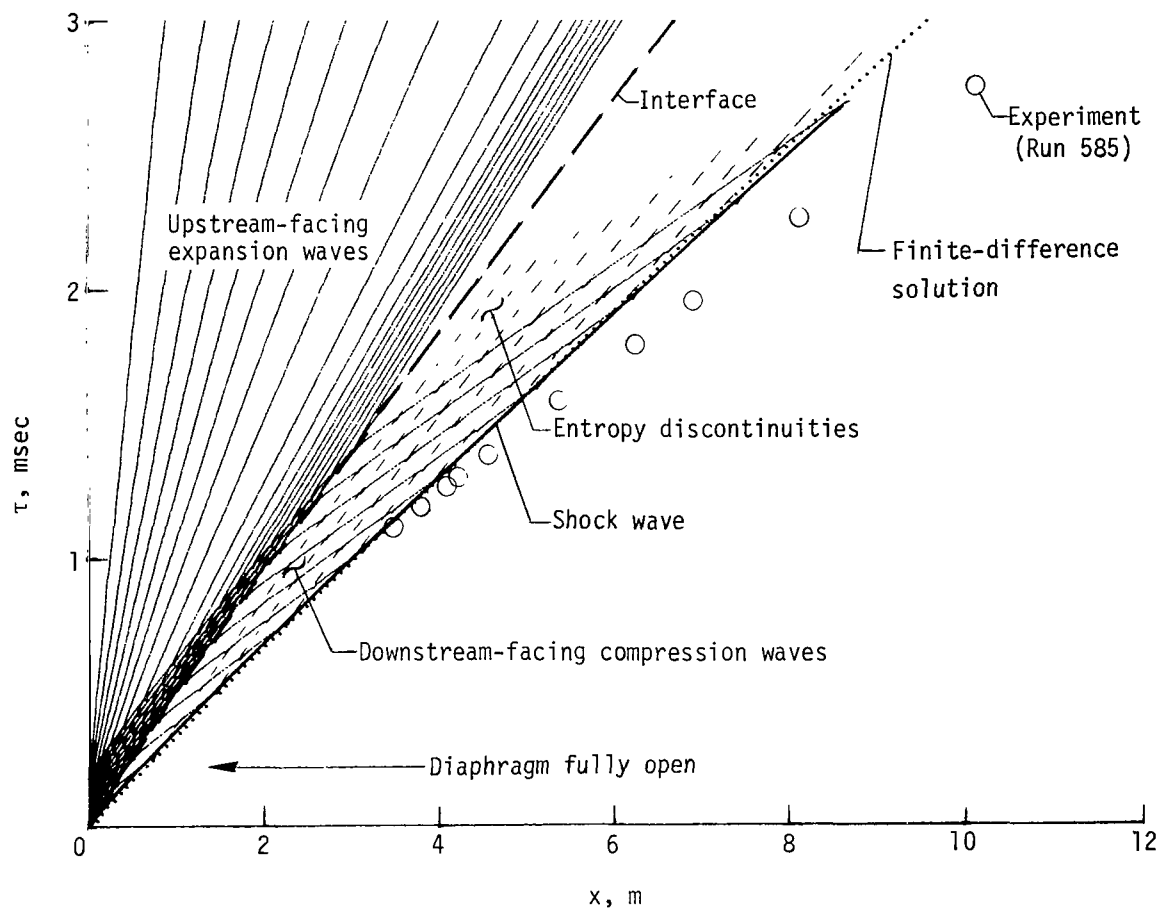


Figure 23.- Distance-time sketch of method-of-characteristics solution for helium driver and test gas. Diaphragm opening time of 200 μ sec.

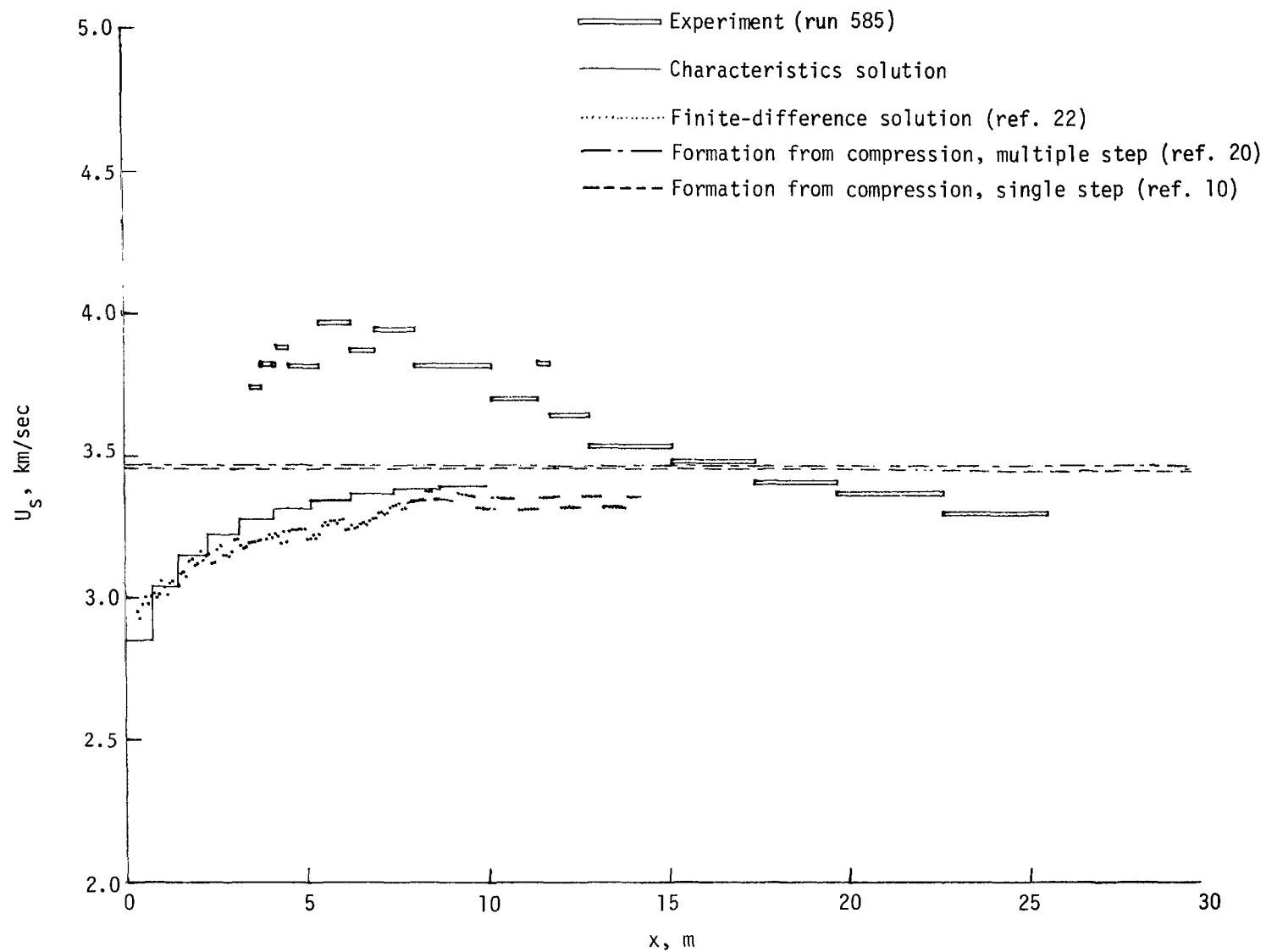


Figure 24.- Experimental and theoretical variation of shock velocity with distance downstream of diaphragm for helium as driver and test gas.

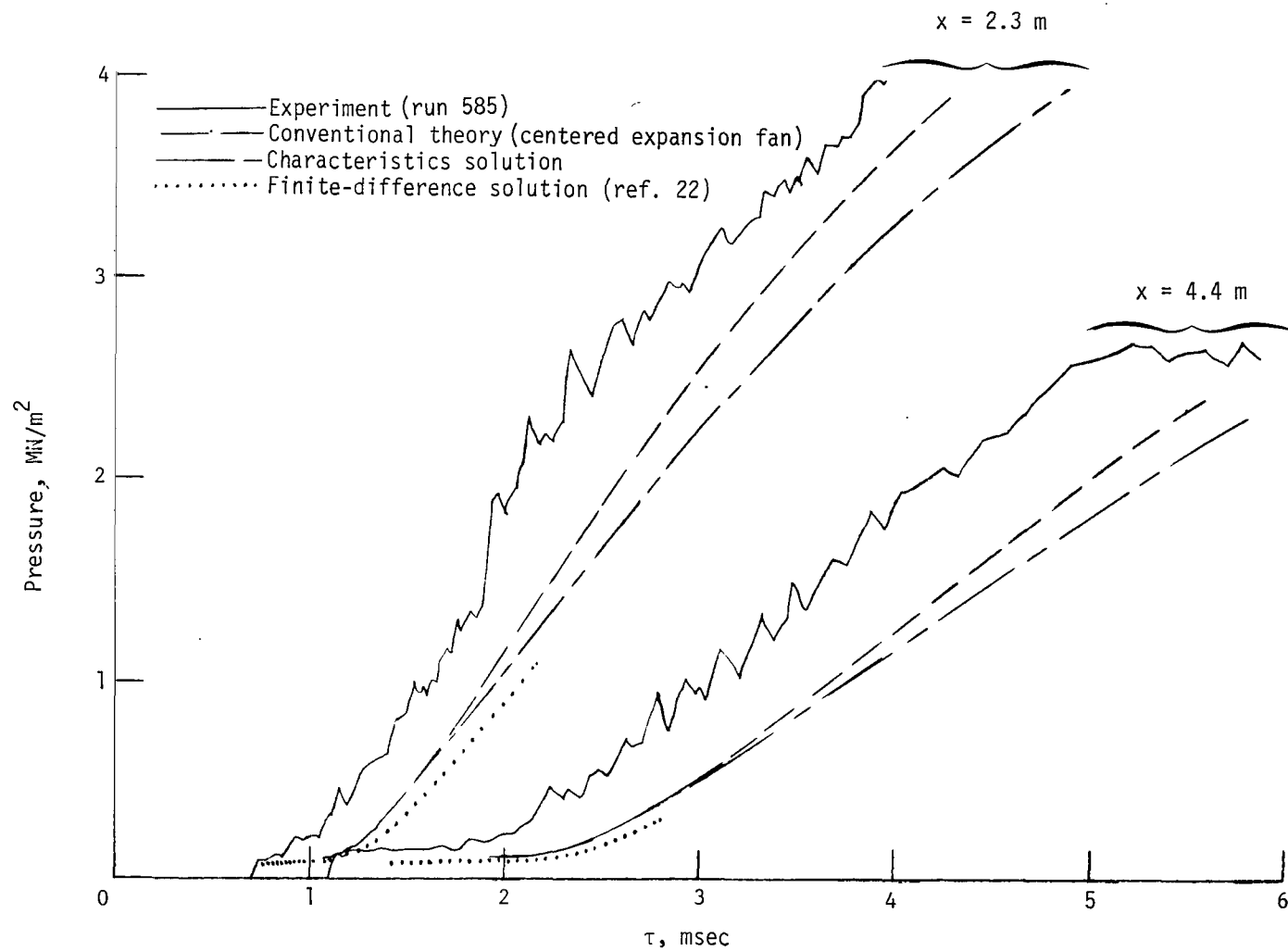


Figure 25.- Expanding driver pressure as a function of time at two distances downstream of diaphragm.

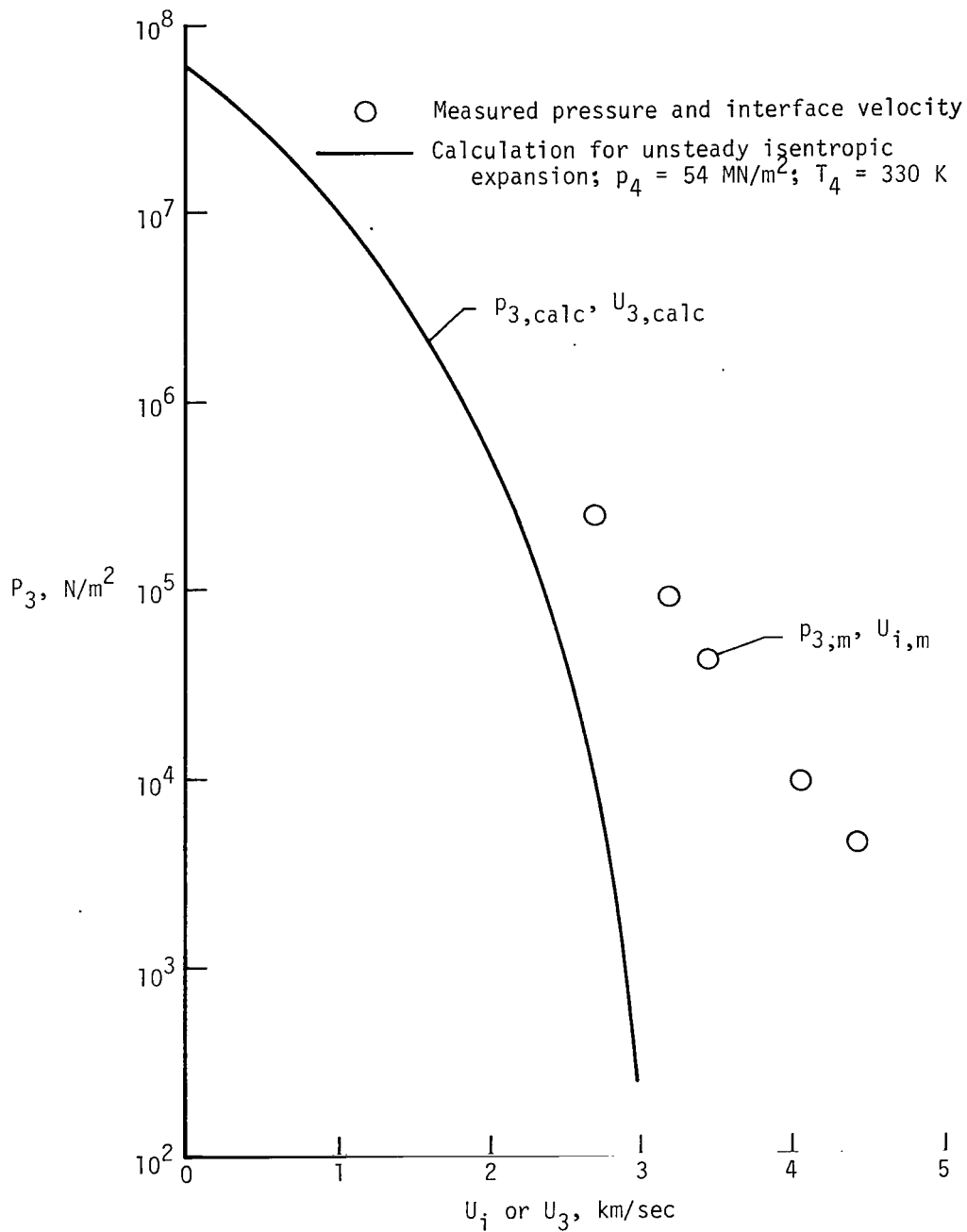


Figure 26.- Measured and calculated interface conditions for a series of tests with air as test gas.

NATIONAL AERONAUTICS AND SPACE ADMINISTRATION
WASHINGTON, D.C. 20546

OFFICIAL BUSINESS
PENALTY FOR PRIVATE USE \$300

SPECIAL FOURTH-CLASS RATE
BOOK

POSTAGE AND FEES PAID
NATIONAL AERONAUTICS AND
SPACE ADMINISTRATION
451



136 001 C1 U D 751212 SC0903DS
DEPT OF THE AIR FORCE
AF WEAPONS LABORATORY
ATTN: TECHNICAL LIBRARY (SUL)
KIRTLAND AFB NM 87117

POSTMASTER: If Undeliverable (Section 158
Postal Manual) Do Not Return

"The aeronautical and space activities of the United States shall be conducted so as to contribute . . . to the expansion of human knowledge of phenomena in the atmosphere and space. The Administration shall provide for the widest practicable and appropriate dissemination of information concerning its activities and the results thereof."

—NATIONAL AERONAUTICS AND SPACE ACT OF 1958

NASA SCIENTIFIC AND TECHNICAL PUBLICATIONS

TECHNICAL REPORTS: Scientific and technical information considered important, complete, and a lasting contribution to existing knowledge.

TECHNICAL NOTES: Information less broad in scope but nevertheless of importance as a contribution to existing knowledge.

TECHNICAL MEMORANDUMS: Information receiving limited distribution because of preliminary data, security classification, or other reasons. Also includes conference proceedings with either limited or unlimited distribution.

CONTRACTOR REPORTS: Scientific and technical information generated under a NASA contract or grant and considered an important contribution to existing knowledge.

TECHNICAL TRANSLATIONS: Information published in a foreign language considered to merit NASA distribution in English.

SPECIAL PUBLICATIONS: Information derived from or of value to NASA activities. Publications include final reports of major projects, monographs, data compilations, handbooks, sourcebooks, and special bibliographies.

TECHNOLOGY UTILIZATION PUBLICATIONS: Information on technology used by NASA that may be of particular interest in commercial and other non-aerospace applications. Publications include Tech Briefs, Technology Utilization Reports and Technology Surveys.

Details on the availability of these publications may be obtained from:

SCIENTIFIC AND TECHNICAL INFORMATION OFFICE

NATIONAL AERONAUTICS AND SPACE ADMINISTRATION

Washington, D.C. 20546